12-2020

Seismic Expressions of Paleokarst

Olanrewaju Ayodapo Aboaba
University of Arkansas, Fayetteville

Seismic Expressions of Paleokarst

A dissertation submitted in partial fulfillment
of the requirements for the degree of
Doctor of Philosophy in Geosciences

by

Olanrewaju Ayodapo Aboaba
Federal University of Technology, Akure
Bachelor of Technology in Applied Geophysics, 2004
University of Oklahoma
Master of Science in Geophysics, 2015

December 2020
University of Arkansas

This dissertation is approved for recommendation to the Graduate Council

_____
Christopher L. Liner, Ph.D.
Dissertation Director

_____
Walter L. Manger, Ph.D.
Committee Member

_____
Thomas Mac McGilvery, Ph.D.
Committee Member

_____
Matthew D. Covington, Ph.D.
Committee Member

_____
Doy L. Zachry, Ph.D.
Committee Member

ABSTRACT

Paleokarst are characterized by epigene and/or hypogene processes in their formation and hold significant numbers of hydrocarbons and other natural resources. This dissertation examines worldwide seismic expression of paleokarst; and specifically, the characterization of paleokarst reservoirs developed across the Cherokee Platform, and in the Arkoma Basin, Oklahoma.

Worldwide subsurface paleokarst formations are of Precambrian to Miocene age and found at depths less than 200 m to as great as 8000 m. Karst can be are expressed on seismic records as sinkholes, paleocave collapse, and tower morphologies. Seismic modeling indicates that karst can be modeled and imaged to better understand its subsurface architecture. High variance, negative curvature, bright amplitudes/localized bright spots characterize karst. As part of this dissertation, a worldwide map of paleokarst locations was generated, and geophysical measurements for some of these locations were taken for further analysis.

In the Arkoma Basin, the Ordovician Viola Limestone, Mississippian Caney Shale, Pennsylvanian Jefferson Sandstone and Wapanucka Limestone were mapped on seismic data, and paleokarst sinkhole and pipe features were identified. Viola sinkholes can be recognized as structural depressions, characterized by higher seismic variance, and lower positive amplitude, and most-negative curvature. Wapanucka sinkhole features are subtle, show lower variance and higher positive amplitude, and no structural relief. The Ordovician sinkholes are coincident with the Pennsylvanian Wapanucka Limestone which are 610 m apart, with some of these sinkhole features occurring over vertical pipe features. The Viola sinkholes and pipe features are inferred to be a mature epigene karst system. The Wapanucka sinkholes are interpreted as an immature karst system with epigene and hypogene elements. This study indicates for the first-time

evidence of pipe features that extend from the Ordovician into the Mississippian, and the presence of Wapanucka sinkhole features in the Arkoma Basin of Oklahoma.

In the Cherokee Platform, the term Chat designates residual chert which is either in place or transported, formed by an epigene process, and found above the Miss Lime. The tripolite is internal to the Mississippi Lime formed by in place alteration of the limestone by epigene and/or hypogene processes. I have classified and mapped Chat and tripolitic chert (tripolite) zones by seismic evaluation calibrated by well control with full-wave sonic log data. Chat and tripolite show clear separation on total acoustic impedance from Miss Lime, but no separation with V_P /V_S, and both exhibit total porosities greater than 20 % with an indication of fracture porosity. Sonic-based normal incidence wedge models for Chat bounded above by Pennsylvanian Shale and below by Miss Lime indicate two seismic expressions are probable: a strong negative amplitude when Chat thickness is above tuning and a weak or non-existent amplitude associated with small impedance contrast between Chat and overlying Pennsylvanian shale. This analysis suggests both the traditional Chat ‘strong response’ and a new ‘dim-out’ exploration approach. Tripolite response is consistently a negative amplitude event that strengthens with increasing tripolite thickness. This study provides an interpretive framework for characterizing Chat and tripolite zones associated with the Mississippian Lime in the US Midcontinent, which may be applicable to areas around the world.

ACKNOWLEDGEMENTS

I am immensely grateful to Dr. Christopher Liner my faculty advisor for his guidance, patience, and support all through my study in Arkansas. I have really learnt a lot from him, and I am confident working with him has prepared me for the challenges and opportunities that lies ahead. Dr. Covington who taught me how to use python software. Dr. Walt Manger for the field trips and exposure to geology. “The best geologist is one who has seen the most rocks”. Dr. Mac McGilvery and Dr. Doy Zachry who have expanded and deepened my geological mind from the perspective of my geophysical training.

This project benefited from data and expertise provided to the Department of Geosciences by Shane Matson, Charles Wickstrom, Ron Snyder, and Don Unruh.

I am truly grateful to Dr. Oluwaseyi Ogunsola and family, Oluwafemi Alademehin, Oluwatobi Olorunsola, Dr. Bode Omoboya, The Omolewus’, Solomon Ojo, Carly Bartow, Mr. Boyd Fisher, Karli Moore, Emily Burch, Rev. Jody Farrell and family for their immeasurable support and guidance. Ikrammuddin Bahram, Abram Barker for those long hours we spent in the office and going on hikes, and other friends and well wishers who have contributed to making this a reality.

Oyeronke Fatoki for your support and pushing me harder to complete this work and believing in me. You are truly appreciated and loved.

I truly appreciate my family my parents - Michael and Tanwa Aboaba, my siblings, Olakunle, Segilola and Morohounfoluwa for their prayers, support and encouragement without you all this would not have been possible.

DEDICATION

This dissertation is dedicated to the Almighty God who in His infinite wisdom and grace has made this possible; in you, I live and move and have my being.

TABLE OF CONTENTS

LIST OF FIGURES

LIST OF TABLES

LIST OF PUBLISHED PAPERS

Aboaba, O. A., and C. Liner, 2019, Interpretation of Paleozoic Paleokarst Features in the Arkoma Basin of Oklahoma using 3D Seismic and Well Logs: Interpretation, **8**, no. 2, T421-T440, doi:/10.1190/int-2019-0155.1. Published, Chapter 3

Aboaba, O. A., and C. Liner, 2020, Mississippian Chat and Tripolite Zones in Osage County, Oklahoma: Paleokarst Interpretation based on 3D Seismic and Well Logs: Interpretation. In Final Review, Chapter 4.

CHAPTER 1

Introduction

This doctoral dissertation is presented in five chapters. Chapter 1 presents the introduction. Chapters 2, 3 and 4 will culminate as papers for publication. Chapter 5 is the conclusion.

Chapter 2 treats paleokarst of world-wide regions reported on seismic and well logs, particularly in hydrocarbon reservoirs; the geological aspects of paleokarst reservoirs; seismic expressions of paleokarst based on scale, seismic resolution, and characteristic elements in seismic data to identify karst and numerical and physical models. I show seismic interpretation methods such as horizon tracking techniques and seismic attributes in mapping karst. I discuss rock physics, drilling and production challenges reported for karst reservoirs. I generate a map of worldwide karst locations and present a table of seismic measurements for some of these karst locations.

In Chapter 3, I investigate paleokarst features in the Arkoma Basin. Four horizons were mapped on seismic namely the Ordovician Viola Limestone, Mississippian Caney Shale, Mississippian Jefferson Sandstone and Pennsylvanian Wapanucka Limestone for paleokarst evidence. I present the use of seismic attributes of variance, amplitude, and curvature in characterizing sinkhole and pipe features. Seismic amplitude analysis and Gassmann equations models are applied to illustrate the effect of acoustic impedance on amplitude for the Viola and Wapanucka Limestone, respectively.

In Chapter 4, I examine paleokarst Chat and tripolite zones associated with the Mississippian Lime. The Chat is associated with meteoric water and found at the Mississippian Pennsylvanian Boundary. Tripolite is found below the Mississippian Limestone. I correlate Chat

and tripolite zones on well logs. I show wedge models for Chat and tripolite to determine how amplitude varies with thickness. Exploratory data analysis plots of V_P /V_S and total porosity; and acoustic impedance against total porosity of Chat and tripolite, respectively. We delineate Chat and tripolite using time structure, amplitude, acoustic impedance, and porosity maps. Acoustic impedance against total porosity; and V_P/V_S against porosity plots were generated that show distinct and variable characteristics of Chat and tripolite from Mississippian Limestone.

In Chapter 5, I make conclusions and the implication of these studies.

CHAPTER 2

Worldwide Seismic Expressions of Paleokarst: A Review

Olanrewaju Aboaba and Christopher Liner, Department of Geosciences, University of Arkansas

This paper will be submitted to the journal Interpretation

Abstract

Paleokarst reservoirs associated with carbonate rocks represent some of the largest oil and gas fields found worldwide. In addition, they hold a large amount of groundwater and industrial minerals. Paleokarst reservoirs from the Precambrian to the Miocene have produced hydrocarbons We have reviewed karst features identified particularly from seismic data and well logs. The advent of 3D seismic data in the 1980s provided the ability to characterize subsurface paleokarst terrains. Post-stack data conditioning techniques, such as structural smoothing and spectral bluing, have increased seismic data fidelity thereby improving interpretation of paleokarst features, such as sinkholes, tower karst, fluvial systems and channels associated with karst features. Other mapping techniques used to identify these features include auto-tracking, manual tracking of individual sinkholes when auto-tracking fails, isochron maps that show changes in sinkhole evolution, 90^{o} phase conversion of seismic data that aids in the interpretation of weak and difficult events caused by paleocave collapse. Poststack seismic attributes such as variance, chaos, curvature, amplitude, acoustic impedance, and multi-trace attributes are useful in delineating subtle karst features, which may not be visible on time maps. The interior of paleokarst features are characterized by high variance, negative curvature, high amplitudes (localized bright spots), and low impedance. Drilling through karst reservoirs exhibits high production rates, loss circulation, and anomalous readings on well logs. For the first time, a worldwide map of subsurface paleokarst locations observed from seismic and well logs and

geophysical measurements of paleokarst locations has been provided. This review will be useful in understanding paleokarst occurrence around the world.

Introduction

Carbonates account for about 50 percent of the hydrocarbon production in the world (Ford and Williams, 2007). Other valuable minerals, such as uranium, aluminium, nickel, vanadium, uranium and phosphates, as well as groundwater, are found in karstified carbonate rocks (Mazzullo and Chilingarian, 1996).

Paleokarst is karst terrain that has undergone tectonic subsidence to lie below an unconformity (Ford and Williams 2007) or other stratigraphic discontinuities (Fritz,1991). These discontinuities are unconformities related to major karst events; sequence boundaries linked to regional karst; and conformable boundaries associated with minor karstification (Fritz, 1991).

Esteban and Klappa (1983) defined karst as "diagenetic facies, an overprint in subaerially exposed carbonate bodies, produced and controlled by dissolution and migration of calcium carbonate in meteoric waters, occurring in a wide variety of climatic and tectonic settings and generating a recognizable landscape." Ford and Williams (2007) defined karst as "comprising terrain with distinctive hydrology and landforms that arise from a combination of high rock solubility and well-developed secondary (fracture porosity)".

James and Choquette (1988) noted that the development of karst landforms occurs by external and inherent factors. The external factors include climate (precipitation and evaporation, temperature), base level (relief and elevation, sea level or local water tables), plant life and duration of time and inherent factors, such as structure and stratigraphy (strata attitude, unconfined or confined aquifers and structural conduits) and lithology (fabric and texture, bedding thickness, fractures, and stratal permeability). Karst landforms are characterized by

sinking streams, caves, enclosed depressions, fluted rock outcrops and large springs (Ford and Williams, 2007). These karst landforms are synonymous with epigene karst, comprising about 90% of karst landforms. Esteban and Kappa (1983) further classified these landforms into lapies (channels or furrows), dolinas (sinkholes) and poljes (interior valleys) for surface features; pores caves, vugs and pipes for subterranean landforms; as well as speleothems and collapse structures. Dense, massive, pure, and coarsely fractured rocks are most likely to produce karst. High porosity carbonates (30-50%) are less likely to develop karst, while rocks with negligible primary porosities support excellent karst (Ford and Williams 2007).

Fritz (1991) noted that karst is a diagenetic process that involves agitated flow through a vug diameter of 5 mm or more by hydronormal (meteoric) or hydrothermal waters (connate) and laminar flow through pores of less than 5 mm. The length of exposure determines the evolution of karst terrain from youthful, mature to senile. In the youth stage, the flow regime is mainly by conduit. In the mature and senile stages, channel flow dominates. The position of the water table with respect to the vadose (aerated) and phreatic (saturated) zones is important in describing karst structure.

Ford and Williams (2007) illustrated a comprehensive karst system (Figure 2.1). They divided karst into net erosion and net deposition. The net erosion is characterized by dissolution along ground water flow regimes, which is the diagnostic characteristic of karst. A large percentage of a karst network is of meteoric origin (epigene) occurring at shallow depth. The remaining percentage consists of deep circulating, heated waters, or basement waters or sedimentary basin subsidence (hypogene).

Hypogene karst is synonymous with deep-seated fluid activity (Palmer, 1991; Loucks, 1999; Klimchouk, 2007), or regeneration of epigene processes by deep-seated mechanisms

(Palmer, 1991), with waters at elevated temperature and pressure relative to ambient conditions (Wright and Harris, 2013), and linked with rising thermal fluids (Klimchouk, 2007). The dissolution fluids include sulfuric acid, breached from hydrocarbon oilfields (Hill, 1990, 1995) or igneous basement hydrothermal fluids migrated along faults causing dissolution (Palmer, 1991; Burberry et al., 2015, 2016). Wright and Harris (2013) and Wright (2016) proposed deep-seated processes (hypogene/hydrothermal) to be associated with development of saddle dolomite, compacted grains, fractures linked with stylolites, late cements and cements with hydrocarbon inclusions, and generation of minerals, such as dickite and Mississippi Valley Type deposits.

Fritz (1991) classified paleokarst reservoirs into syngenetic, mountain/plateau and hydrothermal. Mazzullo and Chilingarian (1996) proposed classification of karst reservoirs as buried hill traps, structurally expressed, linear fracture/fault trends, and non-structural and paleotopography expressed. Trice (2005) suggested buried hill, plateau, and buildup megakarst.

There have been numerous studies describing paleokarst reservoirs, however, integrated studies on a seismic scale have been limited to the Ellenburger in Texas and the Tarim Basin of China.

In this chapter, information from studies in US, Canada, Asia, and the Middle East are gathered for methods of identifying karst from 3D reflection seismic data and pitfalls that need to be understood. Karst is a very wide topic and we have incorporated a wide array of publications to determine how to identify and characterize paleokarst in the subsurface. In this overview we will analyze 1) production from karst, 2) shallowest and deepest reported paleokarst hydrocarbon fields, 3) geologically oldest and youngest fields, 4) comparison of scales for modern karst and paleokarst, 5) key seismic features that identify paleokarst, 6) seismic horizon techniques useful

in tracking paleokarst, 7) seismic attributes useful in paleokarst mapping, 8) rock and fluid properties that dominate paleokarst reservoir response and 9) drilling and production problems reported for paleokarst reservoirs from published and publicly available data. It is our goal that the reader will be better informed to identify and understand karst as a potential reservoir.

Geological Aspects

Hydrocarbon Fields with Primary Production from Paleokarst

Figure 2.1 shows worldwide locations of karst hydrocarbon reservoirs. Locations 1-40 are modified after Mazzullo and Chilingarian (1996) while locations 41-72 have been added by our deep literature search on paleokarst hydrocarbon reservoirs whose development involved 3D seismic methods.

Mazzullo and Chilingarian (1996) published a list of hydrocarbon reservoirs in karsted carbonate rocks (Table 2.1) from fields in North America (US, Canada, Mexico), Europe (Italy, Spain, Austria, Hungary, France), South America, Middle East (Saudi Arabia, UAE, Qatar, Iraq, Persian Gulf), Africa (Libya), and Asia (India, China, USSR, Iraq). Paleokarst reservoirs hold vast quantities of oil and gas. Mazzullo and Chilingarian (1996) citing Holtz and Kerans (1992) noted a total of 149 fields producing from the Ellenburger Formation in the Permian Basin, USA. They document producible remaining reserves, at 40% recovery, of 5.88×10^8 m^3 (3.7 Billion barrels of oil), with 2.23×10^8 m^3 of oil (1.4 billion barrels) produced as of 1992 including the Yates Field with a cumulative production of 1.7×10^8 m^3 (1.07 billion barrels) of oil from over 6.36×10^8 m^3 (4 billion barrels) original oil in place (Tinker et al., 1995). The Golden Lane Trend of Mexico has reserves of 2.9×10^{10} m^3 of oil (182.5 billion barrels) with 2.26×10^8 m^3 (1.42 billion barrels) produced. The Cerro Azul #4 well in the Golden Lane Trend was drilled to a depth of 500 m (1,640 ft) and flowed 4.13×10^4 m^3 (260,000 barrels/day) of oil; likely the

largest daily flow from a single well recorded in the world (Viniegra O. and Castillo-Tejero, 1970).

Paleokarst hydrocarbon fields not reported by Mazzullo and Chilingarian (1996) are given in Table 2.2. These include the Liuhua oil field located in the Pearl River Mouth basin of the South China Sea, the largest offshore oil producing field in China with reserves of 1.91 x 10^8 m^3 (1.2 billion barrels) (Tyrrell and Christian, 1992); the Nang Nuan oil field in the Chumphon Basin, Gulf of Thailand (Heward et al., 2000); the Luconia Field is the largest gas field in Malaysia with reserves of about 17-19 x 10^{10} m^3 (6-7 trillion ft^3) of gas (Alessio et al., 2005; Kosters et al., 2008). The Kashagan Field in the Caspian Sea of Kazakhstan holds about 5.6 x 10^6 m^3 (35 billion barrels) of oil with an estimated 1.59 – 2.07 x 10^9 m^3 (10-13 billion barrels) recoverable and about 1.4 x 10^{10} m^3 (52 trillion ft^3) of associated gas, probably the fifth largest field with respect to reserves in the world and maybe the largest oil field outside the Middle East (Sorkhabi, 2013). The Upper Devonian Grosmont Formation holds over 64.5 x 10^9 m^3 (406 billion barrels) of bitumen (Alberta Energy Regulator, 2015), but no commercial production (Russel-Houston and Gray, 2014), is the largest carbonate heavy oil reservoir in the world (Machel et al., 2014). The paleokarst Gohta and Alta fields of the Norwegian Arctic were discovered in 2013 and 2014 respectively (Matapour et al., 2018).

Shallowest/Deepest Karst Field

Hydrocarbon has been produced at a shallow depth of 261 m (856 ft) from the Ellenburger formation in West Era Field Cooke County Texas (Loucks, 2003). The deepest well was drilled into the Upper Cambrian Qiulitage dolomite in the Tarim Basin at a depth of 8048 m (26,404 ft) (Zhu et al. 2015).

Geologically Oldest/Youngest Paleokarst Field

The geologically oldest karst fields are found in the Precambrian (Neoproterozoic / Upper Proterozoic or Sinian age dolomites) in China, including the Dengying Dolomite Formation in the Weiyuan gas field, in the south western Sichuan Basin, with gas reserves in place of over a trillion cubic feet (Wei et al. 2008); the Wumishan Dolomite in the Renqui field in the Jizhong depression, west of the Bohai Bay Basin, which was China's first discovery with a high oil production (Qi and Xie-Pei, 1984). Outcrop analogs for the Wumishan Dolomite are found in Xi-Bai Shan 90 km (55 mi) north of Renqiu oil Field and Jin-Xian 300 km (186 mi) north east of Renqiu Field (Qi and Xie-Pei, 1984).

The youngest paleokarst hydrocarbon field is found in the Middle Miocene Jintan Limestone in Luconia province, offshore Sarawak State, Malaysia (Vahrenkamp et al., 2004).

Seismic Expression

Scale Comparison of Paleokarst Features and Seismic Resolution

There are a number of challenges faced in the proper imaging of karst reservoirs including: 1) interpretation of low frequency and low-quality seismic data in a complex carbonate environment (Zeng et al., 2010), 2) characterization of the geometry of collapsed paleocave complexes associated with faults and deformation (Zeng et al., 2011a), 3) discrimination between paleokarst features and noise both laterally and vertically in interpreting karst features (Chung et al., 2011), and 4) the fact that an irregular high-velocity unconformity surface of paleokarst can act as an imaging barrier to associated hydrocarbon reservoirs (e.g., the Vorwata field of Indonesia (Loh et al., 2016)). The limit of visibility is a fraction of the vertical resolution limit and depends on acoustic impedance contrast, noise level in the data and phase of the wavelet (Brown 2011).

Hardage et al. (1996) recorded frequencies of 10-150 Hz in the Boonesville Field of the Fort Worth Basin in Texas, imaging sinkhole diameters greater than 150 m in the Ordovician Ellenburger Formation. These measurements correlate to outcrop dimensions observed in the Ellenburger exposures in the Franklin Mountains, El Paso, Texas. Other reported scales of paleokarst feature include Vahrenkamp et al. (2004), Zeng et al. (2011a, 2011b), Russel-Houston and Gray (2014), Hunt et al. (2010), Sayago et al. (2012), Ahlborn et al. (2014), Aboaba and Liner (2018, 2020), and Basso et al. (2018) (Table 2.3). Furthermore, Table 2.3 shows the paleokarst measurements of sinkhole, pipes and towers observed worldwide from seismic data. Corral and Gonzalez (2019) indicate that surface sinkholes distributions show a truncated log lognormal fit (Figure 2.3).

Key Features in Seismic Data Identifying Paleokarst

Fontaine et al. (1987) suggested that the detection of paleokarst zones using seismic involve recognition of paleotopographic highs and other indicators of subaerial exposure, such as sediments onlapping on structural highs and irregularities disrupting seismic reflection events. Structural lows or highs delineated from paleotopography maps may show paleokarst systems (Loucks, 1999), with the structural lows diagnostic of sinkholes (Figures 2.5 and 2.7), while the highs may be indicative of tower karst, cone karst or residual hills (Figure 2.5). Hunt et al. (2010) noted that paleoslope, bedrock and faulting affect karst distribution and geometry.

Seismic mapping of an unconformity surface can reveal sinkholes, tower karst, hills, and fluvio-karst features, such as channels, canyons, and valleys (Zeng et al., 2011a, 2011b), (Figure 2.4). Paleokarst features can display discontinuous reflectors (Castillo and Mann, 2006), missing reflectors (Loucks 1999, 2003; Zeng et al. 2011a) and lateral discontinuities (Russel-Houston and Gray, 2014), (Figure 2.5).

Brown (1985) was the first to show sinkhole features on 3D seismic horizontal sections. Sinkholes appear as circular to elliptical features (Story et al., 2000; Ahlborn et al., 2014; Russel-Houston and Gray, 2014), or have elongated geometry (Loucks, 1999, 2003) on seismic time-slice images.

Paleokarst solution valley fills imaged on seismic data can exhibit a sinuous geometry (Russel-Houston and Gray, 2014), which may be associated with faults or erosional truncations or unconformities. Erosional (subaerial) unconformities on vertical seismic sections commonly define irregular paleotopography. Paleocave networks can be identified on seismic by localized isopach thicknesses in shallower formations (Loucks, 1999), structural depressions (Loucks, 1999; Zeng et al., 2011b), and circular or linear faults (Loucks, 2003; Zeng et al. 2011a, 2011b) (Figure 2.5). Anomalous amplitudes and bright spots have been associated with paleocave collapse (Zeng et al., 2011a, 2011b; Zhao et al., 2014, Basso et al. 2018) (Figure 2.6). These bright amplitudes are indicative of low impedance cave collapse zones in otherwise hard carbonate (Hunt et al., 2010). Chaotic reflections with minor fault indicators can divide bright spots as observed in the Ordovician Limestone, Tarim Basin (Zeng et al., 2010). Breccia pipes indicating collapse or dissolution chimneys can be seen on seismic data as disruption zones tapering upwards in vertical section and a cylindrical to conical geometry in horizontal view (Loucks, 2003; McDonnell et al., 2007; Cartwright et al., 2007; Zeng et al., 2011b; Sun et al., 2013; Aboaba and Liner, 2018, 2019, 2020). Paleokarst reflection events often show extreme disruption of stratal reflections and localized sag features (Loucks, 1999, 2003; Cartwright et al., 2007; Sun et al., 2013; Aboaba and Liner, 2018, 2019, 2020; Basso et al., 2018) (Figures 2.5 and 2.6).

Sinkholes are characterized by laterally discontinuous amplitude anomalies (Ahlborn et al., 2014; Russel-Houston and Gray, 2014; Kumbalek, 2015; Aboaba and Liner 2018, 2019, 2020) and differential amplitude outside of the sinkholes. High sinkhole amplitude with adjacent low amplitude have been documented in the Pennsylvanian Wapanucka Limestone, in the Arkoma Basin, Oklahoma, while the opposite effect has been observed in the deep Viola Limestone in the same 3D seismic survey (Aboaba and Liner, 2018, 2019, 2020). Paleokarst can be associated with stratiform breccia (associated with evaporite dissolution) and solution enhanced porosity can be laterally continuous with a stratiform low density zone and acoustic impedance contrast (Russel-Houston and Gray, 2014).

Hunt et al. (2010) noted that paleokarst features are arranged in separate subparallel zones that follow truncated strata. Each zone showed a specific relief, sinkhole density and depth variations attributed to seismic velocity changes. Purdy and Betram (1993) reported that the time sag effect of paleokarst collapse features on deeper seismic reflections poses a challenge to determine the level at which collapse begins. Linear rather than circular low velocity time sag suggests carbonate collapse, with vertical dim-amplitude zones related to subsidence and possibly gas chimneys (Story et al., 2000). Collapse features may show a notable time sag below a sinkhole, which is caused by the variable low-velocity sinkhole fill composed of overlying sandstone, mudstone, coal, and carbonate blocks (Russel-Houston and Gray, 2014).

The Role of Seismic Modeling

Purdy and Waltham (1999) combined ray tracing with wave equation-based diffractions to show that the scale of tower and cone karst observed on modern analogs is sufficient to be seen on synthetic seismic sections. Yao et al. (2005) used seismic forward models to show that diffractions from fluid filled caverns are strong in contrast to the weak reflections of the

carbonate host rock, and that the diffraction amplitude is more influenced by cavern width than height. Barber and Marfurt (2009) used 2D wave field modelling to demonstrate that valley shaped anomalies can be caused by dissolution and collapse rather than a velocity anomaly. Zeng et al. (2011a, 2011b) using wave equation models showed that impedance contrast and cave dimensions are important factors that influence the amplitude anomaly features associated with paleocaves. Yang et al. (2012) categorized fractured cave bodies as three models with increasing dissolution and collapse termed 'honeycomb, hamburger, and pineapple' in the Tarim Basin using numerical and physical models, observing a gradual link in reservoir evolution and erosion for these models. They noted that total cave volume, total porosity, and inner structure influence reflection amplitudes, and higher amplitudes suggest a cave cluster.

Zhan et al. (2014) used elastic finite-difference modelling to demonstrate the horizontal limit of visibility for paleokarst was a width of 30 m or a 500 m karst dipping at 60^{o}. They noted that the true width of the karst image was correct when the width of the karst was greater than the P-wavelength (Figure 2.8). Verma et al. (2015) used wave equation modelling in the Mississippi Lime of Oklahoma to show that reflection sag features were due to paleokarst topography and not velocity pull down due to gas chimneys (Figure 2.9). Xu et al. (2016) using physical models to study paleokarst caves pointed out that relative amplitudes of anomalous bright spots increased with cave width and decreased with cave velocity, reporting that when cave heights exceeded 100 m two distinct anomalous bright spot reflections were created. Basso et al. (2018) using physical experiments showed that most 'string-of-beads' bright spots observed in the Macae Group carbonates of the Campos Basin, Brazil have cave diameters of between 60 and 80 m.

Seismic Interpretation Methods

Seismic Horizon Tracking Techniques for Paleokarst

Successful tracking/auto tracking of horizons to map and identify subtle paleokarst features requires that the seismic dataset be subjected to post-stack filtering processes to suppress noise and increase the fidelity of the seismic data. These techniques include structural filtering (Sullivan et al., 2006; Russel-Houston and Gray, 2014; Qi et al., 2014), spectral balancing, and bluing (Qi et al., 2014).

Loucks (1999, 2003) used tracking to identify collapsed paleocave system trends from a time structure residual (second order derivative) map in the Ellenburger group in West Texas (Figure 2.5). Zeng et al. (2006) generated a horizon residual map by removing the regional structural trend from the structure map. This procedure allowed the recognition of subtle circular collapse trends in the Hobbs Field, New Mexico, USA.

In Barents Seas paleokarst, Hunt et al. (2003) auto tracked a seismic zero crossing to increase vertical resolution to a few meters. In regions that are difficult to track, because of discontinuities, manual tracking of sinkholes should be undertaken. Manual tracking of individual sinkholes has been utilized because of failure of edge detection and geobody extraction to differentiate karst from noise (Russel-Houston and Gray, 2014).

In China's Tarim Basin, Zeng et al. (2011a, 2011b) rotated 3D seismic data to a 90^{o} phase to aid interpretation of weak, discontinuous events caused by paleocave collapse. In addition to attribute volumes and visualization as a guide, paleokarst interpretation quality is dependent on the judgement of the interpreter to achieve a geologically reasonable result.

Horizon flattening on the top basement reflector in the Barents Sea visualized paleokarst features that were previously unidentified (Hunt et al., 2010) and allowed mapping of top and

base of paloekarst zones for well planning (Hunt et al., 2010). Isochron maps can indicate changes in sinkhole evolution (Sullivan et al., 2006; Basso et al., 2018; Aboaba and Liner, 2020) and graphs of sinkhole depths as a function of distance along the geomorphic profile show a relationship between karst penetration and paleoslope (Hunt et al., 2010).

Seismic Attributes Useful for Mapping Paleokarst

Seismic attributes measure 3D seismic time, amplitude, frequency and/or attenuation characteristics (Sherriff, 2002). These serve as tools for defining geology and quantifying zone properties of seismic data (Barnes, 2016).

Poststack attributes used to delineate paleokarst features include:

Curvature

Curvature measures the change of dip and azimuth on a 3D seismic reflection surface (Roberts, 2001; Barnes, 2016) and are organized into classes, for example: positive, negative, most positive, most negative, etc. Lineaments in the most negative curvature indicate valleys, while lineaments in the most positive curvature indicate ridges (Sullivan et al., 2006). Positive values on most-positive curvature indicate domes. Negative values on most positive curvature are associated with bowls (Al-Dossary and Marfurt, 2006; Sullivan et al., 2006). In paleokarst settings, these bowls can indicate sinkholes or collapse features related to a system of faults and joints (Sullivan et al., 2006; Qi et al., 2014). Gaussian curvature may also be an indicator of paleokarst infill (Al-Dossary and Marfurt, 2006). Horizon slices of most positive curvature can highlight subtle polygonal or cockpit paleokarst (Nissen et al., 2009, Moser, 2016) (Figure 2.10). Horizon slices of most positive and negative curvature showed the presence of sinkholes in Southern Oklahoma (Kumbalek, 2015; Aboaba and Liner, 2018, 2020) and the Fort Worth Basin of Texas (Qi et al., (2014).

Coherence

Coherence measures similarity of waveforms around a central point (Bahorich and Farmer, 1995; Chopra and Marfurt, 2007; Barnes, 2016). Other computed forms of coherence include: semblance "ratio *of the energy of the average trace to the average energy of all the traces along a specified dip*" (Chopra and Marfurt, 2007), and variance is derived by subtracting the semblance from one (Chopra and Marfurt, 2007). Coherence highlighted faults and fractures associated with paleokarst (Story et al., 2000; Heubeck et al., 2004; Qi et al., 2014; Kumbalek, 2015; Spina et al., 2015) and sinkholes (Story et al., 2000; Heubeck et al., 2004; Qi et al., 2014; Kumbalek, 2015; Basso et al., 2018; Aboaba and Liner, 2018, 2019, 2020) (Figure 2.7c). Continuity time slices have been used to highlight circular faults linked to paleocave collapse and linear faults associated with paleocave passages (Zeng et al., 2011a, 2011b). Vahrenkamp et al. (2004) and Chung et al. (2011) used horizon slice semblance-based coherence to delineate dendritic drainage patterns comparing paleokarst and patch reefs in the Miocene Jintan limestone, Offshore Sarawak State, Malaysia. Dendritic paleokarst patterns showed a downward propagating chaotic expression in contrast to patch reefs that showed discontinuities only for a short time interval (Chung et al., 2011). Variance has been used to highlight subtle sinkhole features not visible on horizon time structure maps in the Wapanucka Limestone of Southern Oklahoma (Aboaba and Liner, 2020).

Acoustic Impedance Inversion

Acoustic impedance (AI) is defined as the product of mass density and seismic velocity. Acoustic impedance inversion is the process of estimating AI from 3D poststack seismic data using one or more wells for calibration (sonic and density logs required). In the case of paleokarst, low-porosity, unkarsted limestone host rock has relatively high impedance, while

high-porosity reservoirs have relatively low impedance. Vahrenkamp et al. (2004) showed estimated acoustic impedance values for reservoir zones with a karst overprint. Duo et al. (2011) used acoustic impedance to distinguish paleokarst from non-paleokarst reservoirs in the San Andreas Formation in the Permian Basin, Texas. Fernandez and Marfurt (2013) suggested that high acoustic impedance correlated with the dense Ordovician Ellenburger Formation in the Fort Worth Basin, Texas, while low impedance values may relate to Barnett shale infill of paleokarst collapse features. In the Devonian Grosmont formation of Western Canada, Russel-Houston and Gray (2014) showed an impedance contrast of 6,000 kPa.s/m between the non-reservoir and paleokarst reservoir rock. Spina et al. (2015) observed that wells drilled into low impedance paleokarst zones show high secondary porosity zones in the Devonian Kharyaga Platform in Russia. Li et al. (2016) used acoustic impedance to define a very low impedance cavern carbonate reservoir in the Tarim Basin, China. Moser (2016) showed that sinkholes in the Boone Limestone showed low acoustic impedance within the sinkholes and higher acoustic impedance outside the sinkholes (Figure 2.11). Kilcoyne (2018) used three different AI inversion methods to characterize the Austin Chalk, reporting that model-based inversion had the highest correlation of 96%, while band-limited and colored inversion had accuracy of 82% and 75%, respectively (Figure 2.12)

Spectral Decomposition

Spectral decomposition (SD) (Chakraborty and Okaya, 1995; Barnes 2016) decomposes a seismic trace time signal into a time-frequency representation revealing the time-dependent frequency nature of the seismic signal. Many methods of time-frequency decomposition have been developed. Using 8-10 Hz spectral decomposition (SD), Hunt et al. (2010) highlighted for the first-time interconnected drainage networks linked with smaller sinkholes, secluded sinkholes

and canyons in the Gipsdalen Formation, Norway. Cai et al. (2011) demonstrated that low frequency anomalies may be correlated with paleokarst oil reservoirs. Ahlborn et al. (2014) blended three frequencies (26-30-35 Hz) to enhance paleokarst imaging. Qi et al. (2014) showed SD was useful to distinguish paleokarst caves, cave edges, internal discontinuities, and valleys in the Ellenburger Formation of the Fort Worth Basin. Basso (2018) used 20-40-65 Hz spectral components to highlight sinkholes in the Campos Basin, Brazil (Figure 2.7d).

Amplitude

Root mean square (RMS) amplitude is the square root of the average trace energy (Barnes et al., 2016). In paleokarst settings where automatic, or even manual, horizon tracking can be very difficult, it may be much more robust to convert seismic amplitude to short window RMS amplitude then autotrack. Ahlborn et al. (2014) used RMS amplitude to identify ‘regions with low amplitudes synonymous with intense karstification. Li et al. (2016) and Sun et al. (2016) delineated regions with bright spots, or bead-like reflections (Sun et al., 2016) in the Ordovician cavernous carbonate reservoirs in the Tarim Basin, China. Such paleokarst bright spots may be oil filled or water filled (Li et al., 2016 and Sun et al., 2016) (Figure 2.13).

Chaos

The Chaos attribute has been used to reveal sinkhole infill (Ahlborn et al., 2014) and define internal sinkhole geometry. Russel-Houston and Gray (2014) used a multi-trace chaos attribute to define the chaotic nature of sinkhole internal geometry in the Devonian Grosmont Formation, Canada, using chaos co-rendered with a time structure map (Figure 2.14)

Dip Magnitude / Dip Azimuth

Dip magnitude is the “angle a planar reflection makes with the horizontal" (Barnes, 2016). Hunt et al., (2003, 2010) characterized the variability within the Gipsdalen Formation

showing karst channels controlled by fracture and faults, sinkholes, and paleo caverns from carbonate polygonal buildup. Based on dip attributes, Hunt et al. (2003) recognized that paleokarst features correspond to poor reflector continuity areas and found sinkholes at the intersection of faults. Qi et al. (2014) used dip attributes to map karst boundaries and fault extent in the Ellenburger Formation in the Fort Worth Basin. Qi et al. (2014) used a plot of dip azimuth with a cyclic color bar revealed that reflectors dip into the collapse features. Figure 2.15 shows dip magnitude/azimuth for sinkholes in the Ordovician Viola Limestone in the Arkoma Basin. The sinkholes show greater dip in the sinkhole interior than exterior.

Amplitude Gradients

The energy-weighted coherent amplitude gradient is an amplitude variability measurement of only the coherent component of the seismic data (Chopra and Marfurt, 2007). Energy-weighted coherent-amplitude gradients reveal features that show changes in thin bed tuning, such as thin meandering channels that are associated with collapse features and valleys, providing evidence of subaerial exposure (Sullivan et al., 2006).

Multi-Trace Attributes

Hunt et al. (2003, 2010) and Sayago et al. (2011, 2012) used a multi-trace volume seismic attribute (envelope, dominant frequency, chaos, gradient magnitude, instantaneous bandwidth, and variance) with artificial neural networks to discriminate paleokarst. Roy et al. (2013) used supervised and unsupervised classification to delineate less dense regions in the Mississippi Lime. Basso et al. (2018) used self-organizing maps to highlight paleokarst in the Campos Basin, Brazil (Figure 2.7e).

Rock Physics and Prestack Seismic

Rock/Fluid Properties and Seismic Response

The lateral extension of paleokarst can be delineated by prestack amplitude analysis (Fontaine et al., 1987) using near and far offset ratios to distinguish between zones with and without karst. (Figure 2.16). The magnitude of the reflection event as a function of offset is strongly affected by Poisson's ratio, and a relationship exists between Poisson's ratio and changes in limestone porosity, and paleokarst can lower limestone density affecting the relative magnitude of limestone reflection events (Vandenberghe et al., 1983).

Purves et al. (1992) used poststack amplitude variations sensitive to rock property changes to distinguish dense cave pillars, solution collapse breccias, and cave fill, noting higher production (> 2 MMBO/well) in solution collapsed breccias. In the Hobbs Field, New Mexico, Zeng et al. (2006) found that paleocaves existed in high impedance carbonates with low interparticle porosity and permeability.

Seismic amplitude bright spots can suggest a collapsed paleocave system (Zeng 2011a, 2011b) whose presence and geometry are good indicators of collapse extent and fault/fracture density as verified by core data that exhibits low gamma ray, low impedance zones corresponding with clastic cave sediment fill (Figure 2.17) as observed in the Tarim Basin, China. Seismic amplitude anomalies for caves are associated with different scales of collapse from minor to moderate to extensive collapse. Minor collapse has been defined as fault offsets less than 10 m in a paleocave complex with a thickness of 30 m and a width of 100 - 200 m. Minor collapse is linked with regional fracture networks. Moderate collapse bright spots are V shaped, indicating caves 200 - 500 m wide with vertical displacement of 50-150 m, and sag structures are noticeable in younger strata. Large collapse shows V shaped bright spots for caves

500-5000 m wide and a thickness of 300 m (Zeng et al., 2011a). In China's Tarim Basin, wells drilled through collapse bright spot reflections encountered disturbed rocks interpreted as paleocave infill (Zeng et al., 2010).

Cavern carbonate reservoirs that are oil-filled show decreasing peak time with increasing frequency, while brine saturated carbonate reservoirs do not show significant changes in peak time (Li et al., 2016).

Rock Physics Models

Rock physics models (RPMs) describe elastic parameters (V_P, V_S, density) as a function of mineralogy, pore fluid, pressure, temperature, and pore structure. Carbonate RPMs are a challenge because of strong dependence on pore types, such as intraparticle, interparticle, vuggy and moldic in limestone and dolomite. Clastic RPMs are far less dependent on pore structure having only intergranular pores (Xu and Payne, 2009). Xu and Payne (2009) and Liu et al. (2009) noted that pore shape may be the principal influence in carbonate rock physics. Xu and Payne (2009) proposed a carbonate rock physics model, which included various rock types, use of velocity and porosity data to estimate pore types, the influence of pore-types on Gassmann fluid substitution, and the impact of elastic properties and fluid flow anisotropy among fractures and matrix pores. Sun et al. (2011) reported the use of differential effective medium-Gassmann substitution to determine relationships between velocities, porosities, and pore shapes in carbonates of the Tarim Basin, China.

Mur and Vernik (2020) propose use of RPM for pore shapes, effective stress, mineralogy, porosity, and effective stress on elastic properties of limestones and dolomites with a porosity range as high as 45%. This technique shows that local geological description and observations can be used to calibrate the model in an unambiguous fashion.

Amplitude Variation with Offset and Frequency.

Sun et al. (2016) and Li et al. (2016) applied amplitude variation with offset frequency-dependent inversion for fluid detection giving evidence for distinguishing oil-filled versus water-filled caves in the Tarim Basin, China. Li et al. (2016) noted that oil-saturated cave reservoirs show strong attenuation to the high frequency spectral components at large offsets (incidence angles) and strong energies in the low frequency. However, brine saturated reservoirs do not show such phenomenon (Figure 2.18).

Prestack Elastic Inversion and Full Waveform Inversion (FWI)

Prestack elastic inversion extends poststack acoustic impedance inversion by iteratively modeling amplitude variation with offset (AVO) to fit well calibration data (fullwave sonic, density) and deliver a dense grid of elastic parameters (V_P, V_S, density) throughout the 3D seismic volume. In the Devonian Grosmont Formation, Alberta Basin, Canada, Russel-Houston and Gray (2014) used a model-based prestack simultaneous inversion to estimate density which correlated to core data (Figure 2.19).

Tran et al. (2015) used full waveform tomography to outline low-velocity karst zones, extremely variable limestone, and a void confirmed by surface measurements at a karst site in Florida.

Drilling and Completion

Drilling and Production Problems in Paleokarst Reservoirs

Paleokarst reservoirs usually have permeability systems with high fluid flow anisotropy and subtle flow regimes (Fontaine et al., 1987; Trice, 2005). Trice (2005) noted major porosity and permeability heterogeneities in paleokarst reservoirs are problematic to characterize and quantify, with spatial distributions difficult to predict and model away from well control.

Paleokarst wells with a large volume of mud loss, but circulation not totally lost, can become major producers, while those wells with minor fluid loss are generally poor to medium producers, and lower flow rates in mudstone are associated with narrower fractures with more tortuous connectivity (Daniel, 1954). Zhao et al. (2014) reported a sharp production and pressure decline curves for fracture dominated reservoirs, whereas vug-dominated reservoirs show relatively stable production and pressure with long-term production. Paleokarst water drive reservoirs may experience high production rates with turbulent flow leading to sharp increases in water cut and water coning (Fritz, 1991; Purdy and Waltham, 1999; Trice, 2005). Sinkholes cluster may contribute to poor production as reported in the Liuhua field of China (Story et al., 2010).

The recovery factor of hydrocarbons in paleokarst reservoirs depends on the strength of the water drive, matrix wettability, degree of matrix and fracture connectivity, and porosity development (Trice, 2005). Higher matrix porosity increases the delivery rate of matrix oil to the production stream, relative to fracture and karst conduit oil (Purdy and Waltham, 1999). Karst drainage systems have vertical and horizontal flow regimes fundamentally different than conventional layered or tectonically fractured reservoirs (Trice, 2005).

Common problems in paleokarst drilling for hydrocarbons include lost circulation (Andre and Doulcet, 1991; Lomando et al., 1993; Zhao et al., 2014), increased drilling rates (Varenicheva et al., 1973; Lomando et al., 1993), bit drops (Craig, 1988; Lomando et al., 1993; Demiralin, 1993; Dembicki and Machel,1996; Zhao et al., 2014), rushes of oil during drilling (Craig, 1988), extreme flow rates (Craig 1988; Viniegra O. and Castillo-Tejero, 1970; Yang et al., 2010), and rock fragments brought to the surface in oil moving through casing and flow lines (Craig, 1988). Drilling mud weight planning can be a challenge when drilling through paleokarst

because of rapid variation in porosity and permeability (Burberry et al., 2016), although paleokarst can enhance permeability and porosity of otherwise poor-quality reservoirs.

In paleokarst zones, logs may show low readings with cycle skipping on the acoustic log, enlargement of the caliper log, lower density, and lower resistivity with deep resistivity greater than shallow resistivity (Del Olmo and Esteban, 1983; Lomando et al., 1993; Dembicki and Machel, 1996; Zhao et al., 2014). In the Mississippian Chat of Northern Oklahoma, the shallow induction resistivity log has greater values than the deep induction log and low bulk density values (Rogers, 2001), while in the Tarim Basin formation micro image logs show mud fills and open vugs associated with high resistivity calcite (Zhao et al., 2014), and Middle East paleokarst reservoirs can show spectral gamma log indications of relatively high uranium counts associated with hypogene paleokarst (Trice, 2005).

Completion Methods in Paleokarst Reservoirs

Paleokarst washout washout can result in lost fluids and log interpretation difficulties for fluid contacts and fluid gradients. Barefoot completions (no casing or liner across the reservoir interval) are common, as are slotted or pre-drilled liners because of the incapacity to cement casing (Heward et al., 2000). In paleokarst reservoirs it can be tricky to reach a total depth (TD) of the well without encroaching water from underlying units. For example, for targeting Mississippian Chat in Northeast Oklahoma a typical workflow is: “Drill into the top of the Chat with rate of penetration closely monitored and bottom-up circulation to catch samples at 15- and 30-minutes intervals. The samples are evaluated for fluorescence, odor and hydrocarbon cut. Samples with less than ~50% bright gold fluorescence, strong petroliferous odor and flash cut with thick ring suggest additional drilling with the process repeated. However, drilling rate is less than 30 seconds/foot, stop drilling and circulate bottom up for samples. A drill rate of 30

seconds/foot shows a very high porosity up to 40%. For samples greater than 50% bright gold fluorescence, strong odor with flash cut and thick ring, a drill stem test should be considered (Matson, 2020 Pers. Comm).

Horizontal drilling in paleokarst has been active throughout the Mississippian Lime play of Northern Oklahoma. A typical well plan might read: “Land at the top of the tripolite at 80-degree inclination. Drill until you are confident you are at least 3 vertical feet below the top. Circulate hole and prepare to run an intermediate 7" casing to Total Depth (TD). Once the casing is cemented and ready, reenter well bore with bottom hole assembly and drill the lateral. Drilling rates of 120 feet/hour are possible, but should be avoided. Too fast of a rate causes problems keeping the hole clean of cuttings. Too many cuttings can cause drill string pipe to stick. Catch and evaluate samples every 20'. Keep samples organized and out for 1000' intervals. Allow to dry in a darkened room. Utilize ultraviolet light to evaluate how fluorescence changes over time. Rock cuttings that lose fluorescence quickly are often higher porosity and permeability. Mapping and targeting the lenses of higher porosity and permeability is possible. When TD is reached, circulate hole clean and lay down pipe” (Shane Matson, personal communication, 2020).

Conclusion

A review of available literature reveals a global distribution of paleokarst reservoirs revealed and developed using 3D seismic data and well logs. Sinkholes, tower karst, canyons, valleys, and vertical collapse paleokarst landforms have been identified and characterized on seismic data. Millions (if not billions) of barrels of hydrocarbons have been produced from karst reservoirs in the Neoproterozoic to the Miocene. Seismic attributes such as coherence, RMS amplitude, isopach, isochron maps, variance, and acoustic impedance have been successfully used to characterize and delineate paleokarst features. Bright isolated amplitudes in carbonate

intervals can suggest the presence of paleocave collapse features. Seismic modeling -- physical, wave and ray tracing -- provides an understanding of observed subsurface paleokarst features and their characteristic scales. The literature provides insight to the nature and understanding of paleokarst reservoirs on a seismic scale.

References

Aboaba, O. and C. Liner, 2018, 3D seismic interpretation of Paleozoic paleokarst features in the Arkoma Basin: 88th Annual International Meeting, SEG, Expanded Abstracts, 1698-1702, doi. 10.1190/segam2018-2998630.1.

Aboaba O., and C. Liner, 2019, 3-D Seismic Characterization of Paleokarst Collapse Features in the Arkoma Basin, Oklahoma: AAPG Search and Discovery Article #90350.

Aboaba, O. and C. Liner, 2020, Interpretation of Paleozoic paleokarst features in the Arkoma Basin of Oklahoma using 3D seismic and well logs: Interpretation, **8**, no. 2, 1-20, doi: 10/1190/INT-2019-0155.

Andre, P., and A. Doulcet, 1991, Rospo Mare Field — Italy Apulian Platform, Adriatic Sea, in N. H. Foster and E. A. Beaumont, eds., Stratigraphic traps II: AAPG Treatise of Petroleum Geology, Atlas of Oil and Gas Fields: American Association of Petroleum Geologists, 29–54.

Aves, H. S., and D. M. Tappmeyer, 1985, The use of synthetic sonic logs derived from seismic data in the interpretation of stratigraphic variation in Cretaceous carbonates of the North Field area, Qatar, *in* O. R. Berg and D. G. Woolverton, eds., Seismic Stratigraphy II: An integrated approach to hydrocarbon exploration: AAPG Memoir 39, 241–253.

Ahlborn, M., L. Stemmerik, T.-K., Kalstø, 2014, 3D seismic analysis of karstified interbedded carbonates and evaporites, Lower Permian Gipsdalen Group, Loppa High, southwestern Barents Sea: Marine and Petroleum Geology, **56**, 16–33, doi: 10.1016/j.marpetgeo.2014.02.015.

Alberta Energy Regulator, 2015, ST98-2015: Alberta's energy reserves 2014 and supply/demand outlook 2015–2024: Alberta Energy Regulator.

Al-Dossary, S., and K. J. Marfurt, 2006, 3D volumetric multispectral estimates of reflector curvature and rotation: Geophysics, **71**, no. 5, P41–P51, doi: 10.1190/1.2242449.

Alessio, L., S. Coca, and L. Bourdon, 2005, Experimental design as a framework for multiple realization history matching: F6 further development studies: SPE 93164, Asia Pacific Oil and Gas Conference and Exhibition, doi: 10.2118/93164-MS.

Amthor, J. E., and G. M. Friedman, 1989, Petrophysical character of Ellenburger karst facies: Stateline (Ellenburger) field, Lea County, southeastern New Mexico, *in* B. K. Cunningham and D.W. Cromwell, eds., The Lower Paleozoic of west Texas and southern New Mexico - Modern exploration concepts: PBS-SEPM Publication 89-31, 133–144.

Bahorich, M., and S. Farmer, 1995, 3-D seismic discontinuity for faults and stratigraphic features: The coherence cube: The Leading Edge, **14**, 1053–1058, doi: 10.1190/1.1437077.

Balint, V., and F. Pach, 1984, Depletion experiences and modeling of mixed-porosity, fractured, cavernous reservoirs in Hungary: 59th Annual Technical Conference and Exhibition, SPE, Conference Paper, SPE 13186, 1–11, doi: 10.2118/13186-MS.

Barber, R., and K. Marfurt, 2009, Attribute delineation of karst - calibration via elastic wave-equation modeling: 79th Annual International Meeting, SEG, Expanded Abstracts, 2627-2321, doi: 10.1190/1.3255392.

Barnes, A. E., 2016, Handbook of poststack seismic attributes: SEG Geophysical reference series 21, doi: 10.1190/1.9781560803324.

Barnett, A. J., V. P. Wright, V. S. Chandra, and V. Jain, 2015, Distinguishing between eogenetic, unconformity-related and mesogenetic dissolution: a case study from the Panna and Mukta fields, offshore Mumbai, India: Geological Society of London Special Publications, **435**, 67–84.

Basso, M., M. C. Kuroda, L. C. S. Afonso, and A. C. Vidal, 2018, Three-dimensional seismic geomorphology of paleokarst in the Cretaceous Macaé group carbonates, Campos basin, Brazil, Journal of Petroleum Geology, **41**, 512–526.

Bebout, D. G. and R. G. Loucks, 1974, Stuart City Trend, Lower Cretaceous, south Texas.: Bureau of Economic Geology, University of Texas-Austin, Report of Investigations, **78**, 1–80.

Bentley, J., 1984, Petroleum geology of the central Broome platform, *in* P. G. Purcell, ed., The Canning basin, Western Australia: Proceedings Geological Society of Australia and Petroleum Exploration Society of Australia, Canning Basin Symposium, 157–168.

Birt, C., B. Boyd, A. Nugraha, 2015, Evolution and karstification of the Eocene-Miocene carbonates overlying the Tangguh gas fields in western Papua – Observations from 3D seismic and impact on drilling operations: 39th Annual Convention and Exhibition, International Petroleum Association, Proceedings, IPA, IPA15-G-302, 1–17.

Bliefnick, D. M. and W. C. Belfield, 1991, The Ordovician Arbuckle Group of Oklahoma - a karsted dolomite reservoir, *in* A. Bosellini et al., eds., Abstracts, Dolomieu Conference on Carbonate Platform and Dolomitization, 17–18.

Bliefnick, D. M., 1992, Karst-related diagenesis and reservoir development in the Arbuckle Group, Paschall #2 core, Wilburton field, in M. P. Candelaria and C. L. Reed, eds., Paleokarst, karst-related diagenesis, and reservoir development: Examples from Ordovician-Devonian age strata of west Texas and the Mid-continent: SEPM Publication 92-33, 137–152.

Brady, T.J., Campbell, N.D.J. and Maher, C.E., 1980. Intisar "D" oil field, Libya, *in* M. T. Halbouty, ed., Giant oil and gas fields of the decade: 1968-1978: AAPG Memoir 30, 543– 564.

Bramlette, M. N., 1946, The Monterey Formation of California and the origin of its siliceous rocks: USGS Professional Paper 212, 1–57.

Brown, A. R., 1985, The role of horizontal seismic sections in stratigraphic interpretation, *in* O. R. Berg and D. G. Woolverton, eds., Seismic stratigraphy II: An integrated approach to hydrocarbon exploration: AAPG Memoir 39, 37–47.

Burberry, C. M., S. R. Chandler, and C. A. L. Jackson, 2015, Seismic expression of karst-related features in the Persian Gulf and implications for characterization of carbonate reservoirs: AAPG Annual Convention and Exhibition, Search and Discovery Article #30411.

Burberry, C. M., C. A. L Jackson, and S. R. Chandler, 2016, Seismic reflection imaging of karst in the Persian Gulf: Implications for the characterization of carbonate reservoirs: AAPG Bulletin, **100**, 1561–1584, doi: 10.1306/04151615115.

Cai, R., and Y. Sun, 2011, Seismic analysis using wavelet transform for hydrocarbon detection in paleo-karst reservoirs: 81st Annual International Meeting, SEG, Expanded Abstracts, 1052–1056, doi: 10.1190/1.3627385.

Canter, K. L., D. M. Wheeler, and R. C. Geesaman, 1992. Sequence stratigraphy and depositional facies of the Siluro-Devonian interval of the northern Permian Basin, *in* M. P. Candelaria and C. L. Reed, eds., Paleokarst, karst related diagenesis and reservoir development: Examples from Ordovician-Devonian age strata of west Texas and the mid-continent: PBS-SEPM 92-33, 93–109.

Cantrell, D. J., R. A. Shah, J. Ou, C. Xu, C. Phillips, X. L. Li, T. M. Hu, 2020, Depositional and diagenetic controls on reservoir quality: Example from the upper Cretaceous Mishrif Formation of Iraq: Marine and Petroleum Geology, **118**, 1–34, doi: 10.1016/j.marpetgeo.2020.104415

Carpenter, B.N. and M. E. Evans, 1991, Comparison of the Arbuckle Group at Wilburton Field, Latimer County, with N. E. Alden Field, Caddo County, Oklahoma, *in* K. S. Johnson, ed.,

Arbuckle Group Core Workshop and Field Trip: OGS Special Publication, 91-3, 111–132.

Cartwright J., M. Huuse and A. Aplin, 2007, Seal bypass systems: AAPG Bulletin, **91**, 1141–1166, doi: 10.1306/04090705181.

Castillo M. N, and P. Mann, 2006, Deeply buried, Early Cretaceous paleokarst terrane, southern Maracaibo Basin, Venezuela: AAPG Bulletin, **90**, 569–579, doi: 10.1306/10120505034.

Catacosinos, P.A., P. A. Daniels, and W. B. Harrison, 1990, Structure, stratigraphy, and petroleum geology of the Michigan Basin *in* M. W. Leighton, D. R. Kolata, D. F. Oltz and J. J. Eidel, eds., Interior cratonic basins: AAPG Memoir 51, 561–602.

Chakraborty, A., and D. Okaya, 1995, Frequency-time, decomposition of seismic data using wavelet-based methods: Geophysics, **60**, 1906–1916.

Chopra, S., and K. J. Marfurt, 2007, Seismic attributes for prospect identification and reservoir characterization: SEG Geophysical developments series, no. 11, doi: 10.1190/1.9781560801900.

Chung E., T. K. King, and O. AlJaadi, 2011, Karst modeling of a Miocene carbonate build-up in central Luconia, SE Asia: Challenges in seismic characterization and geological model building: IPTC 14539, 1–6.

Coogan, A. H., D. G. Bebout, and C. Maggio, 1972, Depositional environments and geological history of Golden Lane and Poza Rica trends, Mexico, an alternative view: AAPG Bulletin, **56**, 1419–1447.

Corral, A., and A. Gonzalez, 2019, Power-law size distributions in geoscience revisited: Earth and Space Science, 673–697, doi: 10.1029/2018EA000479.

Craig, D. H., 1988, Caves and other features of Permian karst in San Andres dolomite, Yates field reservoir, west Texas, *in* N. P. James and P. W. Choquette, eds., Paleokarst: Springer–Verlag.

Craig, D. H., D. H. Mruk, M. J. Heymans, P. D. Crevello, and R. C. Lanz, 1986, Stratigraphy and reservoir geology of the San Andres Dolomite, Yates Field, west Texas, *in* D. G. Bebout and P. M. Harris, eds., Hydrocarbon reservoir studies, San Andres/Grayburg Formations, Permian Basin: PBS-SEPM Publication 86-26, 139–143.

Cunningham, K. J., and C. Walker, 2009, Seismic-sag structural systems in Tertiary carbonate rocks beneath southeastern Florida, USA: Evidence for hypogenic speleogenesis? in A. B. Klimchouk and D. C. Ford, eds., Hypogene speloeogenesis and karst hydrogeology of Artesian Basins: Ukrainian Institute of Speleology and Karstology, Special Paper 1, **280**, 151–158.

Daniel, E. J., 1954, Fractured reservoirs of Middle East: AAPG Bulletin, **38**, 774–815.

Dolly, E. D., and D. A. Busch, 1972, Stratigraphic, structural, and geomorphologic factors controlling oil accumulation in Upper Cambrian strata of central Ohio: AAPG Bulletin, **56**, 2335–2368.

Del Olmo, W. M., and M. Esteban, 1983, Paleokarst development, *in* R. A. Scholle, D. G. Bebout, and C. H. Moore, eds., Carbonate depositional environments: AAPG Memoir 33, 93–95.

Dembicki, E. A., and H. G. Machel, 1996, Recognition and delineation of paleokarst zones by the use of wireline logs in the bitumen-saturated upper Devonian Grosmont Formation of northeastern Alberta, Canada: AAPG Bulletin, **80**, 695–712.

Demiralin, A. S., N. F. Hurley, and T. W. Oesleby, 1993, Karst breccias in the Madison Limestone (Mississippian), Garland field, Wyoming, *in* R. D. Fritz, J. L. Wilson, and D. A. Yurewicz, eds., Paleokarst related hydrocarbon reservoirs: SEPM Core Workshop 18, 101–118.

Duo Q., Y. Sun, C. Sullivan, and H. Guo, 2011, Paleokarst system development in the San Andres Formation, Permian Basin, revealed by seismic characterization: Journal of Applied Geophysics, **75**, 379–389, doi: 10.1016/j.jappgeo.2011.08.003.

Dussert, P., G. Santoro, and H. Soudet, 1988, A decade of drilling developments pays off in offshore Italian oil field: Oil & gas journal, 33–39.

Ebanks, W. J., R. M. Euwer, and D. E. Nodine-Zeller, 1977, Mississippian combination trap, Bindley Field, Hodgeman County, Kansas: AAPG Bulletin, **61**, 309–330.

Edie, R. W., 1958, Mississippian sedimentation and oil fields in southeastern Saskatchewan, *in* A. G. Goodman, ed., Jurassic and Carboniferous of western Canada: AAPG John Andrew Allen Memorial Volume, 331–363.

Esteban, M., 1991, Palaeokarst: practical applications (chapter 3) and case histories, *in* V. P. Wright, M. Esteban and P. L. Smart, eds., Palaeokarsts and palaeokarstic reservoirs: Postgraduate research institute for sedimentology, University of Reading, 89–146.

Esteban, M., and C. F. Klappa, 1983, Subaerial exposure environments, in Scholle, P. A., Bebout, D. G. and Moore, C. H., eds., Carbonate depositional environments: AAPG Memoir 33, 1–54.

Fernandez, A., and K. Marfurt, 2013, Detailed seismic characterization of a heavily karsted zone: AAPG Search and Discovery #10506.

Fontaine, J. M., R. Cussey, J. Lacaze, R. Lanaude, and L. Yapaudjian, 1987, Seismic interpretation of carbonate depositional environments: AAPG Bulletin, **71**, no. 3, 281 – 297.

Ford D. and P. Williams, 2007, Karst hydrogeology and geomorphology: John Wiley and Sons, doi: 10.1002/9781118684986.

Fritz, M., 1991. "It's all there" in the Knox Play: AAPG Explorer, 1.

Fritz, R. D., 1991, Paleokarst Targets, *in* R. D. Fritz, M. K. Horn, S. D. Joshi, eds., Geological aspects of horizontal drilling: AAPG course note series 33, 327–347.

Garcia-Sineriz, B., R. Querol, F. Castillo, and J. R. F. Arribas, 1980, A new hydrocarbon province in the western Mediterranean: l0th WPC, Proceedings, **2**, 191- 197.

Garfield, T. R., and M. W., Longman, 1989, Depositional variations in the Fusselman Formation central Midland Basin, west Texas, *in* B. K. Cunningham and D. W. Cromwell, eds., The Lower Paleozoic of west Texas and Southern New Mexico-Modern exploration concepts: PBS-SEPM Publication 89-31, 187–202.

Gatewood, L.E., 1970: Oklahoma City Field-- anatomy of a giant, *in* M. T. Halbouty, ed., Geology of Giant Petroleum Fields: AAPG Memoir 14, 223–254.

Geesaman, R. C. and A. J. Scott, 1989. Stratigraphy, lithofacies, and depositional models of the Fusselman Formation, central Midland Basin, *in* B. K. Cunningham and D. W. Cromwell, eds., The Lower Paleozoic of west Texas and Southern New Mexico - Modern exploration concepts: PBS-SEPM Publication 89-31, 175–186.

Gill, D., 1985, Depositional facies of Middle Silurian (Niagaran) pinnacle reefs Belle River Mills Gas Field, Michigan Basin, southeastern Michigan, *in* P.O. Roehl and P.W. Choquette, eds., Carbonate Petroleum Reservoirs*:* Springer-Verlag, 121–139.

Guangming, Z. and Quanheng, Z., 1982. Buried-hill oil and gas pools in the North China Basin, i*n* M. T. Halbouty, ed., The deliberate search for the subtle trap: AAPG Memoir 32, 317–335.

Hardage, B., D. Carr, D. Lancaster, J. Simmons, Jr., R. Elphick, V. Pendleton, and R. Johns, 1996, 3D seismic evidence of the effects of carbonate karst collapse on overlying clastic stratigraphy and reservoir compartmentalization: Geophysics, **61**, 1336–1350, doi: 10.1190/1.1444057.

Harris, P. M., and S. H. Frost, 1984, Middle Cretaceous carbonate reservoirs, Fahud Field and northwestern Oman: AAPG Bulletin, **68***,* 649–658.

Harris, P. M., P. E. Flynn, and J. L. Sieverding, 1988, Mission Canyon (Mississippian) reservoir study, Whitney Canyon-Carter Creek Field, southwestern Wyoming, *in* A. J. Lomando and P. M. Harris, eds., Giant oil and gas fields, a core workshop: SEPM Core Workshop 12, 695–740.

Harvey, R. L., 1972, West Campbell (Northeast Cedardale) Gas Field, Major County, Oklahoma, *in* R. E. King, ed., Stratigraphic oil and gas fields: AAPG Memoir 16, 568–678.

Henderson, K. S., and S. C. Knox, 1991, Hydrocarbon potential and subsurface stratigraphy of the Cambro-Ordovician sequence, Black Warrior Basin of Mississippi, *in* K. S. Johnson, ed., Arbuckle Group Core Workshop and Field Trip: OGS Special Publication 91-3, 181–184.

Heubeck, C., K. Story, P. Peng, C. Sullivan, and S. Duff, 2004, An integrated reservoir study of the Liuhua 11-1 field using a high-resolution three-dimensional seismic data set, in G. P. Eberli, J. L. Masaferro, and J. F. "Rick" Sarg, eds., Seismic imaging of carbonate reservoirs and systems: AAPG Memoir 81, 149–168.

Heward, A. P., S. Chuenbunchom, G. Makel, D. Marsland, and L. Spring, 2000, Nuan oil field, B6/27, Gulf of Thailand: Karst reservoirs of meteoric or deep-burial origin?: Petroleum Geoscience, **6**, 15–27.

Hill, C. A., 1990, Sulfuric acid speleogenesis of Carlsbad cavern and its relationship to hydrocarbons, Delaware Basin, New Mexico and Texas: AAPG Bulletin, **74**, 1685–1694

Hill, C. A., 1995, H2S related porosity and sulfuric acid oil-field karst, *in* D. A. Budd, A. H. Saller, and P. M. Harris, eds., Unconformities and porosity in carbonate strata: AAPG Memoir 63, 301–306.

Holtz, M. H. and C. Kerans, 1992. Characterization and categorization of west Texas Ellenburger reservoirs, *in* M.P. Candelaria and C.L. Reed, eds., Paleokarst, karst related diagenesis and reservoir development: Examples from Ordovician-Devonian age strata of west Texas and the Mid-Continent: PBS-SEPM Publication 92 33, 45–54.

Hook, R. C., 1990, Recent developments at Wilburton Field, Latimer County, Oklahoma: AAPG Bulletin, **74**, 677.

Hovorka, S. D. and S. C. Ruppel, 1990, Controls on porosity evolution in Devonian cherts of west Texas: AAPG Bulletin, **74**, 678.

Hu, B. L., 1992, Petroleum geology and prospects of the Tarim basin, China, *in* M. T. Halbouty, ed., Giant oil and gas fields of the decade 1978–1988: AAPG Memoir 54, 493–510.

Hunt, D., G. Elvebakk, B. Rafaelsen, J. Pajchel, K. Hogstad, and H. Robak, 2003, Palaeokarst recognition & 3D distribution – new insights from the Upper Palaeozoic, Loppa high, Barents Sea: 65th Conference and Exhibition, EAGE, Extended Abstracts, 1–4, doi: 10.3997/2214-4609-pdb.6.P032.

Hunt, D., A. Colpaert, F. Miquelis, B. Graham-Wall, J. Pajchel, J. Lukasik, B. Rafaelsen, A. Avu, G. Patton, 2010, Seismic geomorphology of paleokarst systems in Paleozoic carbonates, Norwegian Barents Sea, *in* L. J. Wood, T. T. Simo, and N. C. Rosen, eds.,

Seismic imaging of depositional and geomorphic systems: 30th Annual GCSSEPM Foundation Annual Bob F. Perkins Research Conference Proceedings, **30**, 184–206, doi: 10.5724/gcs.10.30.0184.

Ijirigho, B.T. and Schreiber, J.F., 1988. Composite classification of fractured and brecciated carbonate rocks - examples from the Ordovician Ellenburger Group, west Texas: Journal of Petroleum Geology, **11**, 193–204.

Illing, L.V., G. V. Wood, and J. G. C. M. Fuller, 1967, Reservoir rocks and stratigraphic traps in non-reef carbonates: 7th World Petroleum Congress Proceedings, **2**, 487–499.

James, N. P., and P. W. Choquette, 1988, Paleokarst: Springer-Verlag.

Jordan, C. F., T. C. Connally, and H. A. Vest, 1985, Middle Cretaceous carbonates of the Mishrif Formation, Fateh Field, offshore Dubai, U.A.E, *in* P. O. Roehl and P.W. Choquette, eds., Carbonate petroleum reservoirs: Springer-Verlag, 426– 442.

Karajas, J., and C. N. Kernick, 1984, A prospective Nita Formation reservoir trend on the Broome platform, *in* P. G. Purcell, ed., The Canning basin, Western Australia: Proceedings Geological Society of Australia and Petroleum Exploration Society of Australia, Canning Basin Symposium, 169–177.

Keeling, R. M., 2016, Stratigraphic interpretation and reservoir implications of the Arbuckle Group (Cambrian-Ordovician) using 3D seismic, Osage County, Oklahoma: M.S. Thesis, University of Arkansas.

Kent, D. M., F. M. Haidl, and J. A. MacEachern, 1988, Mississippian oilfields in the northern Williston Basin, *in* S. M. Goolsby and M. W. Longman, eds., Occurrence and petrophysical properties of carbonate reservoirs in the Rocky Mountain region: RMAG, 381–418.

Kerans, C., 1988, Karst-controlled reservoir heterogeneity in Ellenburger Group carbonates of west Texas. AAPG Bulletin, **72**, 1160–1183, doi: 10.1306/0C9B2439-1710-11D7-8645000102C1865D.

Kerans, C., 1989, Karst-controlled reservoir heterogeneity and an example from the Ellenburger (Lower Ordovician) of west Texas: The University of Texas at Austin, Bureau of Economic Geology, Report of Investigations no. 186, 1–40.

Kerans, C., 1991. Description and interpretation of karst-related breccia fabrics, Ellenburger Group, west Texas, *in* K. S. Johnson, ed., Arbuckle Group Core Workshop and Field Trip: OGS Special Publication 91-3, 145–156.

Kerans, C. and Parsley, M.J., 1986. Depositional facies and porosity evolution in a karst-modified San Andres reservoir, Taylor Link West San Andres, Pecos County, Texas, *in* D. G. Bebout and P. M. Harris, eds., Hydrocarbon reservoir studies, San Andres/Grayburg Formations, Permian Basin: PBS-SEPM 86-26, 133–134.

Khutorov, A. M., 1958, The formation of secondary oil deposits in the Fergana depression: Geologiya Nefti i Gaza, **2**, 7B: 643– 651.

Kilcoyne, D., 2018, Mapping Lower Austin Chalk secondary porosity using modern 3-D seismic and well log methods in Zavala County, Texas: M.S. thesis, University of Arkansas.

Klimchouk, A. B., 2007, Hypogene speleogenesis: Hydrogeological and morphogenetic perspective. Special Paper no 1: National Cave and Karst Research Institute, 106.

Kosters, M., P. F. Hague, R. A. Hoffman, and B. L. Hughes, 2008, Integrated modelling of karstification of a Central Luconia field, Sarawak, Malaysia: IPTC, Conference Paper, IPTC 12327, 1–9.

Kruger, J.M., 1992, Diagenesis and porosity development beneath the pre-Kaskaskia (Early Devonian) interregional unconformity, northwest Illinois Basin, *in* M. P. Candelaria and C. L. Reed, eds., Paleokarst, karst related diagenesis and reservoir development: Examples from Ordovician-Devonian age strata of west Texas and the Mid-Continent: PBS-SEPM Publication 92-33, 182–191.

Kumbalek, M., 2015, Analysis of paleokarst sinkholes in the Arkoma Basin using 3-D seismic: M.S. thesis, University of Arkansas.

Kupecz, J.A., 1992. Sequence boundary control on hydrocarbon reservoir development, Ellenburger Group, Texas, *in* M. P. Candelaria and C. L. Reed, eds., Paleokarst, karst related diagenesis and reservoir development: Examples from Ordovician-Devonian age strata of west Texas and the Mid-Continent: PBS-SEPM Publication 92-33, 55–58.

Ladwein, H. W., 1988, Organic geochemistry of Vienna Basin: Model for hydrocarbon generation in overthrust belts: AAPG Bulletin, **72**, 586–599.

Latham, J.W, 1970. Petroleum geology of Healdton Field, Carter County, Oklahoma, *in* M. T. Halbouty, ed., Geology of giant petroleum fields: AAPG Memoir 14, 255–276.

Li, M., G. Taisheng, Z. Xueping, Z. Taijun, G. Rong, and D. Zhenrong, 1982, Oil basins and subtle traps in the eastern part of China, *in* M.T. Halbouty, ed., The Deliberate search for the subtle trap: AAPG Memoir 32, 287–315.

Li, Y., L. Zhang, D. Wang, S. Shi, and X. Cui, 2016, Hydrocarbon detection for Ordovician carbonate reservoir using amplitude variation with offset and spectral decomposition: Interpretation, **4**, no. 3, SN11–SN30, doi: 10.1190/INT-2015-0135.1.

Li, T., G. Deng, Z. Wang, and H. Zang, 2017, The study of seismic inversion in paleokarst reservoir: 87th Annual International Meeting, SEG, Expanded Abstracts, 3027–3031, doi: 10.1190/segam2017-17747781.1.

Liu, E., M. A. Payne, S. Xu, G. Baechle, and C. E. Harris, 2009, Carbonate rock physics issues, International Petroleum Technology Conference, doi: 10.2523/13850-MS.

Loh, F. C., B. L. Chuah, J. Zhou, T. Manning, S. Wolfarth, D. Priyambodo, 2016, Subsea detection and imaging improvement using full waveform inversion: 78th Conference and Exhibition, EAGE, Extended Abstracts, doi: 10.3997/2214-4609.201601188.

Lomando, A. J., P. M. Harris, and D. E. Orlopp, 1993, Casablanca Rield, Tarragona Basin, Offshore Spain: A karsted carbonate reservoir *in* R. D. Fritz, J. L. Wilson and D. A. Yurewicz, eds., Paleokarst hydrocarbon related reservoirs: SEPM Core Workshop 18, 1–9.

Loucks, R. G. and J. H. Anderson, 1985, Depositional facies, diagenetic terranes, and porosity development in Lower Ordovician Ellenburger Dolomite, Puckett Field, west Texas *in* P. O. Roehl, and P. W. Choquette, eds., Carbonate petroleum reservoirs: Springer-Verlag, 19–38.

Loucks, R. G. and C. R. Handford, 1992. Origin and recogni tion of fractures, breccias, and sediment fills in paleocave-reservoir networks, *in* M. P. Candelaria and C. L. Reed, eds., Paleokarst, karst related diagenesis and reservoir development: Examples from Ordovician-Devonian age strata of west Texas and the Mid-Continent: PBS-SEPM Publication 92-33, 31–44.

Loucks, R. G., 1999, Paleocave carbonate reservoirs: Origins burial-depth modifications, spatial complexity, and reservoir implications: AAPG Bulletin, **83**, 1795–1834.

Loucks, R. G., 2003, Review of the Lower Ordovician Ellenburger Group of the Permian Basin, west Texas: Bureau of Economic Geology, 1–92.

Lowenstam, H. A., 1948, Marine Pool, Madison County, Illinois, Silurian reef producer *in* J. V. Howell, ed., Structure of typical American oil fields: AAPG Symposium 3, 153–189.

Lucia, F. J., 1995, Lower Paleozoic cavern development, collapse, and dolomitization, Franklin Mountains, El Paso, Texas, *in* D. A. Budd, A. H. Saller, and P. M. Harris, eds., Unconformities and porosity in carbonate strata: AAPG Memoir 63, 279–300.

Lynch, M., and Z. Al-Shaieb, 1991, Paleokarstic features and thermal overprints observed in some of the Arbuckle cores in Oklahoma. In: K.S. Johnson (Editor), Arbuckle Group Core Workshop and Field Trip: OGS Special Publication 91-3, 31–68.

Machel, H. G., M. L. Borrero, E. Dembicki, H. Huebscher, L. Ping, and Y. Zhao, 2014, The Grosmont: A complex dolomitized, fractured and karstified heavy oil reservoir in a Devonian carbonate-evaporite platform: AAPG Search and Discovery Article #10576.

Maksimovich, G. A. and V. N. Bykov, 1978, Karst of carbonate oil- and gas- bearing formations: Perm University Press.

Marafi, H., 1972, Newburg-South Westhope oil field, North Dakota, *in* R. E. King, ed., Stratigraphic oil and gas fields: AAPG Memoir 16, 633–640.

Martin, R., 1964. Buried hills hold key to new Mississippian pay in Canada: Oil & Gas Journal Oct 19, 158–162.

Martin, R., 1966, Paleogeomorphology and its application to exploration for oil and gas (with examples from western Canada): AAPG Bulletin, **50**, 2277–2311, doi: 10.1306/5D25B723-16C1-11D7-8645000102C1865D

Maslov, Y. P., 1945, To the question of phases of deposition and karstification of buried massifs of Ishimbay: lzv. Akad. Nauk SSSR, Ser. Geol., 88–100.

Matapour, Z., D. A. Karlsen, B. Lerch and, K. Backer-Owe, 2018, Petroleum occurrences in the carbonate lithologies of the Gohta and Alta discoveries in the Barents Sea, Arctic Norway: Petroleum Geoscience, **25,** 50–70, doi: 10.1144/petgeo2017-085.

Mazzullo, L. J., 1990a, Fusselman paleotopographic trap search pays off in the Midland Basin: Oil & gas journal, 98–102.

Mazzullo, L. J., 1990b, Implications of sub-Woodford geologic variations in the exploration for Silurian Devonian reservoirs in the Permian Basin, in J. E. Flis and R. C. Price, eds., Permian Basin oil and gas fields: Innovative ideas in exploration and development: WTGS Publication 90-87, 29–42.

Mazzullo, L. J., S. J. Mazzullo, and T. E. Durham, 1989, Geologic controls on reservoir development in Silurian and Devonian carbonates, northern Midland Basin, Texas. In: B.K. Cunningham and D.W. Cromwell, eds., The Lower Paleozoic of west Texas and southern New Mexico - Modern exploration concepts: PBS-SEPM Publication 89-31, 209–218.

Mazzullo, S. J., 1986, Stratigraphic approaches to hydrocarbon exploration and exploitation: Journal of Geology, **21**, 265–281.

Mazzullo, S. J, 1989a, Formational and zonal subdivisions of the Ellenburger Group (Lower Ordovician), southern Midland Basin, Texas, *in* B. K. Cunningham and D. W. Cromwell, eds., The Lower Paleozoic of west Texas and southern New Mexico - Modern Exploration Concepts: PBS-SEPM Publication, 89–31:113–121.

Mazzullo, S. J., 1989b, Subtle traps in Ordovician to Permian carbonate petroleum reservoirs Permian Basin: an overview, *in* J.E. Flis, R. C. Price and J. F. Sarg, eds., Search for the Subtle Trap, Hydrocarbon Exploration in Mature Basins: WTGS Publication 89-85, 155–180.

Mazzullo, S.J., 1990. Karst-controlled reservoir heterogeneity in Ellenburger Group carbonates of west Texas: Discussion. AAPG Bulletin, **74**, 1119–1123.

Mazzullo, S. J. and L. J. Mazzullo, 1992. Paleokarst and karst-associated hydrocarbon reservoirs in the Fusselman Formation, west Texas, Permian Basin. In: M.P. Candelaria and C.L. Reed (Editors), Paleokarst, karst related diagenesis and reservoir development: Examples from Ordovician-Devonian age strata of west Texas and the mid-continent: PBS-SEPM Publication 92-33: l10–120.

Mazzullo, S. J., and G. V. Chilingarian, 1996, Hydrocarbon reservoirs in karsted carbonate rocks, 1996, *in* S.J. Mazzullo, H. H. Rieke, G.V. Chilingarian, eds., Carbonate reservoir characterization: In a geologic-engineering analysis, Part II, 44, 1st Ed. 797–865.

Mazzullo, S. J. and Reid, A. M., 1986, Belize, Central America: geologic models for certain Paleozoic reservoirs in the Permian Basin: WTGS Bulletin, **25**, 4–11.

McCaleb, J. A., 1988, Significance of paleokarst on petroleum recovery, Elk Basin Field, Big Horn Basin, *in* S. M. Goolsby and M. W. Longman, eds., Occurrence and petrophysical properties of carbonate reservoirs in the rocky mounta*in* region: RMAG, 139–147.

McCaleb, J. A. and D. A. Wayhan, 1969, Geologic reservoir analysis, Mississippian Madison Formation, Elk Basin Field, Wyoming-Montana: AAPG Bulletin*,* **53***,* 2094–2113.

McDonnell, A., R. G. Loucks, and T. Dooley, 2007, Quantifying the origin and geometry of circular sag structures in northern Fort Worth Basin, Texas: Paleocave collapse, pull-apart fault systems, or hydrothermal alteration?: AAPG Bulletin, **91**, 1295–1318, doi: 10.1306/05170706086.

Mear, C. E. and C. K. Dufurrena, 1984, Pre-Leonardian geology of Midland Farms Field area, Andrews County, Texas: AAPG southwest section Transactions 111–123.

Mear, C. E., 1989a, Ellenburger reservoir development at Midland Farms and Inez Fields, Andrews County, Texas, *in* B. K. Cunningham and D. W. Cromwell, eds., The Lower Paleozoic of west Texas and southern New Mexico - Modern exploration concepts: PBS-SEPM Publication 89-31, 169–174.

Mear, C. E., 1989b. Fusselman reservoir development at Flying W Field, Winkler County, Texas, *in* B. K. Cunningham and D.W. Cromwell, eds., The Lower Paleozoic of west Texas and southern New Mexico - Modern exploration concepts. PBS-SEPM Publication 89-31,203–207.

Mesolella, K. J., J.D. Robinson, L. M. McCormick, and A. R. Ormiston, 1974, Cyclic deposition of Silurian carbonates and evaporites in Michigan Basin: AAPG Bulletin **58**, 34–62.

Milad, B. M., and R. Slatt, 2017, Integrated 3-D seismic, outcrop, and core data for characterization of natural fractures of the Hunton limestone and the Woodford shale in Central Oklahoma: AAPG Search and Discovery Article #51382.

Miller, J. A., 1985, Depositional and reservoir facies of the Mississippian Leadville Formation, Northwest Lisbon field, Utah, *in* P. O. Roehl and P. W. Choquette, eds., Carbonate petroleum reservoirs: Springer-Verlag, 161–173.

Moser, D. J., 2016, 3D seismic interpretation of paleokarst sinkholes, Boone limestone, Lower Mississippian: Subsurface eastern Arkoma Basin, Conway County, Arkansas: M.S. thesis, University of Arkansas.

Mur, A., and L. V. Vernik, 2020, Rock physics modeling of carbonates: 90th Annual International Meeting, SEG, Expanded Abstracts, 2479–2483, doi: 10.1190/segam2020-3427703.1

Nadon, G. C. and G. L. Smith,1992, Identification of subaerial unconformities in the subsurface-an example from the Lower-Middle Ordovician of the central Michigan Basin, *in* M. P. Candelaria and C. L. Reed, eds., Paleokarst karst related diagenesis and reservoir development: examples from Ordovician-Devonian age strata of west Texas and the mid-continent: PBS-SEPM Publication 92-33, 153–164.

Newell, K. D., Watney, W.L., Cheng, S. W. L. and Brownrigg, R. L., 1987, Stratigraphic and spatial distribution of oil and gas production in Kansas: Subsurface Geology Series, **9**, 1–86.

Nissen, S. E, S. Bhattacharya, W. L. Watney, and J. H. Doveton, 2009, Improving geologic and engineering models of Midcontinent fracture and karst-modified reservoirs using new 3-D seismic attributes: Kansas Geological Survey Open-File Reports, 1–185, doi: 10.2172/967045.

Palmer A. N., 1991, Origin and morphology of limestone caves: GSA Bulletin, **103**, 1–21.

Purdy, E. G., and G. T. Bertram, 1993, Carbonate concepts from the Maldives, Indian Ocean: AAPG Studies in Geology 34, 7–55, doi: 10.1306/St34568.

Purdy, E. G., and D. Waltham, 1999, Reservoir implications of modern karst topography: AAPG Bulletin, **83**, 1774–1794.

Purves, W. J., J. E. Burnitt, L. R. Weathers, and L. K. Wipperman, 1992, Cave/pillar definition in the Ordovician Ellenburger reservoir by 3-D seismic, Pegasus field, Midland and Upton counties, Texas (abs.): AAPG Search and Discovery Article #91012.

Qi, F., and W. Xie-Pei, 1984, Significant role of structural fractures in Renqiu buried-hill oil field in eastern china, AAPG Bulletin, **68**, 971–982.

Qi, J., B. Zhang, H. Zhou, and K. Marfurt, 2014, Attribute expression of fault-controlled karst — Fort Worth Basin, Texas: A tutorial: Interpretation, **2**, no. 3, SF91–SF110.

Quanheng, Z., 1984. Jizhong Depression, China - its geologic framework, evolutionary history, and distribution of hydrocarbons: AAPG Bulletin, **68**, 983–992.

Rao, R. P., and S. N. Talukdar, 1980, Petroleum geology of Bombay High Field, India, *in* M. T. Halbouty, ed., Giant Oil and Gas Fields of the Decade: 1968 – 1978: AAPG Memoir 30, 487–506.

Raymond, D. E. and W. E. Osborne, 1991, Stratigraphy and exploration of the Knox Group in the Appalachian field and thrust belt and Black Warrior Basin of Alabama, *in* K.S. Johnson, ed., Arbuckle Group Core Workshop and Field Trip, OGS Special Publication 91-3, 163– 180.

Read, D. L. and W. O. Zogg, 1988, Description and origin of the Devonian dolomite oil reservoir, Grant Canyon Field, Nye County, Nevada, *in* S. M. Goolsby and M. W. Longman, eds., Occurrence and petrophysical properties of carbonate reservoirs in the rocky mountain region: RMAG, 229–240.

Reid, A. M. and Mazzullo, S. J., 1988, Paint Rock and Paint Rock Southwest Fields, Concho County, Texas: Strawn analogs of modem shelf island systems. WTGS Bulletin*,* **27**, no. 8: 5–10.

Reid, A., and S. A. T. Reid, 1991, The Cogdell Field study, Kent and Scurry Counties, Texas: A postmortem, *in* M. Candelaria, ed., Permian basin plays: Tomorrow 's technology today: WTGS Publication 91-89, 118–119.

Reid, A., S. A.T. Reid, and M. A. Mosley, 1991, Late Strawn and Early Canyon highstand and lowstand shelf edges and reefs on the Eastern Shelf with examples from Schleicher and Tom Green Counties, Texas, *in* M. Candelaria, ed., Permian Basin Plays: Tomorrow's technology today: WTGS Publication 91-89, 118–119.

Reid, A. M., S. A. Reid, and S. J. Mazzullo, 1990, Lowstand carbonate reservoirs: Upper Pennsylvanian sea level changes and reservoir development adjoining Horseshoe Atoll: AAPG Bulletin, **74**, 221.

Roberts, A., 2001, Curvature attributes and their applications: First break, **19**, 85–100, doi: 10.1046/j.0263-5046.2001.00142.x.

Roehl, P. O., 1985, Depositional and diagenetic controls on reservoir rock development and petrophysics in Silurian tidalites, Interlake Formation, Cabin Creek field area, Montana, *in* P. O. Roehl and P. W. Choquette, eds., Carbonate petroleum reservoirs: Springer-Verlag, 85–105.

Rogers, S. M., 2001, Deposition and diagenesis of Mississippian chat reservoirs, north-central Oklahoma: AAPG Bulletin, **85,** 115–129.

Rose, P. R., 1972, Edwards Group, surface, and subsurface, central Texas: University of Texas Austin, BEG, Report of investigations no. 74, 1–198.

Roy, A, B. L. Dowdell, and K. J. Marfurt, 2013, Characterizing a Mississippian tripolitic chert reservoir using 3D unsupervised and supervised multiattribute seismic facies analysis: An example from Osage County: Interpretation, **1**, no.2, SB109–SB124, doi: 10.1190/INT-2013-0023.1.

Russel-Houston, J., and K. Gray, 2014, Paleokarst in the Grosmont Formation and reservoir implications, Saleski, Alberta, Canada: Interpretation, **2**, no. 3, SF29–SF50, doi: 10.1190/int-2013-0187.1.

Saller, A. H., D. Van Horn, J. A. Miller, and B. T. Guy, 1991, Reservoir geology of Devonian carbonates and chert - implications for tertiary recovery, Dollarhide Field, Andrews County, Texas: AAPG Bulletin, **75**, 86–107.

Santiago-Acevedo, J., 1980, Giant fields of the southern zone, Mexico, *in* M. T. Halbouty, ed., Giant oil and gas fields of the decade: 1968-1978: AAPG Memoir 30, 339–385.

Sayago, J., M. D. Lucia, M. Mutti, A. Cotti, A. Sitta, and K. Broberg, 2011, 3D seismic mapping with attribute analysis and core data to detect paleokarst signatures in the Loppa High, Barents Sea: 73rd Conference and Exhibition, EAGE, Extended Abstracts, doi: 10.3997/2214-4609.20149126.

Sayago, J., M. D. Lucia, M. Mutti, A. Cotti, A. Sitta, K. Broberg, A. Przybylo, R. Buonaguro, and O. Zimina, 2012, Characterization of a deeply buried paleokarst terrain in the Loppa High using core data and multiattribute seismic facies classification: AAPG Bulletin, **96**, 1843–1866, doi: 10.1306/02271211137.

Sheriff, R. E., 2002, Encyclopedic dictionary of applied geophysics, 4th ed.: SEG, Geophysical References Series 13.

Shirley, K., 1988. Deeper zone rejuvenates old basin- Oklahoma Arbuckle targeted: AAPG Explorer, **9**, 10–13.

Sieverding, J. L. and P. M. Harris, 1991, Mixed carbonates and siliciclastics in a Mississippian paleokarst setting, southwestern Wyoming thrust belt, *in* A. J. Lomando, and P. M. Harris, eds., Mixed carbonate-siliciclastic sequences: SEPM Core Workshop 15: 541–568.

Sorkhabi, R., 2013, Kasaghan comes on stream, https://www.geoexpro.com/articles/2013/12/kashagan-comes-onstream, accessed 11 February 2019.

Spina, V., J. Borgomano, G. Nely, N. Shchukina, A. Irving, C. Neumann, and V. Neillo, 2015, Characterization of the Devonian Kharyaga carbonate platform (Russia): Integrated and multiscale approach: AAPG Bulletin, **99**, 1771–1799, doi: 10.1306/03031514119.

Stormont, D. H., 1949, Huge caverns encountered in Dollarhide Field make for unusual drilling conditions: Oil & Gas Journal, 66–68, 94.

Story, C., P. Peng, C. Heubeck, C. Sullivan, and J.D. Lin, 2000, Liuhua 11-1 Field, South China Sea: A shallow carbonate reservoir developed using ultrahigh-resolution 3-D seismic, inversion, and attribute-based reservoir modeling: The Leading Edge, **19**, 834–844, doi: 10.1190/1.1438721.

Sullivan, E. C., K. J. Marfurt, A. Lacazette, and M. Ammerman, 2006, Application of new seismic attributes to collapse chimneys in the Fort Worth Basin: Geophysics, **71**, no. 4, B111–B119, doi: 10.1190/1.2216189.

Sun, Q., J. Cartwright, S. Wu, and D. Chen, 2013, 3D seismic interpretation of dissolution pipes in the South China Sea: Genesis by subsurface, fluid induced collapse: Marine Geology, **337**, 171–181, doi: 10.1016/j.margeo.2013.03.002.

Sun, S. Z., Z. Liu, H. Wang, and H. Yang, 2011, Quantitative inversion of carbonate secondary pore structure using rock physics model: 81st Annual International Meeting, SEG, Expanded Abstracts, 2266–2271, doi: 10.1190/1.3627659.

Sun, S. Z., L. F. Liu, and T. Du, 2016, Karst carbonate reservoir identification using frequency dependent AVO inversion in Tarim Basin, China: 78th Conference and Exhibition, EAGE, Extended Abstracts.

Tinker, S. W., J. R. Ehrets, and M. D. Brondos, 1995, Multiple karst events related to stratigraphic cyclicity: San Andres Formation, Yates field, west Texas, *in* D. A. Budd, A. H. Saller, and P. M. Harris, eds., Unconformities and porosity in carbonate strata: AAPG Memoir 63, 213–238.

Tran, K.T., M. McVay, T. D. Nguyen, 2015, Detection of voids in karst terrain with fill waveform tomography: 14th sinkhole conference, NCKRI Symposium 5, 381–386

Trice, R., 2005, Challenges and Insights in Optimizing Oil production from Middle East Mega Karst Reservoirs: 14th SPE Middle East Conference, SPE, Conference Paper, SPE 93679, 1–26, doi: 10.2118/93679-MS.

Troschinetz, J., 1992a, An example of karsted Silurian reservoir: Buckwheat Field, Howard County, Texas, *in* M. P. Candelaria and C. L. Reed, eds., Paleokarst, karst related diagenesis and reservoir development: Examples from Ordovician-Devonian age strata of west Texas and the Mid-Continent: PBS-SEPM Publication 92-33, 131–133.

Troschinetz, J., 1992b, Paleokarst reservoir in Crittendon (Silurian) Field, Winkler County, Texas, *in* M. P. Candelaria and C. L. Reed, eds., Paleokarst, karst related diagenesis and reservoir development: Examples from Ordovician-Devonian age strata of west Texas and the Mid-Continent: PBS-SEPM Publication 92-33, 134–136.

Tschopp, R. H., 1967, Development of the Fahud Field: 7th World Petroleum Conference Proceedings, 243–250.

Tyrrell, W.W., and H. E. Christian, 1992, Exploration history of Liuhua 11-1 field, Pearl River Mouth basin, China: AAPG Bulletin, **76**, 1209–1223.

Twombley, B. N. and J. Scott, 1975, Application of geological studies in the development of the Bu Hasa Field, Abu Dhabi: 9th Arab Petroleum Congress*,* Paper*,* 133, B - 1: 1–27.

Vahrenkamp, V. C., F. David, P. Duijndam, M. Newall, and P. Crevello, 2004, Growth architecture, faulting, and karstification of a middle Miocene carbonate platform, Luconia Province, offshore Sarawak, Malaysia, in Seismic imaging of carbonate reservoirs and systems: AAPG Memoir 81, 329–350.

Vandenberghe, N., E. Poggiagliolmi, and E. Schwarz, 1983, Analysis of reflection seismic data for the detection of karstified limestones at depth: 3rd International Seminar, European Geothermal Update, 122–133.

Varenicheva, N. I., V. A. Shcherba, Y. K. Kan, 1973, Karst and fracture types of reservoirs in the Orenburg gas condensate fields: Petroleum geology: A digest of Russian literature on Petroleum Geology, **11**, 90–94.

Verma, S., O. Mutlu, T. Ha, W. Bailey, and K. J. Marfurt, 2015, Calibration of attribute anomalies through prestack seismic modeling: Interpretation, **3**, no. 4, SAC55–SAC70, doi: 10.1190/INT-2015-0072.1.

Verseput, T. S., 1989. Depositional setting of the Ellenburger Langley Field, Lea County, New Mexico, *in* B. K. Cunningham and D. W. Cromwell, eds., The Lower Paleozoic of West Texas and Southern New Mexico-Modern Exploration Concepts: PBS-SEPM Publication 89-31, 145–157.

Vest, E. L., 1970, Oil fields of the Pennsylvanian-Permian Horseshoe Atoll, west Texas, *in* M. T. Halbouty, ed., Geology of giant petroleum fields: AAPG Memoir 14, 185–203.

Videtich, P. E., R. K. McLimans, H. K. S. Watson, and R. M. Nagy, 1988, Depositional, diagenetic, thermal, and maturation histories of Cretaceous Mishrif Formation, Fateh Field, Dubai: AAPG Bulletin, **72**, 1143–1159.

Viniegra-O, F., and C. Castillo-Tejero, 1970, Golden Lane fields, Veracruz, Mexico, *in* M. T. Halbouty, ed., Geology of giant petroleum fields: AAPG Memoir 14, 309–325.

Waddell, R. T., H. Liu, and J. M. Forgotson, 1991, Karst breccias of the Wade, Bray, and Brown Zones of the upper Arbuckle Group in the Healdton Field, Carter County, Oklahoma, *in* K. S. Johnson, ed., Arbuckle Group Core Workshop and Field Trip: OGS Special Publication 91-3: 185–189.

Walters, R. F., 1946. Buried pre-Cambrian hills in northeastern Barton County, central Kansas: AAPG Bulletin, **30**, 660–710.

Walters, R. F., 1958. Differential entrapment of oil and gas in Arbuckle Dolomite of central Kansas: AAPG Bulletin, **42**, 2133–2173.

Walters, R. F., and A. S. Price, 1948, Kraft-Prusa Field, Barton County, Kansas, *in* J. V. Howell, ed., Structure of typical American oil fields: AAPG Symposium 3, 249–280.

Watson, H. J., 1982, Casablanca Field offshore Spain, a paleogeomorphic trap, *in* M. T. Halbouty, ed., The deliberate search for the subtle trap: AAPG Memoir 32, 237–250.

Wei, G., G. Chen, S. Du, L. Zhang, and W. Yang, 2008, Petroleum systems of the oldest gas field in China: Neoproterozoic gas pools in the Weiyuan gas field, Sichuan Basin: Marine and Petroleum Geology, **25**, 371–386, doi: 10.1016/j.marpetgeo.2008.01.009.

Whiting, L. L., and D. L. Stevenson, 1965, Sangamon Arch: ISGS Circular, 383, 1–20.

Wigley, P. L., J. D. Bouvier, and J. M. Dawans, 1988, Karst and mixing-zone porosity in the Amposta Marino Field, offshore Spain: AAPG Bulletin, **72**, 1031.

Wilson, J. L., 1980a, A review of carbonate reservoirs., *in* A. D. Miall, ed., Facts and principles of world petroleum occurrence*:* CSPG Memoir 6, 95–115.

Wilson, J. L., 1980b, Limestone and dolomite reservoirs, *in* G. D. Hobson, ed., Developments in Petroleum Geology, 2: Applied Science Publishers Ltd., 1–51.

Wilson, J. L., 1985, Petroleum reservoirs and karst: SEPM Annual Midyear Meeting Abstracts II*,* 97–98.

Wilson, J. L., Fritz, R. D. and Medlock, P. L., 1991, The Arbuckle Group - relationship of core and outcrop analyses to cyclic stratigraphy and correlation, *in* K. S. Johnson, ed., Arbuckle Group Core Workshop and Field Trip: OGS Special Publication 91- 3: 133–144.

Wilson, J. L. P. L. Medlock, R. D. Fritz, K. L. Canter, and R. G., Geesaman, 1992, A review of Cambro Ordovician breccias in North America, *in* M. P. Candelaria and C. L. Reed, eds., Paleokarst, karst related diagenesis and reservoir development: examples from Ordovician-Devonian age strata of west Texas and the Midcontinent: PBS-SEPM 92-33, 19–29.

Withrow, P. C., 1972, Star-Lacey Field, Blaine and Kingfisher Counties, Oklahoma, *in* R. E. King, ed., Stratigraphic oil and gas fields: AAPG Memoir 16, 520–531.

Wright, P., 2016, Hypogene paleokarst and burial corrosion, https://www.npd.no/globalassets/2-force/2019/documents/archive-2010-2018/advances-in-siliciclastic-and-carbonate-sedimentology/paul-wright---hypogene-palaeokarst-and-burial-corrosion.pdf , accessed 7 July 2020.

Wright, P., and P. M. Harris, 2013, Carbonate dissolution and porosity development in the burial (mesogenetic) Environment: AAPG Search and Discovery Article #50860.

Xu, C., B. Di, and J. Wei, 2016, A physical modeling study of seismic features of karst cave reservoirs in the Tarim Basin, China: Geophysics, **81**, no. 1, B31–41, doi: 10.1190/GEO2014-0548.1.

Xu, S., and M. A. Payne, 2009, Modeling elastic properties in carbonate rocks: Leading Edge, **28**, no.1, 66–74.

Yang, B. X., 1986, Diagenetic history and reservoir characteristics of a Middle Carboniferous dolomite reservoir, eastern Sichuan, China: Sedimentary Geology, **46**, 275–291.

Yang, H., F. Xue, W. Pan, L. Chen, and P. Yang, 2010, Seismic description of karst topography and caves of Ordovician carbonate reservoirs, Lungu area, Tarim basin, west China: 80th Annual International Meeting, SEG, Expanded Abstracts, doi: 10.1190/1.3513072.

Yang, P., S. Z. Sun, Y. Liu, H. Li, G. Dan, and H. Jia, 2012, Origin and architecture of fractured-cavernous carbonate reservoirs and their influences on seismic amplitudes: The Leading Edge, **32**, no. 1, 140–150, doi: 10.1190/1.3686911.

Yao, Y., L. Sa, and S. Wang, 2005, Research on the seismic wave field of karst cavern reservoirs near deep carbonate weathered crusts: Applied Geophysics, **2**, 94–102, doi: 10.1007/s11770-005-0040-6.

Yie, D. S., 1991, Diagenesis and reservoir characteristics of Cambrian through Early Ordovician dolomite in the northern Tarim basin, *in* R. X. Jia, ed., Petroleum research in the northern Tarim basin, China, part 1—stratigraphy and sedimentology: China University Geosciences Press, 263–273.

Yie, D. S., and S. H. Liu, 1991, Diagenesis and reservoir property of Sinian Qigebulake Formation dolomite in northeast Tarim basin, *in* R. X. Jia, ed., Petroleum research in the Northern Tarim basin, China, part 1—Stratigraphy and sedimentology: China University Geosciences Press, 247–255.

Zampetti, V., U. Sattler, and H. Braaksma, 2005, Well log and seismic character of Liuhua 11-1 field, south China sea; relationship between diagenesis and seismic reflections: Sedimentary Geology, **175**, 217–236.

Zampetti, V., X. Marquez, S. Mukund, S. Bach, and M. Emang, 2014, 3D Seismic characterization of UER Karst, Offshore Qatar: International Petroleum Technology Conference, IPTC 17638, 1–12, doi: 10.2523/IPTC-17638-MS.

Zeng, H., C. Kerans, and J. Lucia, 2006, 3-D seismic detection of collapsed Paleocave Systems in the Clear Fork/Glorieta Platform, Hobbs Field, New Mexico: 76th Annual International Meeting, SEG, Expanded Abstracts, 1023–1027, doi: 10.1190/1.2369687.

Zeng, H., Q. Wang, B. Loucks, X. Janson, Y. Xia, and L. Xu, 2010, Seismic geomorphologic, core, and outcrop expression of an Ordovician paleokarst system in north-central Tarim Basin, China, *in* L. J. Wood, T. T. Simo, and N. C. Rosen, eds., Seismic imaging of depositional and geomorphologic systems: 30th Annual GCSSEPM Foundation Bob F. Perkins Research Conference, CD-ROM, 73–87.

Zeng H., G. Wang, X. Janson, R. Loucks, and B. Yuan, 2011a, Characterizing seismic bright spots in deeply buried Ordovician Paleokarst strata, Central Taibei uplift, Tarim Basin, Western China: Geophysics, **76**, no. 4, B127–B137, doi: 10.1190/1.3581199.

Zeng, H., Loucks, R., Janson, X., Wang, G., Xia, Y., Yuan, B., Xu, L., 2011b, Three-dimensional seismic geomorphology and analysis of the Ordovician paleokarst drainage system in the central Tabei Uplift, northern Tarim Basin, western China: AAPG Bulletin, **95**, 2061–2083, doi: 10.1306/03111110136.

Zhan, X., X. Fang, R. Danseshvay, E. Liu and C. E. Harris, 2014, Full elastic finite-difference modeling and interpretation of karst system in a subsalt carbonate reservoir: Interpretation, **2**, no. 1, T49–T56, doi: 10.1190/INT-2013-0120.1.

Zhao, W., A. Shen, Z. Qiao, J. Zeng, and X. Wang, 2014, Carbonate karst reservoirs of the Tarim Basin, northwest China: Types, features, origins, and implications for hydrocarbon exploration: Interpretation, **2**, no. 3, SF65–SF90, doi: 10.1190/INT-2013-0177.1.

Zhu, D., Q. Meng, Z. Jin, Q. Liu, and W. Hu, 2015, Formation mechanism of deep Cambrian dolomite reservoirs in the Tarim Basin, northwestern China: Marine and Petroleum Geology, **59**, 232–244, doi: 10.1016/j.marpetgeo.2014.08.022.

Figures

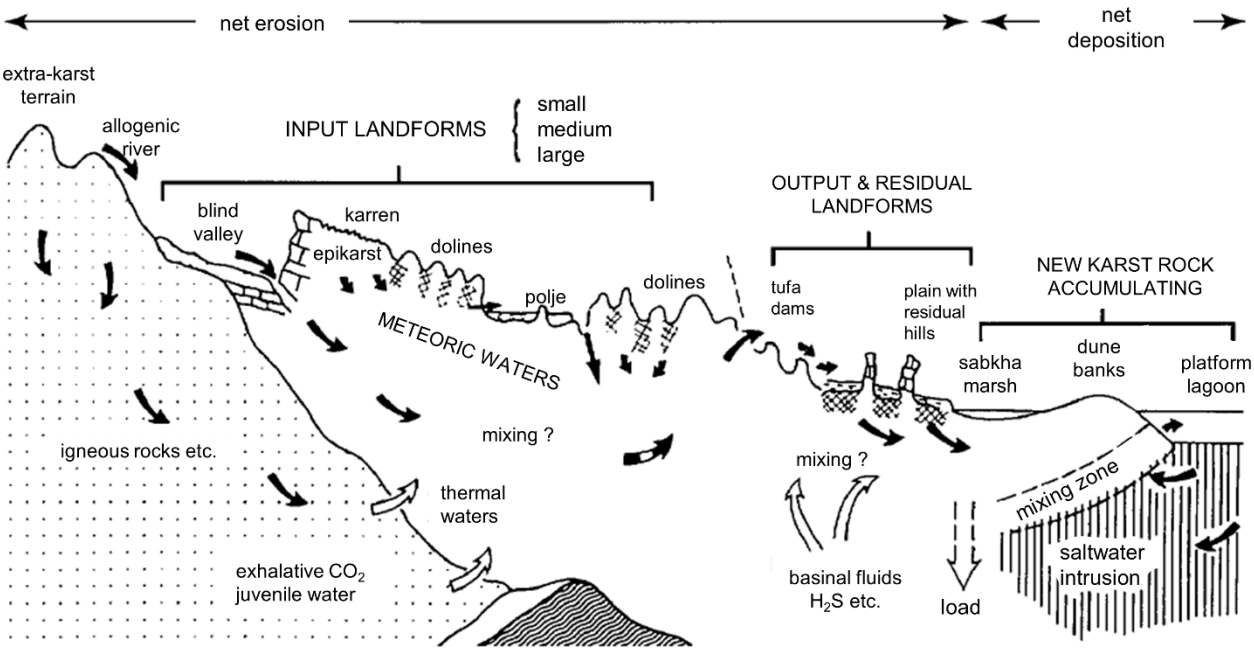

Figure 2.1. The comprehensive karst system: a composite diagram (modified after Ford and Williams, 2007).

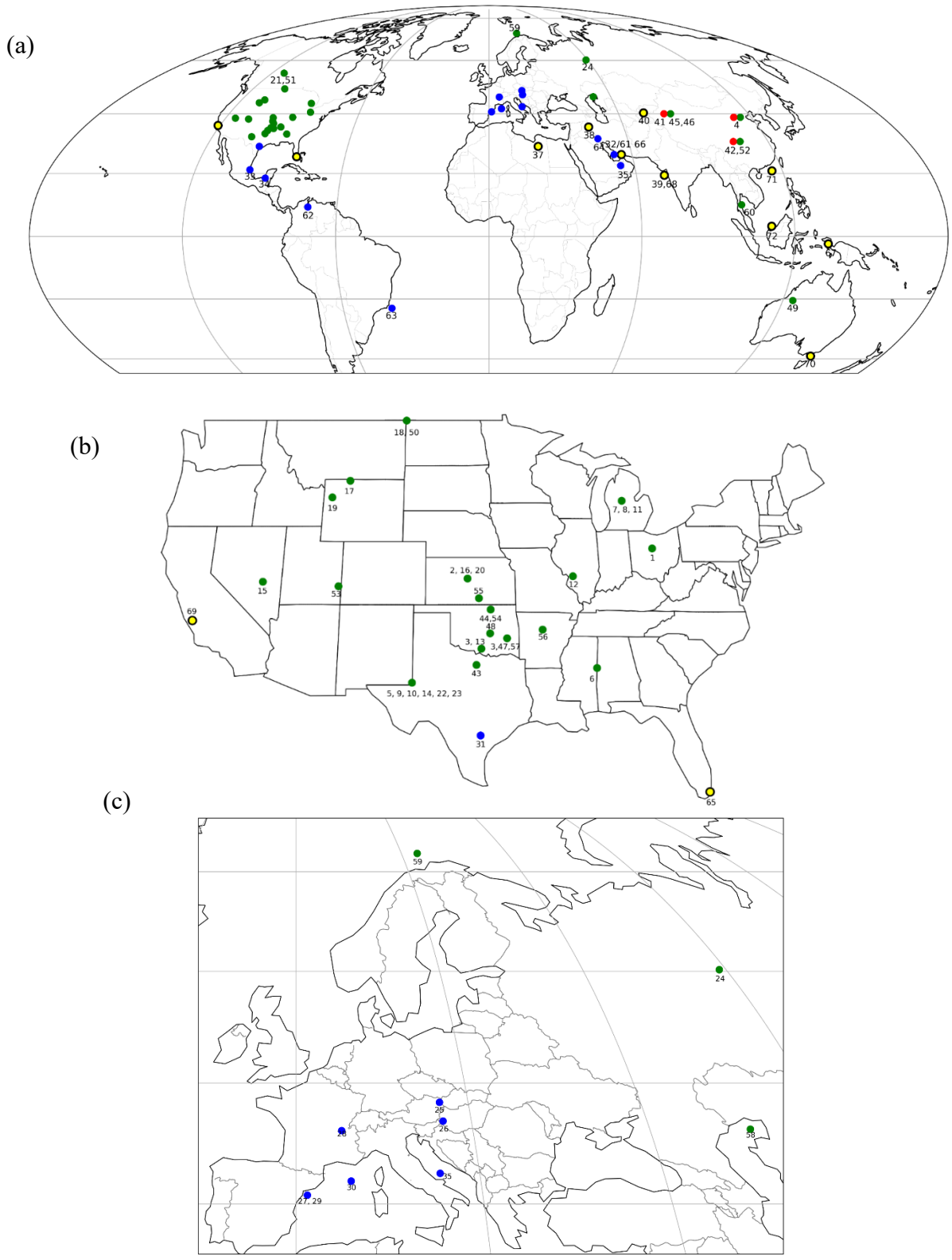

Figure 2.2. Karst worldwide locations. (a) Worldwide b) United States c) Europe. See Table 2.1. and 2.2. for location names.

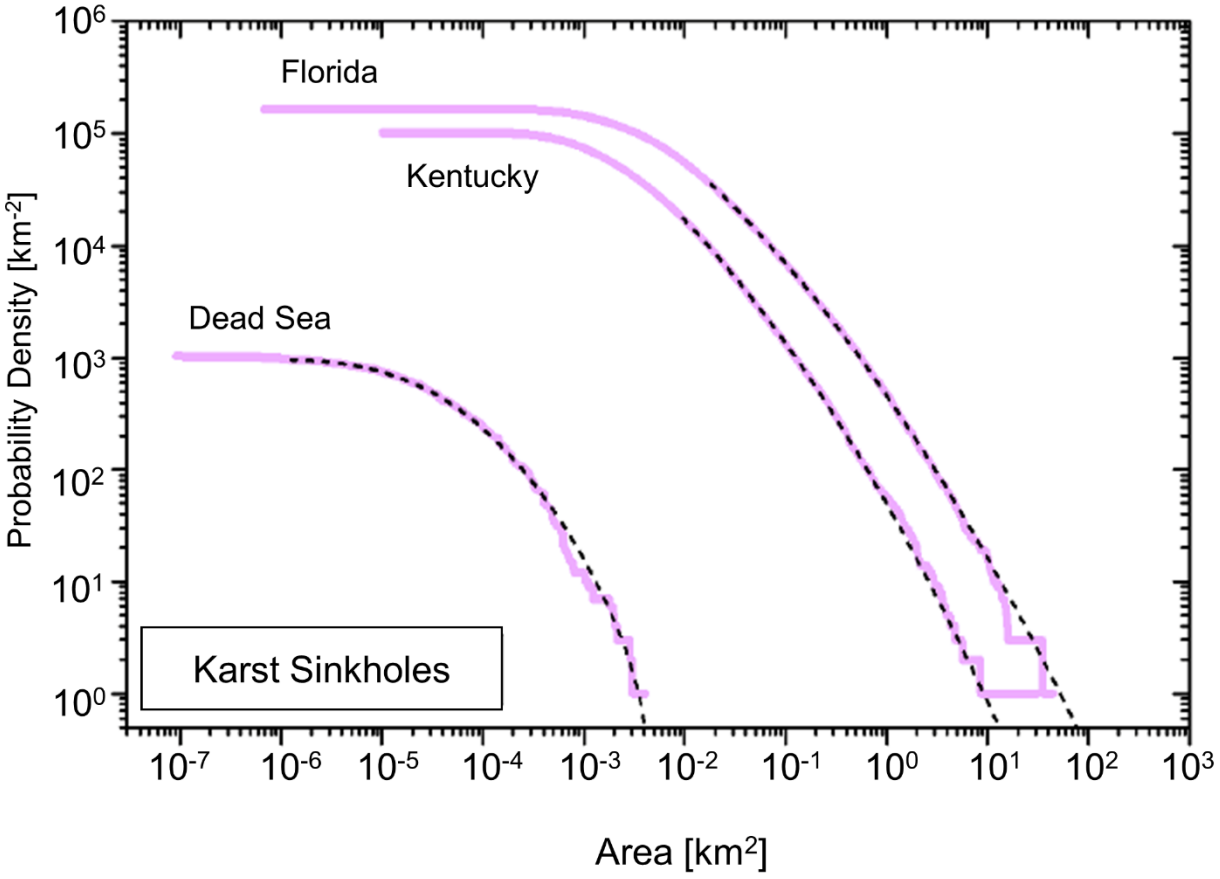

Figure 2.3. Sinkholes are better described by a truncated log-normal distribution. Solid lines indicate power law fits and dashed lines lognormal. (Modified from Corral and Gonzalez, 2019).

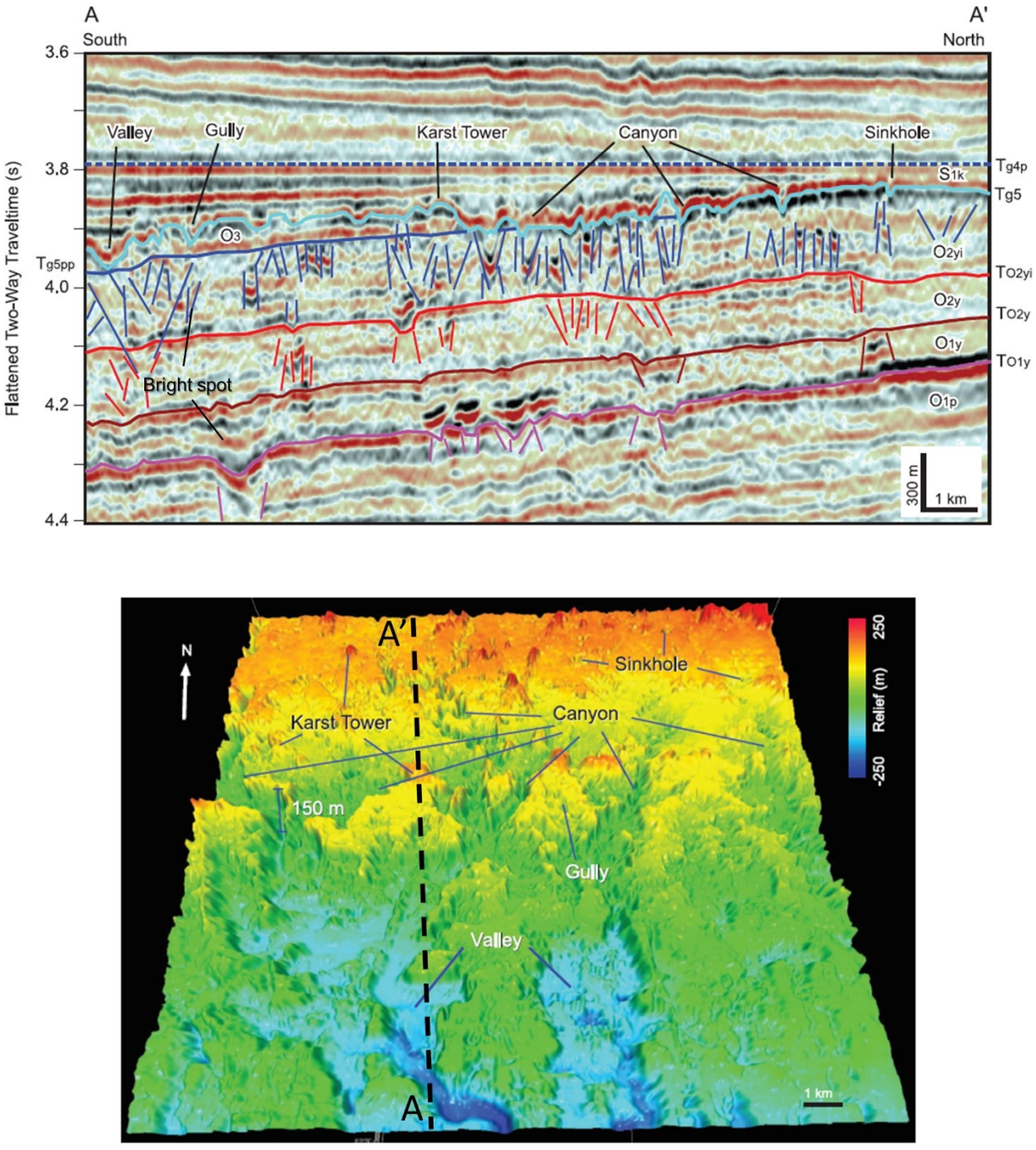

Figure 2.4. a) Seismic section AA' flattened on the Lower Silurian (Tg4p) reflection to show the original paleo-topography at the top of the Ordovician topography at the top of the Ordovician unconformity (Tg5) in the Tarim Basin, China b) 3D dimensional relief map (Modified from Zeng et al., 2011b).

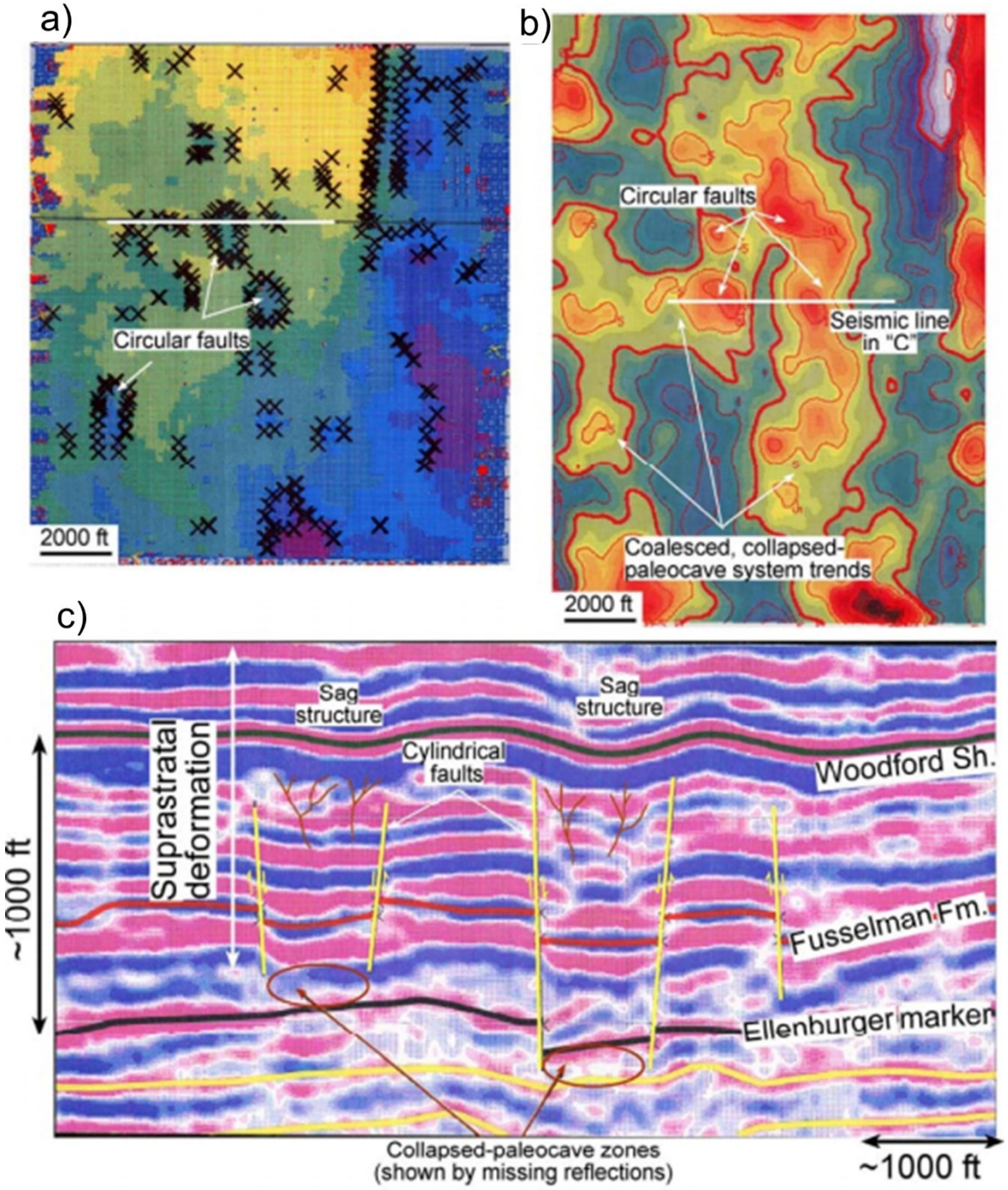

Figure 2.5. 3D seismic over an Ellenburger paleocave system in the Benedune field, Permian Basin, West Texas (a) Fusselman Formation structure map showing cylindrical faults produced by burial collapse of the Ellenburger cave system. (b) Second-order derivative map displaying sag zones produced by collapse in the Ellenburger interval. (C) Seismic line showing missing sections (collapse in Ellengburger section), cylindrical faults and sag structures. Suprastratal deformation is over a thousand feet thick in this section. Modified from Loucks (1999). After Loucks (2003)". No. 5, 10 location in Figure 2.1., Table 2.1.for location

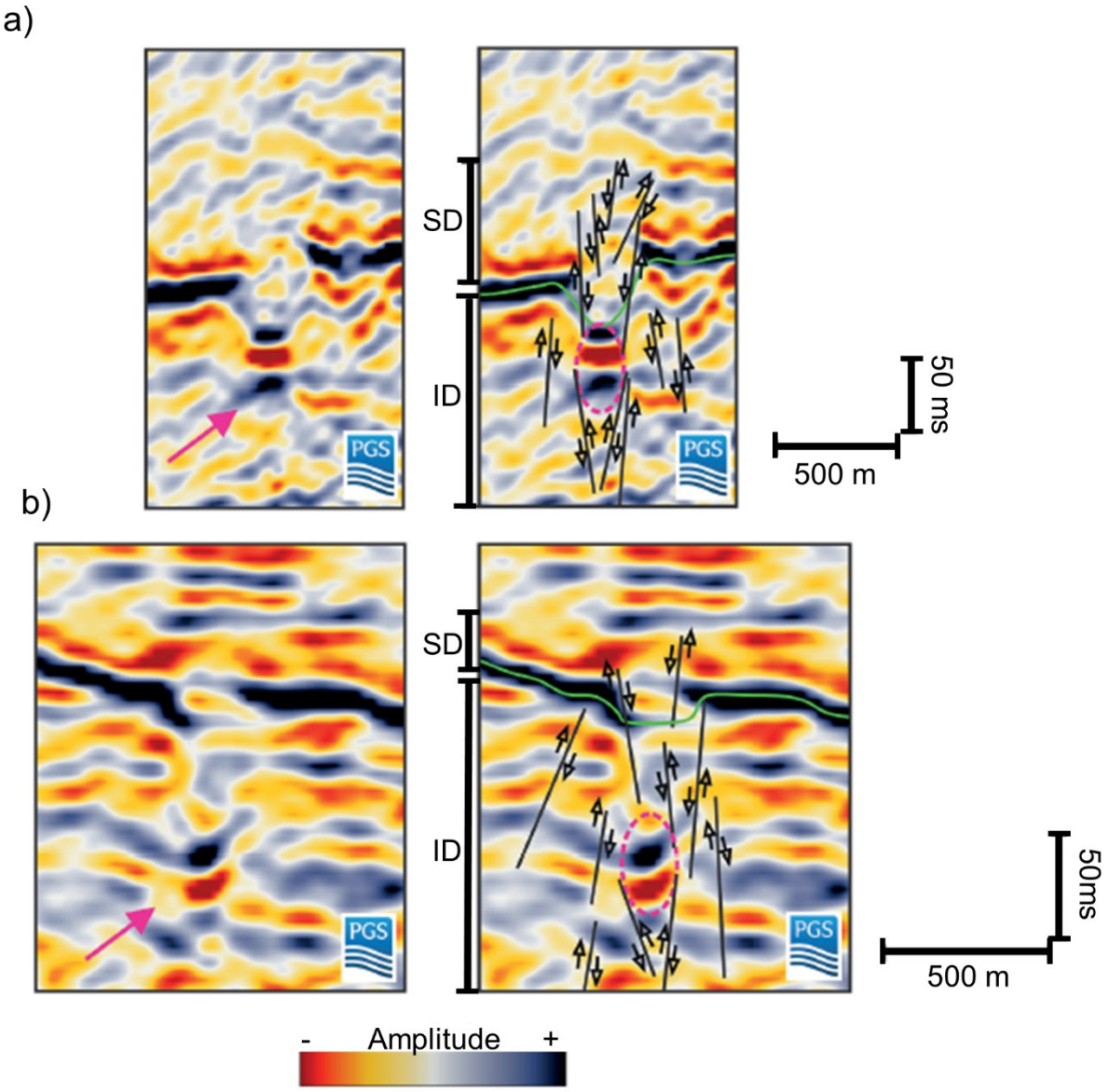

Figure 2.6. Seismic interpretation of two sinkholes (a and b), possibly associated with paleocave collapse in the Campos Basin, Brazil. Uninterpreted seismic sections (left). Structurally interpreted seismic section showing zones of suprastratal (SD) and intrastratal (ID) deformation (right). The green line corresponds to the top of the Macae Group, dashed circles indicate show bright spots associated with paleocave collapse (Modified from Basso et al. (2018). Location no is 63 on Figure 2.1. See Table 2.3 for sinkhole paleokarst dimensions.

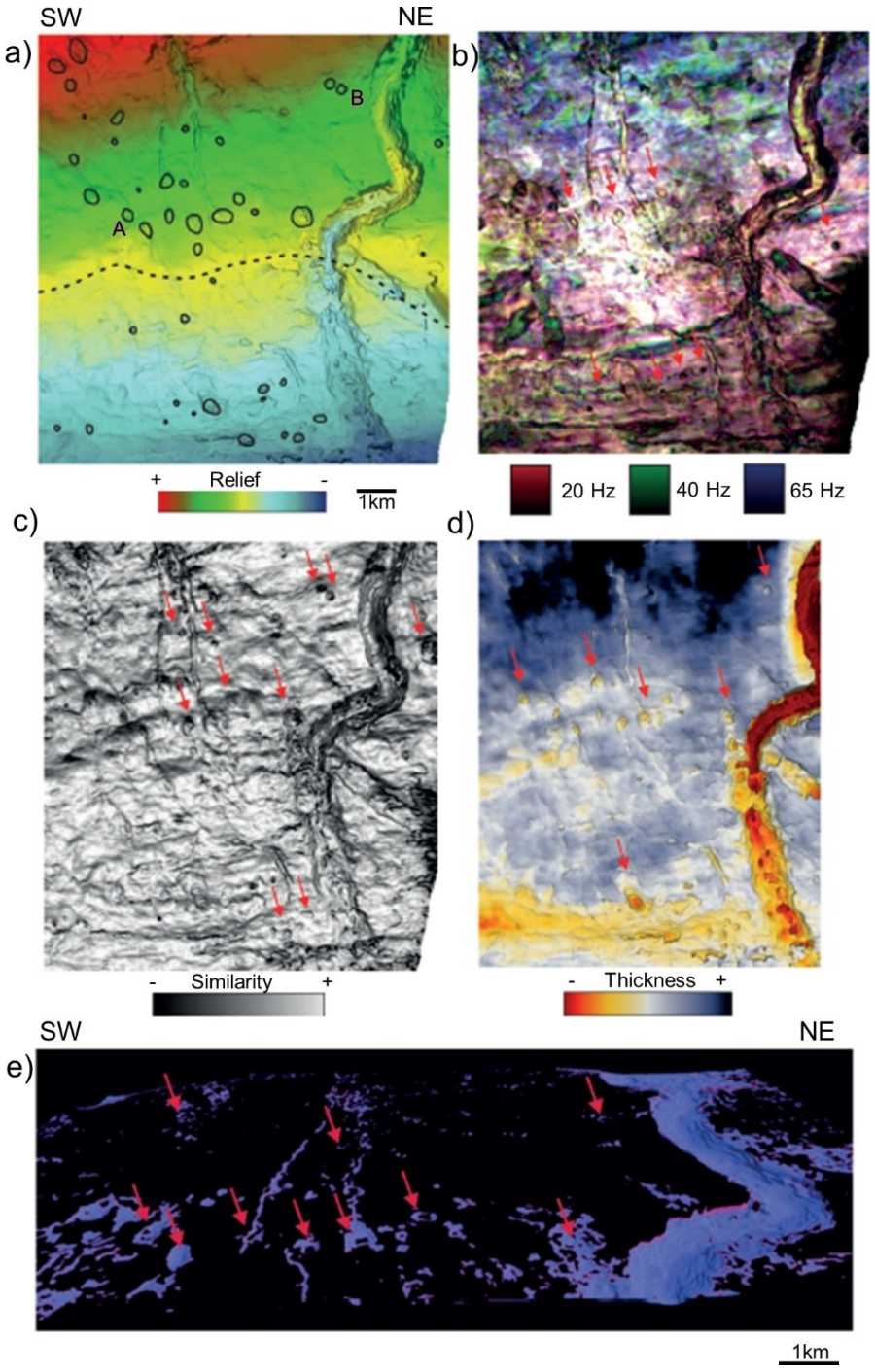

Figure 2.7. (a) Relief map of the northeast region of the study area; black circles (a) indicate sinkhole circular depressions, A and B on map are sinkholes shown in Figure 2.1.6, the dotted line is the boundary between the lowlands and highlands domains (b) Red, Green, Blue stack of the 20, 40, and 65 Hz spectral components. (c) Similarity attribute map of the paleokarst horizon at the top of the Cenozoic Macae Group. (d) Isopach map showing thickness variations of the Cenozoic Macae Group. (e) Multi-attribute classification by means of a Self-Organizing Map (SOM). The red arrows indicate examples of closed, circular depressions (Modified from Basso et al., 2018).

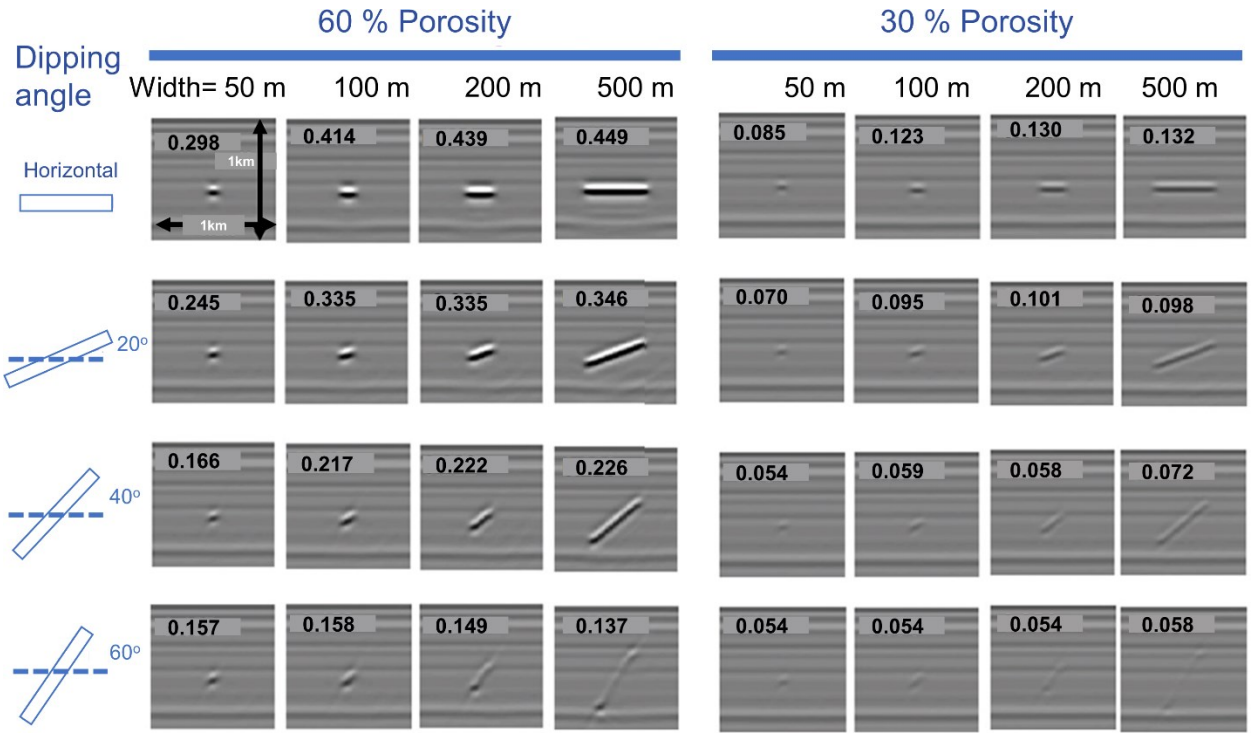

Figure 2.8. Comparison of the pre-stack time migration results for karsts with different dip angles and porosities. The number on each image is the corresponding karst reflectivity (Modified from Zhan et al., 2014).

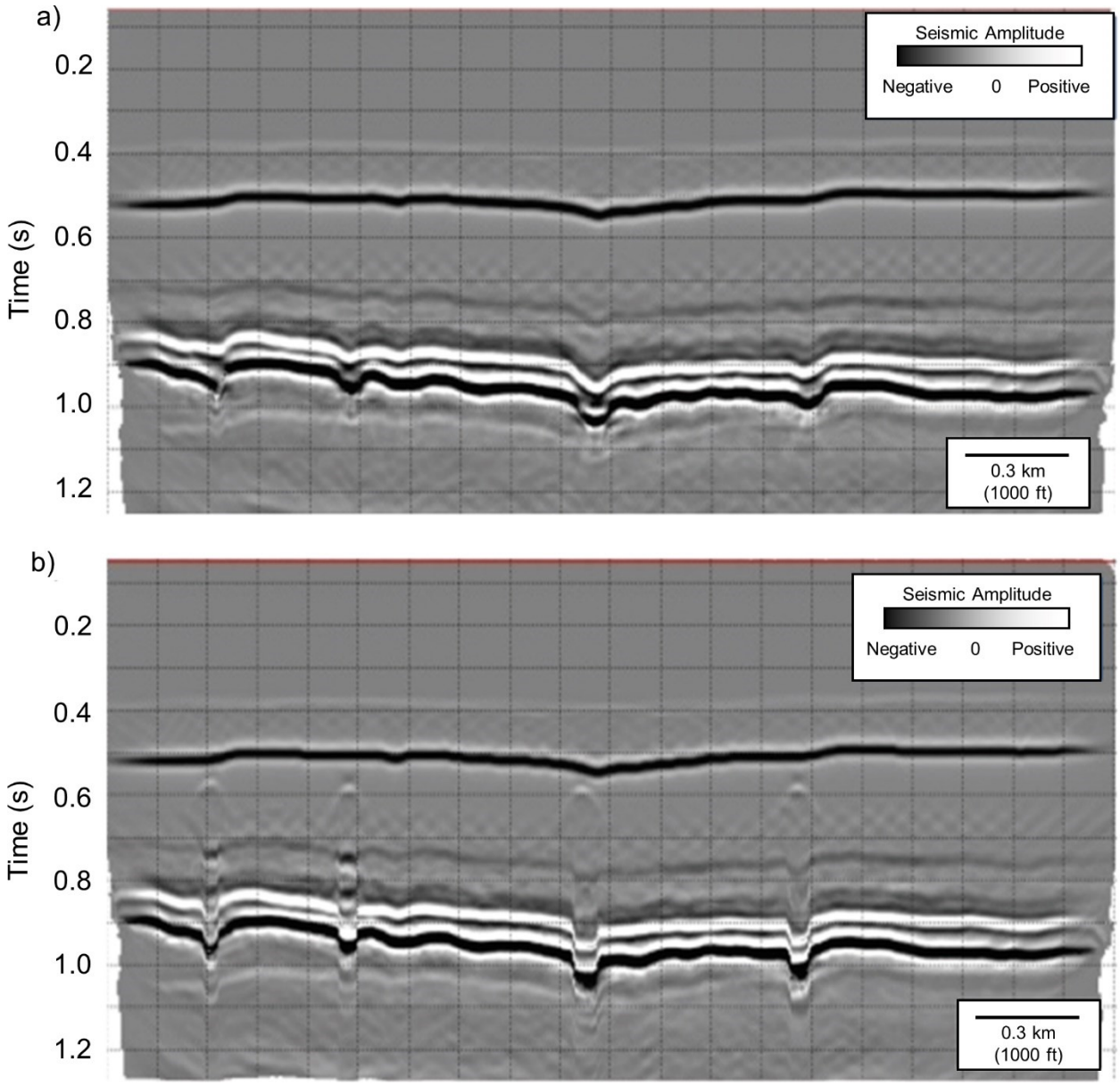

Figure 2.9. Seismic section (a) Karst collapse model (b) Gas chimney model (Modified fromVerma et al., 2015).

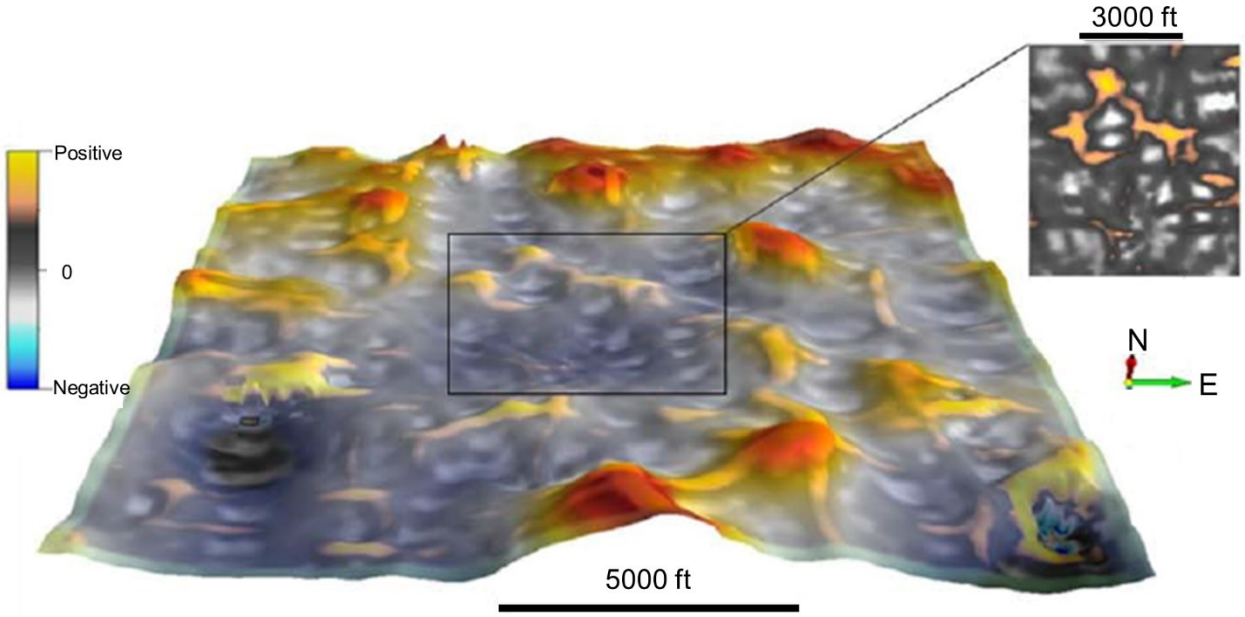

Figure 2.10. Most positive curvature map of the Boone Limestone, Arkoma Basin, Arkansas, showing cockpit karst (Modified after Moser, 2016)

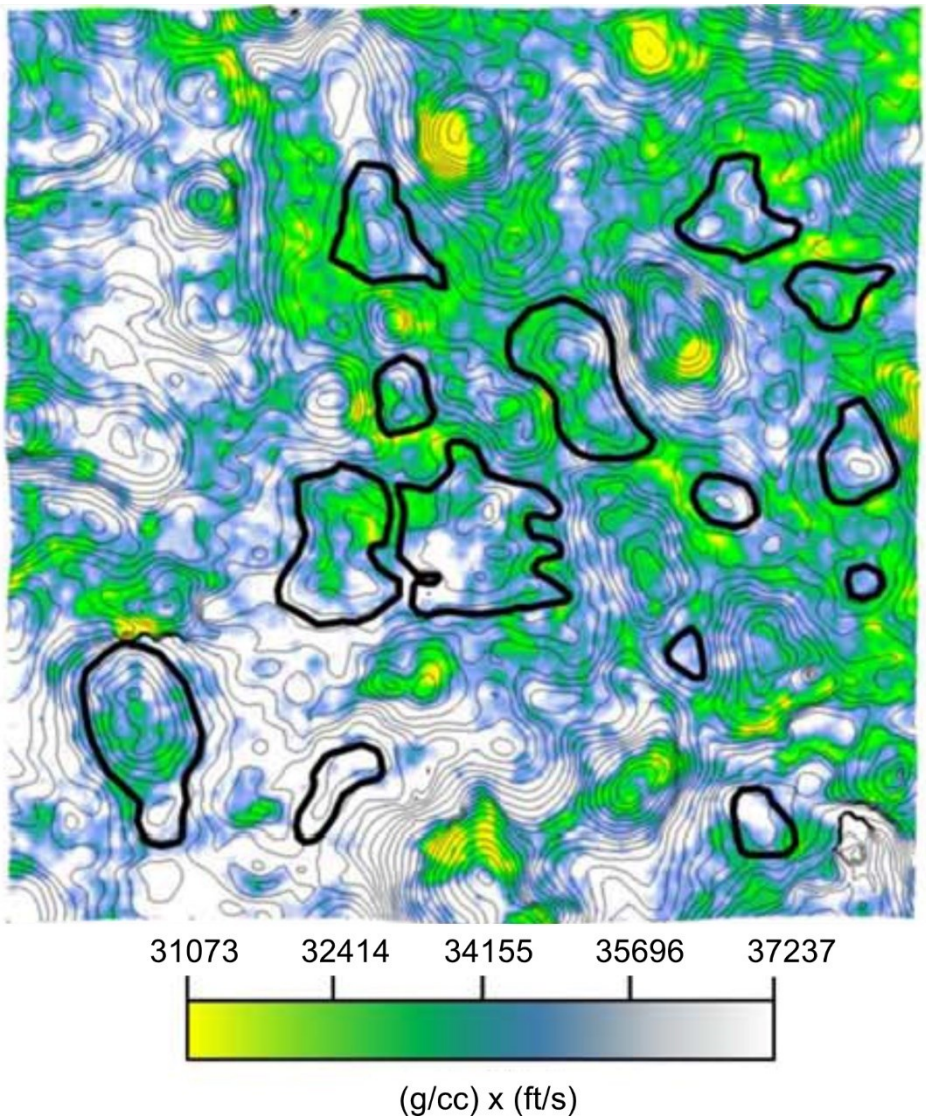

Figure 2.11. Boone Limestone acoustic impedance map showing sinkholes outlined in black in the Arkoma Basin, Arkansas (Modified after Moser, 2016) See S/N 46, Table 2.3

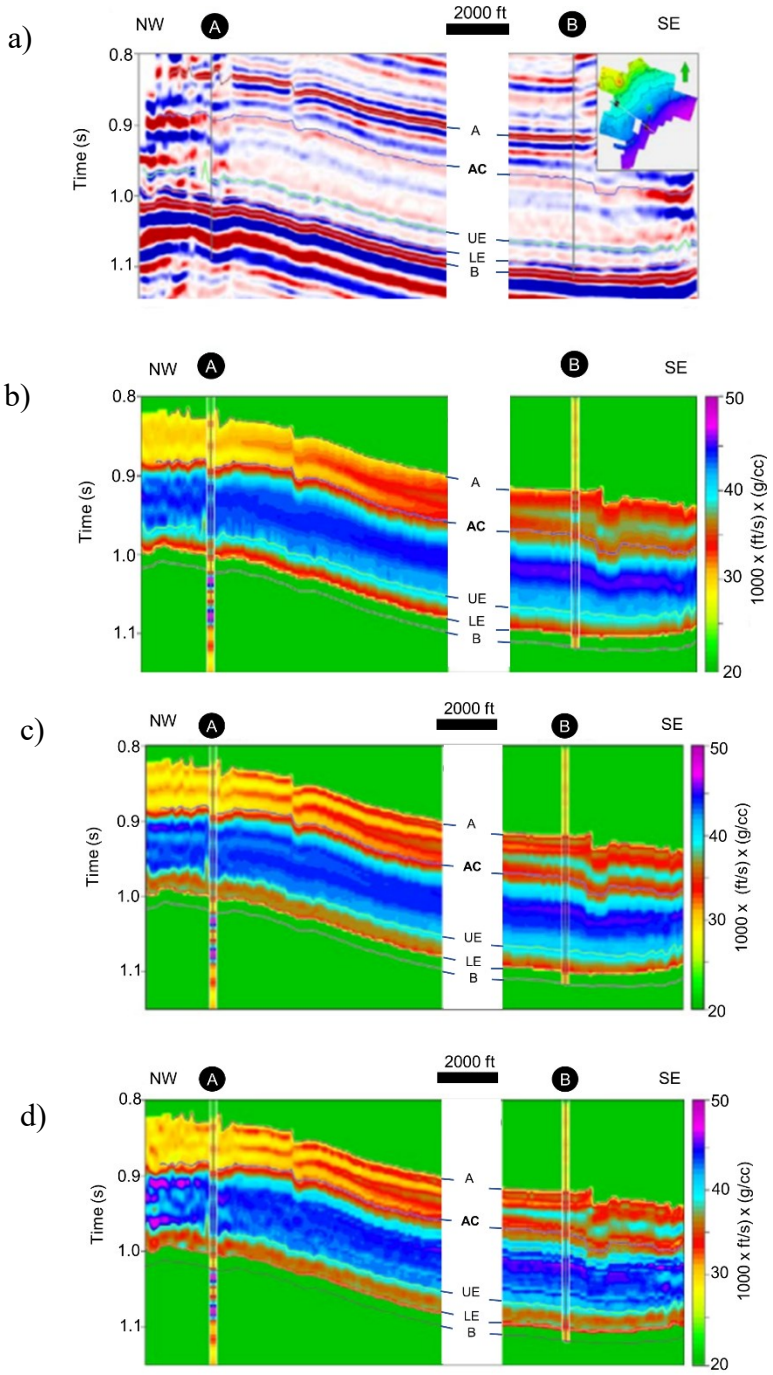

Figure 2.12. Visual comparison between (a) amplitude volume (b) Colored, (c) Band limited and (d) Model-based inversion. A= Anacacho Limestone, AC = Austin Chalk, UE = Upper Eagleford Shale, LE = Lower Eagleford Shale, B = Buda Limestone. Circles A and B are Holdsworth Nelson and Holdsworth Trust wells (Modified after Kilcoyne, 2018)

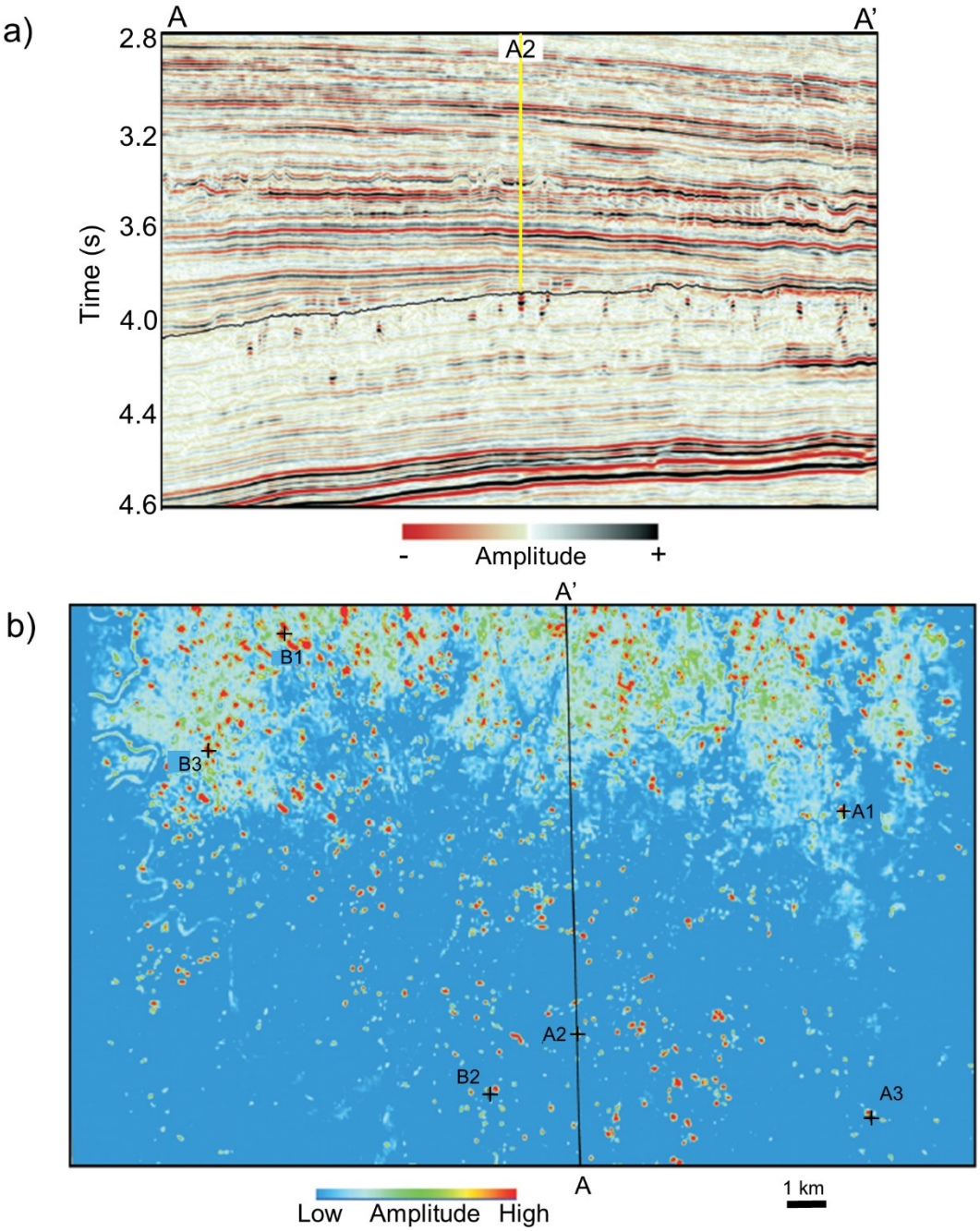

Figure 2.13. a) Line AA' seismic section through well A2. (b) Root mean square amplitude data in the layer of interest. Several bright spots are known seismic responses of carbonates caves by drilling. Wells A1-A3 are three prolific oil wells, B1-B3 are brine wells (Modified after Li et al., 2016).

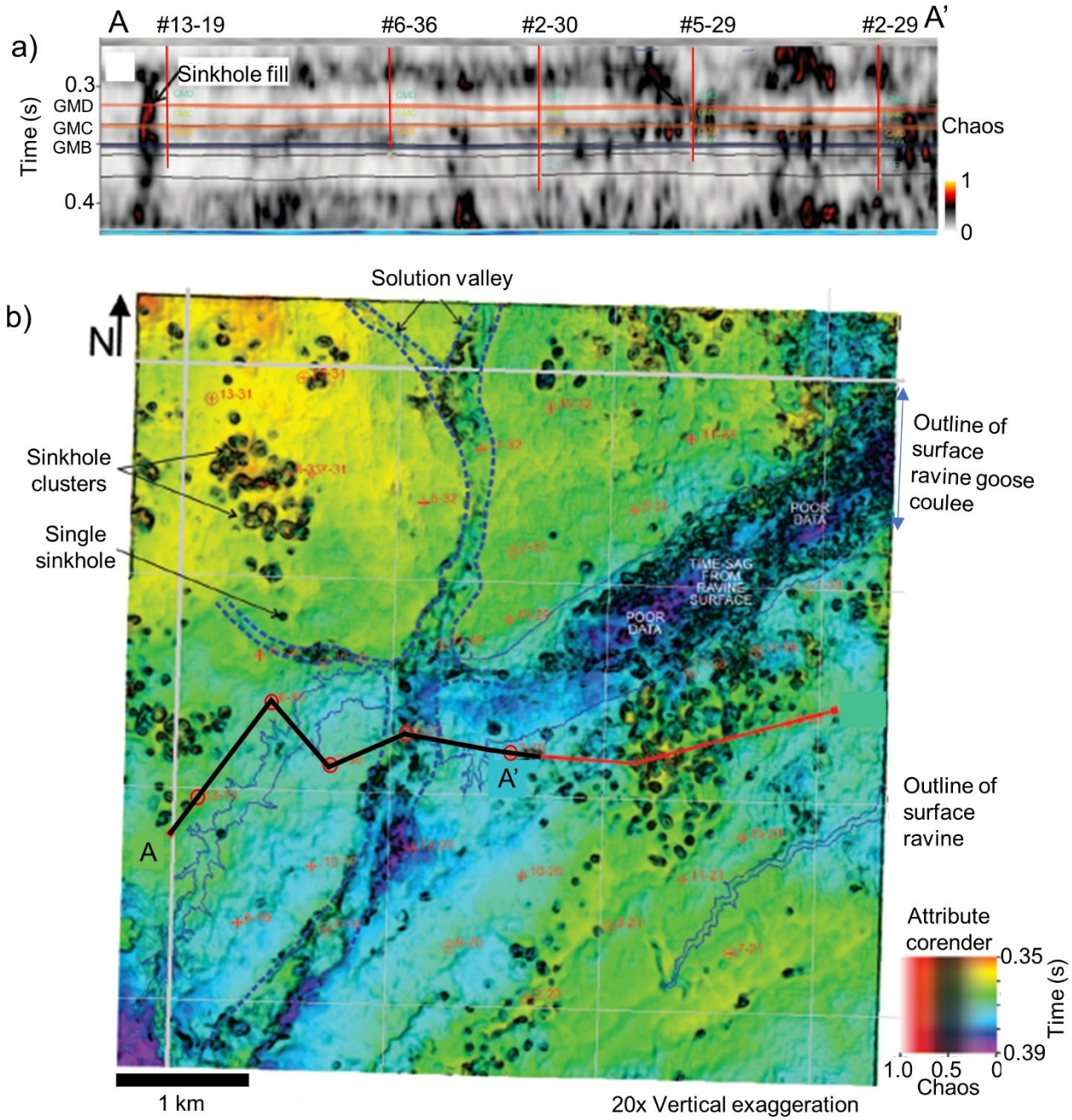

Figure 2.14. (a) Chaos attribute section AA' showing sinkhole fill or paleocave collapse, GMB, GMC, GMD are reservoirs in the Devonian Grosmont Formation Canada. Vertical red lines are wells (b) Sub-Cretaceous unconformity time structure map corendered with chaos attribute. Collapsed paleocave or sinkhole fills appear singular or in clusters. Red circles are well locations (Modified after Russel-Houston and Gray, 2014).

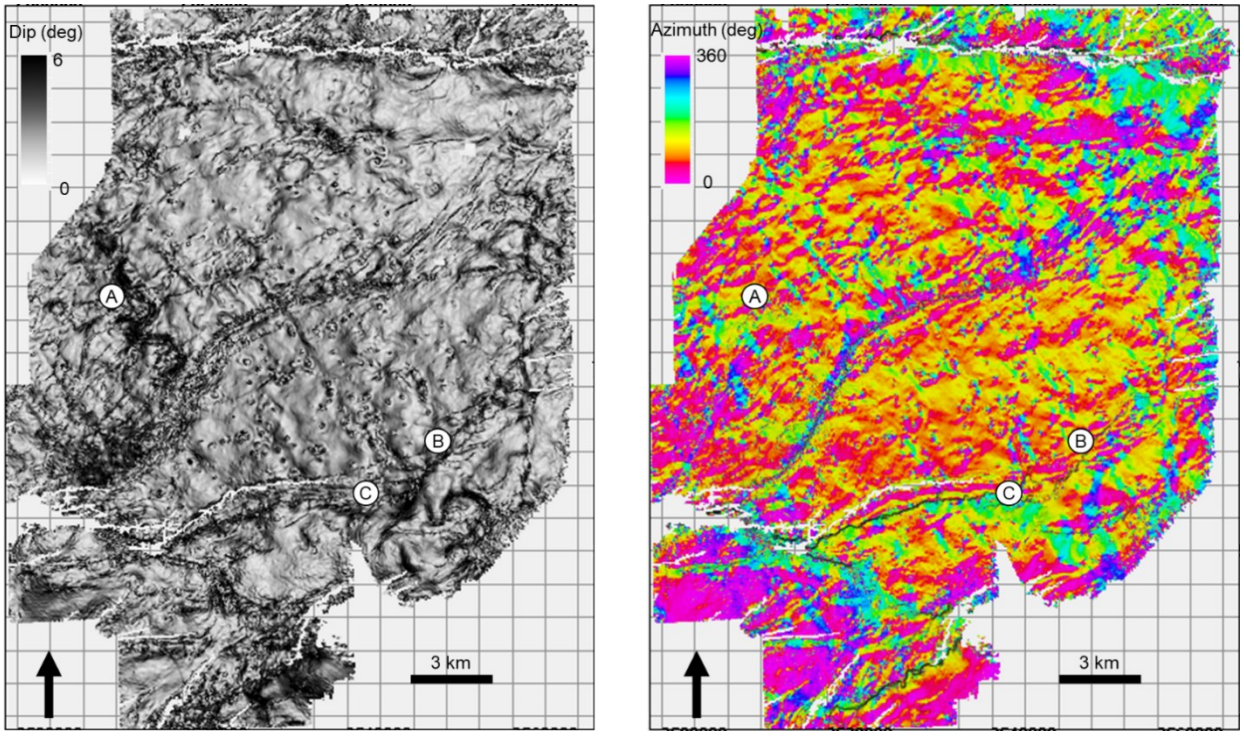

Figure 2.15. Viola Limestone in the Arkoma Basin a) Dip magnitude, b) Dip azimuth in the Circles A, B and C are well locations (Generated by author). See No. 47 in Figure 2.2, and Table 2.3.

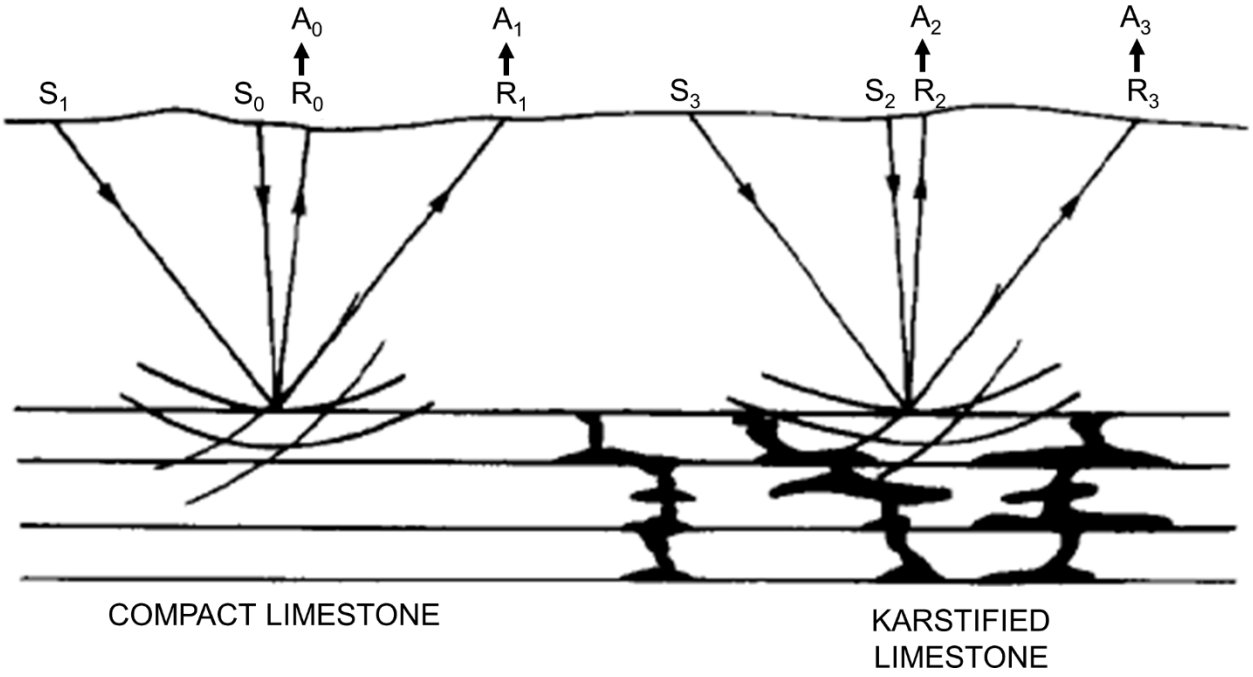

Figure 2.16. Amplitude analysis as function of offset for compact and karst limestone. A0, A1, A2, A3 = magnitudes of reflection for S_0-R_0 (near offset), S_1-R_1 (far offset), S_2-R_2 (near offset), S_3-R_3 (far offset), respectively (modified from Fontaine et al., 1987).

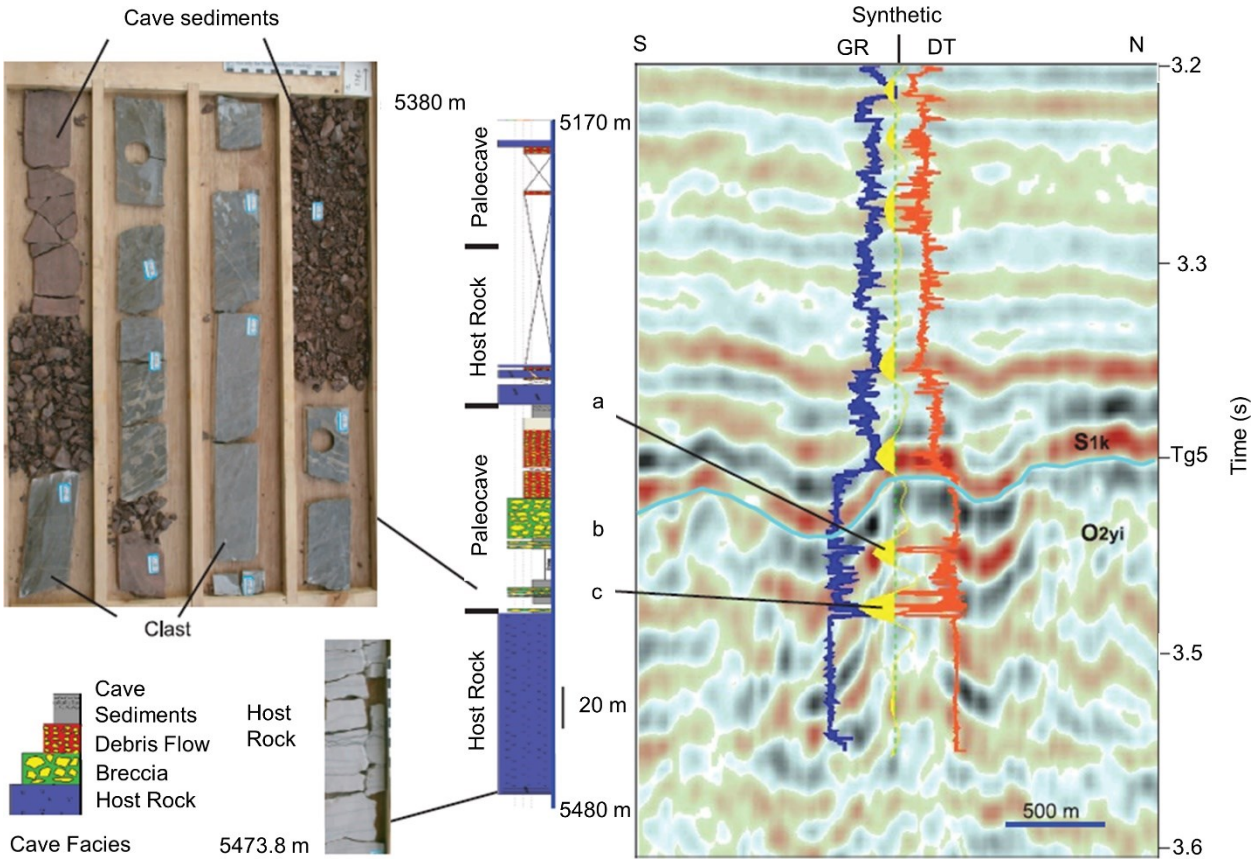

Figure 2.17. Core description of collapsed-paleocave section in the Middle Ordovician and correlation to wireline logs and well-site seismic section. Labels a, b, and c = zones of cave-sediment fill. The scale in the core box is in centimeters (modified from Zeng et al., 2011b)

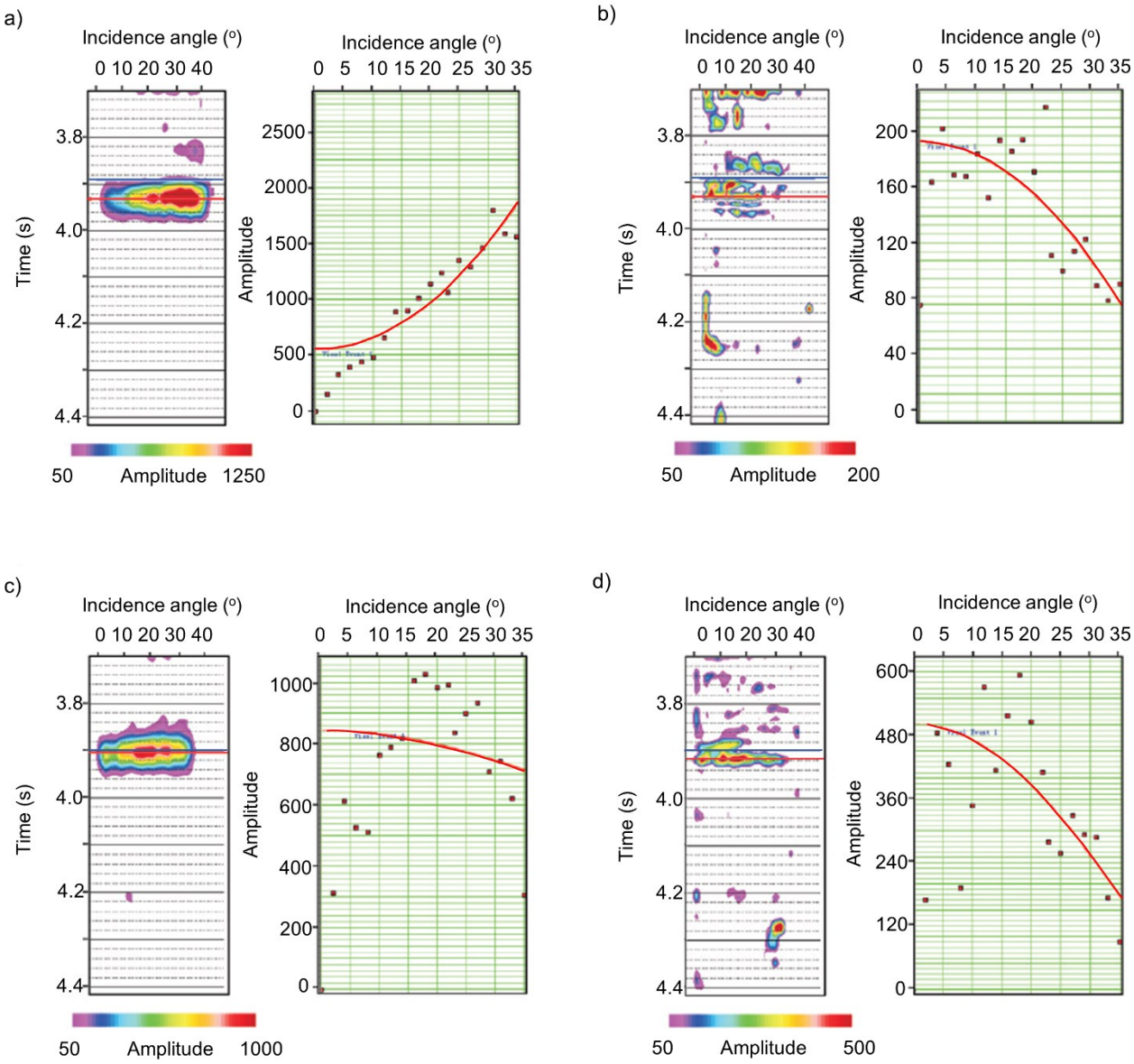

Figure 2.18. Iso-frequency spectral component of spectrally decomposed gathers (left panels). Red lines in the left panels mark the time corresponding to the peak spectral amplitude and the blue lines represent the top of the target layer. The right panels show variation in the peak spectral amplitude with incidence angles (the red dots). Oil well A1 (a) 10 Hz component (b) 50 Hz component. Brine well (c) 10 Hz component (d) 50 Hz component (modified after Li et al., 2016)

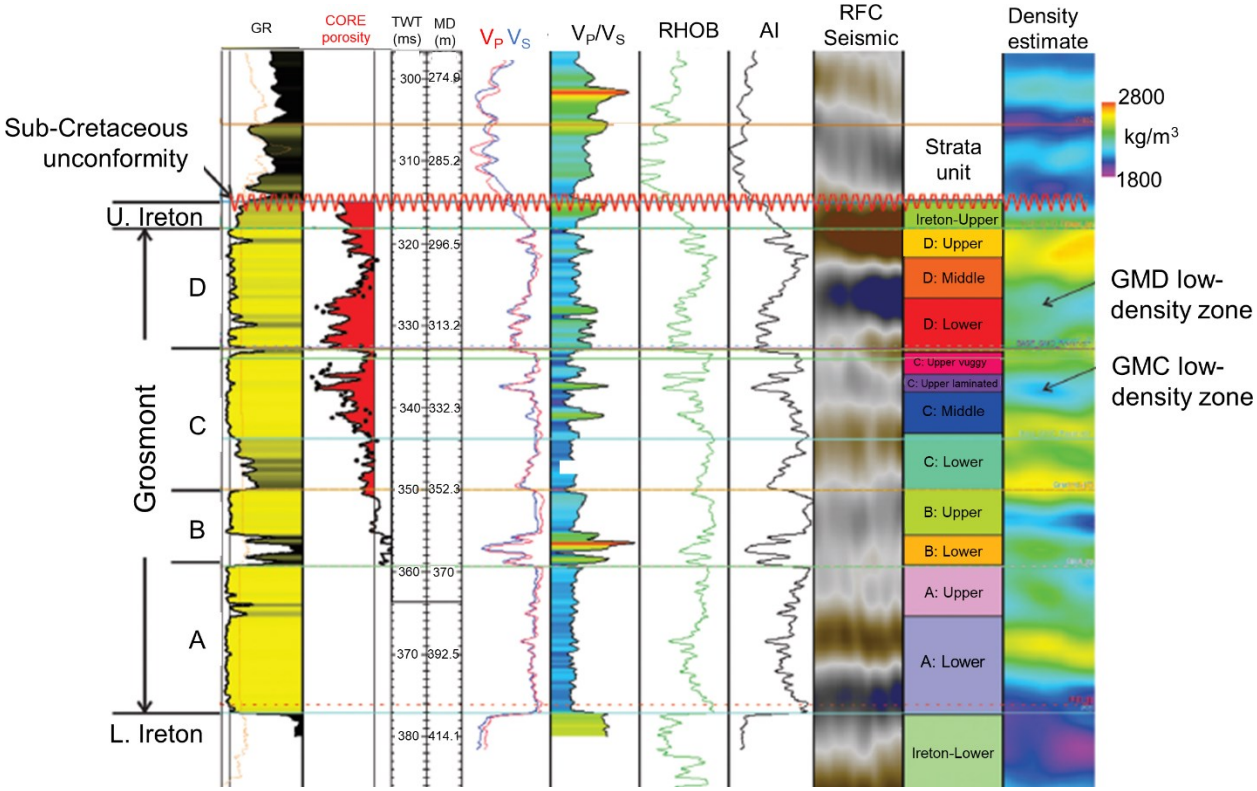

Figure 2.19. GR= Gamma ray, TWT = Two-way time, MD = Measured depth, V_P = Primary velocity, V_S = Secondary velocity, RHOB = Bulk density, AI= Acoustic impedance, RFC= Reflection Coefficient seismic. The two porous reservoir zones of GMD and GMC have a much lower density and stand out in the log and core analysis measures of porosity. The elastic inversion depends on a reasonably linear ln (V_P), ln (V_S) relationship, which can be seen with the V_P/V_S curve (Modified from Russel-Houston and Gray, 2014).

Tables

Table 2.1. Examples of paleokarst reservoirs in karsted carbonate rocks (Modified after Mazzullo and Chilingarian (1996)). No. = location numbers in Figure 2.1.

No.	Field/trend	Location	Reservoir age (unit)	Reservoir lithology	References
1	Various fields	Waverly Arch (Ohio)	U. Cambrian	Dolomite	Dolly and Busch (1972)
2	Kraft-Prusa Trend (Kansas)	Central Kansas Uplift (Arbuckle Group)	Cambrian-L. Ordovician	Dolomite	Walters (1946, 1958); Walters and Price (1948); Newell et al. (1987)
3	Cottonwood Creek, Healdton, Oklahoma, Wilburton fields (and others)	Anadarko and Arkoma Basins (Oklahoma)	Cambrian-L. Ordovician, (Arbuckle Group)	Dolomite	Gatewood (1970); Latham (1970); Wilson (1980a,b; 1985); Shirley (1988); Hook (1990); Bliefnick and Wilburton Belfield (1991); Carpenter and Evans (1991); fields (and others); Lynch and AI-Shaieb (1991); Waddell et al. (1991); Wilson et al. (1991, 1992); Blietfnick (1992)
4	Various fields (e.g. Renqiu)	North China-Bohay Bay Basins (China)	Cambrian-M. Ordovician Precambrian (various units)	Dolomite	Guangming and Quanheng (1982); Li et al. (1982); Qi and Xie-Pei (1984); Quanheng (1984)

Table 2.1. (Contd.)

No.	Field/trend	Location	Reservoir age (unit)	Reservoir lithology	References
5	Various fields	Permian Basin (Texas)	L. Ordovician (Ellenburger Group)	Dolomite	Mear and Dufunena (1984); Loucks and Anderson (1985); Mazzullo and Reid (1986); ljirigho and Schreiber (1988); Kerans (1988, 1989, 1991); Amthor and Friedman (1989); S. J. Mazzullo (1989a, b; 1990); Mear (1989a); Verseput (1989); Holtz and Kerans (1992); Kupecz (1992); Loucks and Handford (1992)
6	Various fields (e.g., New Hope, Fairview, Maben)	Appalachian Region, Black Warrior Basin (Alabama, Mississippi, Tennessee)	L-M. Ordovician (Knox Group)	Dolomite, limestone	Fritz (1991); Henderson and Knox (1991); Raymond and Osborne (1991)
7	Various fields	Michigan Basin (Michigan)	L.-M. Ordovician (Prairie du Chien Group)	Dolomite	Nadon and Smith (1992)
8	Lima Indiana and Albion-Scipio-Pulaski trends; Northville, Stoney Point, Trenton fields	Cincinnati and Findley Arches (Ohio, Indiana)	U. Ordovician (Trenton Fm., Black River Fm./Group)	Dolomite	Wilson (1980 a,b; 1985); DaHaas and Jones (1988); Catacosinos et al. (1990)

Table 2.1. (Contd.)

No.	Field/trend	Location	Reservoir age (unit)	Reservoir lithology	References
9	Dollarhide Field	Central Basin Platform (Permian Basin, Texas)	L. Ordovician - Devonian (Ellenburger Group, Fusselman Fm., Thirtyone Fm.)	Dolomite	Stormont (1949)
10	Various fields	Midland Basin and Central Basin Platform (Permian Basin, Texas and New Mexico)	L.-M. Silurian (Fusselman and Wristen Fms.)	Dolomite; some limestone and locally tripolitic chert	Mear and Dufurrena (1984); Garfield and Longman (1989) Loucks and Anderson (1985); Geesaman and Scott (1989); L. J. Mazzullo (1989;1990 a,b); S. J. Mazzullo (1989b); Mear (1989b); Canter et al. (1992); Entzimnger and Loucks (1992);Mazzullo and Mazzullo (1992); Troschinetz (1992 a,b)
11	No. and So, Michigan Basin Pinnacle Reef Trend (e.g. Belle River Hills, Rapid River fields)	Michigan Basin (Michigan)	M. Silurian (Niagara Group)	Dolomite	Mesolella et al. (1974); Gill (1985)
12	Various fields (e.g., Marine Pool, Colmer-Plymouth, Edinburg West)	Illinois Basin and Sangamon Arch (Illinois)	Silurian (Niagaran, some associated Bevonian)	Dolomite, limestone	Lowenstam (1948); Whiting and Stevenson (1965); Kruger (1992)

Table 2.1. (Contd.)

No.	Field/Trend	Location	Reservoir age (unit)	Reservoir Lithology	References
13	Star, Lacey, West Campbell, NE Alden fields	Anadarko Basin (Oklahoma)	Silurian - Devonian (Hunton Group)	Dolomite	Harvey (1972); Withrow (1972); Carpenter and Evans (1991)
14	Various fields	Permian Basin (Texas, New Mexico)	L.-U. Devonian (Thirtyone Fm.	Dolomite, local limestone and tripolitic chert	Hovorka and Ruppel (1990); Saller et al. (1991); Canter et al. (1992)
15	Grant Canyon Field	Basin and Range (USA)	Devonian (Simonson and Guilmette Fms.	Dolomite	Read and Zogg (1988)
16	Bindley Field	Central Kansas Uplift (Kansas)	L. Mississippian (Warsaw Fm.)	Dolomite	Ebanks et al. (1977)
17	Elk Basin Field (and others)	Big Horn Basin (Wyoming)	U. Mississippian (Madison Fm.)	Dolomite, some limestone	McCaleb and Wayhan (1969); McCaleb (1988)
18	Alida, Daly, Newburg, Nottingham, Parkman, South Westhope, Virden fields (and others)	Williston Basin (Canada and USA)	U. Mississippian (Mission Canyon and Madison Groups)	Limestone, dolomite	Edie (1958); Martin (1964, 1966); llling et al. (1967); Marafi (1972); Wilson (1985); Kent et al. (1988).
19	Carter Creek and Whitney Canyon fields	Wyoming Overthrust Belt	U. Mississippian (Madison Group)	Dolomite	Harris et al. (1988); Sieverding and Harris (1991)

Table 2.1. (Contd.)

No.	Field/Trend	Location	Reservoir age (unit)	Reservoir Lithology	References
20	Various fields	Central Kansas Uplift (Kansas)	Mississippian (Miss. Lime and "Chat"	Limestone, chert residuum	Wilson (1980 a,b)
21	Crossfield, Harmatton East, Harmattan Elkton, Sundre, Westward Ho fields	Alberta Basin (Canada)	Mississippian (Elkton Fm.)	Limestone	Martin (1964, 1966)
22	Various fields (including those on Horseshoe Atoll)	Midland Basin (Permian Basin, Texas)	M.-U. Pennsylvanian (Strawn, Canyon, Cisco Fms	Limestone, some dolomite	Vest (1970); Reid and Mazzullo (1988); Reid et al. (1990, 1991); Reid and Reid (1991)
23	Yates and Taylor Link West fields (and others)	Central Basin Platform (Permian Basin, Texas)	U. Permian (San Andres Fm.)	Dolomite	Craig et al. (1986); Kerans and Parsley (1986); Craig (1988)
24	Various fields (including Ishimbay	Ural Foredeep (U.S.S.R)	Permian (various units)	Limestone	Maslov (1945); Makismovich and Bykov (1978)
25	Malzen, Schonkirche n, Reyersdorf fields	Vienna Basin (Austria)	U. Triassic	Dolomite	Ladwein (1988)
26	Nagylengyel Field	Hungary	Triassic, some Cretaceous	Limestone, dolomite	Balint and Pach (1984)

Table 2.1. (Contd.)

No.	Field/Trend	Location	Reservoir age (unit)	Reservoir Lithology	References
27	Casablanca Field (and others)	Tarragona Basin (Spain)	U. Jurassic	Limestone, some dolomite	Garcia-Sineriz et al. (1980); Watson (1982); Esteban (1991)
28	Un-named	Bresse Basin	Jurassic	Limestone	Fontaine et al. (1987)
29	Amposta Marino Field (and others)	Tarragona Basin (Spain)	L. Cretaceous (Montsia Fm.)	Limestone	Garcia-Sineriz et al. (1980); Wigley et al. (1988); Bouvier et al. (1990)
30	Field "A"	Mediterranean Basin	L. Cretaceous	Limestone	Fontaine et al. (1987)
31	Stuart City Trend	San Marcos Aarch and Texas Gulf Coast (USA)	L. Cretaceous (Edwards Fm.)	Dolomite, limestone	Rose (1972); Bebout and Loucks (1974); Wilson (1980a.b; 1985)
32	North Field	Qatar (Persian Gulf)	L.-M. Cretaceous (Mishrif Fm.)	Dolomite, limestone	Aves and Tappmeyer (1985)
33	Golden Lane Trend	Tampico Embayment (Mexico)	M. Cretaceous (El Abra Fm.)	Limestone	Viniegra and Castillo-Tejero (1970); Coogan et al.(1972)
34	Campeche-Reforma Trend	Mexico	L.-U. Cretaceous, U. Jurassic locally	Dolomite, some limestone	Santiago-Acevedo (1980)

Table 2.1. (Contd.)

No.	Field/Trend	Location	Reservoir age (unit)	Reservoir Lithology	References
35	BuHasa, Fahud, Fateh, and Natih fields	Saudi Arabia, United Arab Emirates (Persian Gulf area)	Cretaceous (Wasia Group)	Limestone	Tschopp (1967); Twornbley and Scott (1975); Wilson (1980) a,b; 1985); Harris and Frost (1984); Jordan et al. (1985);Videtich et al. (1988)
36	Rospo Mare Field	Italy	Cretaceous	Limestone	Dussert et al. (1988)
37	Intisar “D”	Sirte Basin (Libya)	Paleocene (Intisar Fm.)	Limestone	Brady et al. (1980)
38	Kirkuk field	Iraq	Eocene-Oligocene (Fars Fm.)	Limestone, dolomite	Daniel (1954)
39	Bombay High Field	India	Miocene	Limestone	Rao and Talukdar (1980)
40	South Alamyshik Field	U.S.S.R. (Uzbekistan)	Paleogene	Limestone	Khutorov (1958)

Table 2.2. Other paleokarst reservoirs locations not in Mazzullo and Chilingarian (1996) No. are location numbers in Figure 2.1.

No.	Field/trend	Location	Reservoir age (unit)	Resevoir lithology	References
41	Un-named	Tarim Basin (China)	L. Precambrian (Qigebulake)	Dolomite	Yie and Liu (1991)
42	Weiyuan Field	Sichuan Basin (China)	Precambrian (Dengyin)	Dolomite	Wei et al. (2008)
43	Boonsville Field	Fort Wort Basin (Texas)	Cambro-Ordovician (Ellenburger)	Dolomite	Hardage et al., (1996); Sullivan et al., 2006); McDonnell et al., (2007).
44	Unnamed Field	Cherokee Platform (Oklahoma)	Cambro-Ordovician (Arbuckle)	Dolomite	Keeling (2018)
45	Un-named	Tarim (China)	L. Cambrian - E. Ordovician (Quilitage)	Dolomite	Yie (1991); Hu (1992)
46	Un-named	Tarim Basin (China)	L. - M. Ordovician (Yinjianfang)	Limestone	Zeng et al. (2010, 2011a and b)
47	Un-named	Arkoma Basin (Oklahoma)	Ordovician (Viola Fm.)	Limestone	Kumbalek (2015); Aboaba and Liner (2018, 2019, 2020)
48	Un-named	Cherokee Platform (Oklahoma)	L. Ordovician - E. Devonian (Hunton Group)	Limestone	Milad and Slatt (2017)
49	Un-named	Canning Basin (Australia)	M. Ordovician (Nita)	Dolomite	Karajas and Kernick (1984); Bentley (1984)
50	Un-named	Williston Basin (Montana)	Silurian (Interlake)	Dolomite	Roehl (1985)

Table 2.2. (Contd.)

No.	Field/trend	Location	Reservoir age (unit)	Resevoir lithology	References
51	Grosmont Bitumen Area	Western Canadian Sedimentary Basin (Alberta, Canada)	U. Devonian (Grosmont Fm.)	Limestone	Russel-Houston and Gray (2014)
52	Unnamed Field	Sichuan Basin (China)	E. Carboniferous (Unnamed Fm.)	Dolomite	Yang (1986)
53	Un-named	Paradox (Utah)	E. Carboniferous (Leadville)	Dolomite	Miller (1985)
54	West-east trend, Billings East Field, Ponca City Field etc.	Cherokee Platform (Oklahoma)	Mississippian (Miss Chat, Miss Lime)	Chert; Limestone	Rogers (2001)
55	Un-named	Sedgwick Basin (Kansas)	Mississippian	Chert; Limestone	Rogers (2001)
56	Un-named	Arkoma Basin (Arkansas)	Mississippian (Boone Fm.)	Limestone	Moser (2016)
57	Un-named Field	Arkoma Basin (Oklahoma)	Pennsylvanian (Wapanucka Fm.)	Limestone ;	Aboaba and Liner (2018, 2019, 2020)
58	Kashagan Field	Precaspian Basin (Kazakhstan)	Carboniferous	Limestone	Sorkhabi (2013)

Table 2.2. (Contd.)

No.	Field/trend	Location	Reservoir age (unit)	Resevoir lithology	References
59	Alta and Gohta Fields	Loppa High, Barents Sea (Norway)	L. Carboniferous - E. Permian (Gippsdalen Gp.)	Dolomite	Hunt et al. (2003, 2010); Sayago et al., (2012); Ahlborn et al., (2014); Matapour et al. (2018).
60	Nang Nuan Field	Chumphon Basin (Thailand)	Permian (Ratburi Group)	Limestone; Dolomite	Heward et al. (2000)
61	South Pars Field	Persian Gulf (Qatar)	L. Cretaceous (Sarvak Fm.)	Limestone	Burberry et al. (2015, 2016)
62	Un-named	Maracaibo Basin (Venezuela)	L. Cretaceous (Apon Fm.)	Limestone	Castillo and Mann (2006)
63	Various oil fields (e.g. Garoupa)	Campos Basin (Brazil)	E. Cretaceous (Macae Gp.)	Limestone	Basso et al. (2018)
64	Un-named	Mesopotamia Basin (S. Iraq)	Cretaceous (Mishrif Fm.)	Limestone	Cantrell et al. (2020)
65	Floridian Aquifer System	Biscayne Bay (Florida)	Paleocene - E. Oligocene (Oldsmar Fm, Avon Park Fm, Ocala Limestone, Suwannee Limestone)	Limestone	Cunningham and Walker (2009)
66	Al Shaheen Field	Persian Gulf (Qatar)	Paleocene - E. Eocene (Umm Er Radhuma)	Limestone, dolomite	Zampetti et al. (2014)

Table 2.2. (Contd.)

No.	Field/trend	Location	Reservoir age (unit)	Resevoir lithology	References
67	Various fields (e.g., Vorwata)	Papua New Guinea	M. Eocene - Oligocene (Faumai Fm.)	Limestone; Dolomite	Birt et al. (2015)
68	Panna-Mukta fields	Gulf of Khambhat (India)	Eocene (Bassein Fm.)	Limestone	Barnett et al. (2015); Wright (2016)
69	Un-named	California Basin (California)	Miocene (Monterey Fm.)	Chert	Bramlette (1946)
70	Mackerel Field	Gippsland Basin (Australia)	Miocene	Limestone	Brown (1985)
71	Liuhua Field	Pearl River Mouth Basin (China)	L. Miocene (Zhujiang Fm.)	Limestone	Story et al. (2000)
72	Luconia Province	Sarawak (Malaysia)	M. Miocene (Jintan Fm.)	Limestone	Vahrenkamp et al. (2004)

Table 2.3. Worldwide examples of paleokarst measurements on seismic data. Geophysical information on selected sites in Figure 2.1.

No.	Seismic Parameters: frequency (Hz), horizontal resolution (HR)[m], vertical resolution (VR) [m]	Velocity [m/s]	Paleokarst Dimensions [m]	Reference(s)
5	--	--	Paleocave complex 2400 m in length, varying widths up to 10.5 km, thickness of 46-61 m high.	Purves et al., (1992).
23	--	High velocity, low porosity carbonate host rock, collapse rocks show low velocity	Sinkhole diameter 305-1830 m; sinkhole depth is 9-40 m; vertical collapse of 488 m extends into overlying San Andreas carbonate	Zeng et al., (2006)
43	10-150 Hz	--	Sinkhole diameters 150-1200 m; large collapse structures with diameters of 2000 m. Vertical collapse of 760 m extends into the overlying formations of Pennsylvanian age. Sinkholes are 610 – 1830 m apart	Hardage et al., (1996); Sullivan et al., (2006); McDonnell et al., (2007).
44	10-105 Hz, HR [49 m], VR [24m]	Arbuckle interval velocity is 6100 m/s	The paleocave system has an areal extent of 2.7 square kilometers and an average passage width of 260 m	Keeling (2016); Aboaba and Liner (2017)
46	5 -55 Hz, dominant frequency of 25 Hz in Paleozoic section, HR [120 m], VR [60 m]	6000 m/s is host rock velocity, collapsed paleocave with cave sediments had a velocity of 3500 m/s	Sinkhole diameter 50-500 m, sinkhole depth 20-150 m, paleocave complex 200-600 m width, and thickness up to 500 m; canyon width is 100-400 m with depths of 20-100 m; tower karst has heights of 10-150 m.	Zeng et al., (2010, 2011a and b)

Table 2.3. (Contd.)

No.	Seismic Parameters: frequency (Hz), horizontal resolution (HR)[m], vertical resolution (VR) [m]	Velocity [m/s]	Paleokarst Dimensions [m]	Reference(s)
47	15-105 Hz, dominant frequency of 60 Hz; HR [34 m] VR [13 m]	Average velocity is 3048 m/s	Sinkhole diameters range from 50-1067 m, average diameter is 237 m and sinkhole depth from 5-18 m. Pipe features can reach 490m	Kumbalek (2015); Aboaba and Liner, (2018, 2020)
48	--	--	Sinkhole diameters range from 350-700 m with a depth of 90 m	Milad and Slatt (2017)
53	--	--	Sags varying from a few 100 m - 1 km, dendritic patterns, paleokarst height of 8-84 m shows random distribution	Zampetti et al., (2014).
56	8-98 Hz. Dominant frequency 53 Hz, HR [27 m], VR [55m]	Boone Limestone velocity is 5800 m/s	Sinkhole diameters 300-1000 m; average diameter is 632 m; sinkhole depth is 100 m	Moser, 2016
59	5 –35 Hz; peak frequency of 25 Hz recorded in Paleozoic section, HR [--], VR [45m]	Velocities are greater than 4500 m/s	Sinkhole diameters 50-450 m, sinkhole depths of 150 m, vertical collapse of 300 m; paleocave complex 40-50 km length, 10-12 km width and thickness of 10-150 m	Hunt et al., (2003, 2010); Sayago et al., (2012); Ahlborn et al., (2014).

Table 2.3. (Contd.)

No.	Seismic Parameters: frequency (Hz), horizontal resolution (HR)[m], vertical resolution (VR) [m]	Velocity [m/s]	Paleokarst Dimensions [m]	Reference(s)
61	--	--	34 near circular sinkholes mapped. Sinkhole diameters 0.8-10.2 km; depths of 15-80 m; 1100 m thick interval below sinkhole, related to vertical collapse or poor imaging; 43 vertical pipe columns, 2 km in height and up to 5.5 km in diameter	Burberry et al., (2015, 2016).
62	--	--	Sinkhole 600 m in width and 100 m deep.	Castillo and Mann (2006).
63	0-125 Hz with a dominant frequency of 35 Hz, VR [15 m]. HR [--]	--	40 closed depressions mapped. Sinkhole diameters 70-600 m. Sinkhole depths 5-60 m. Valley average for four valleys is 722 m, depth average for four valleys is 36 m. Canyon average width is 1.2 km, canyon depth is 107 m	Basso et al., (2018).

Table 2.3. (Contd.)

No.	Seismic Parameters: frequency (Hz), horizontal resolution (HR)[m], vertical resolution (VR) [m]	Velocity [m/s]	Paleokarst Dimensions [m]	Reference(s)
65	--	--	Five narrow seismic sag structural systems with inner sag width from 167-733 m, and a mean of 355 m. The narrow sag systems are 3.2 km and 7.2 km apart. Six broad seismic sag seismic structural systems range from 1092-4886 m, and a mean of 2479 m. Distance between broad sag features range from 0.8-5 km	Cunningham and Walker (2009)
67	--	--	Tower karst measuring 250 m in diameter with a height of 150 m. Sinkholes up to 1 km wide and 200 m deep	Birt et al., (2015)
68	--	--	Vertical collapse features 350 m deep and about 500 m across	Barnett et al. (2015); Wright (2016)
70	--	--	Sinkhole diameter 200-500 m	Brown et al. (1985)
71	180 Hz field data. Peak frequencies up to 240 Hz. Carbonate bank has a frequency of 120-180 Hz. HR [--], VR [--]	Limestone velocity ranges from 3000 m/s to >6000 m/s	Typical sinkhole diameter 100-500 m, sinkholes may extend to 1000 m, sinkhole depth is 15 m. Vertical collapse is 134-1010 m	Story et al. (2000), Zampetti et al. (2005)

Table 2.3. (Contd.)

No.	Seismic Parameters: frequency (Hz), horizontal resolution (HR)[m], vertical resolution (VR) [m]	Velocity [m/s]	Paleokarst Dimensions [m]	Reference(s)
72	6-50 Hz. Predominant frequency of 25 Hz	4000 m/s limestone velocity with an average porosity of 25%	Large cave several hundred meters in diameter, dendritic and drainage patterns.	Vahrenkamp et al. (2004)

CHAPTER 3

Interpretation of Paleokarst Collapse Features in the Arkoma Basin using 3D Seismic and Well Logs in the Arkoma Basin, Oklahoma. (Published, 2020)

Olanrewaju Aboaba[1] and Christopher Liner[1], University of Arkansas, Department of Geosciences

This paper was published by AAPG/SEG journal Interpretation in 2020

Abstract

Paleokarst regions worldwide are repositories for hydrocarbons, mineral deposits, and groundwater. Time structure maps were generated for the Ordovician Viola Limestone, Mississippian Caney Shale, and Pennsylvanian Jefferson Sandstone and Wapanucka Limestone. Isochron maps indicate pronounced visible sinkhole time thickening in the Viola-Caney and Caney-Jefferson intervals relative to the Jefferson-Wapanucka. Sinkhole features in the Viola exhibit mappable structural depression, characterized by lower positive amplitude, higher seismic variance, and most-negative curvature. Curiously, spatially coincident sinkhole features in the shallower Wapanucka display the opposite characteristics relative to adjacent areas that have not been modified, namely, higher positive amplitude and lower seismic variance with nomappable time structure relief. Seismic amplitude analysis based on well logs and Gassmann modeling indicate that the Viola has a reduction in limestone acoustic impedance inside sinkholes that allows estimation of increased porosity near 10%. Identical analysis for the Wapanucka suggests that no reasonable alteration of the limestone acoustic impedance alone can account for the observed amplitude behavior, implying that the limestone and overlying shale must be altered in sinkhole areas. Some of these interpreted sinkhole features coincide with vertical pipe structures with up to 490 m (1610 ft) vertical extent, diameter up to 520 m (1700 ft),

and separation of at least 460 m (1510 ft). We interpret the Viola sinkhole features and associated vertical pipes to be part of a mature epigene karst system. Conversely, the shallower and more subtle Wapanucka sinkholes we interpret as related to an immature mixed karst system with epigene and hypogene elements. Our study indicates for the first time the seismic evidence of pipe features that extend both below and above the Viola, and the presence of Wapanucka sinkhole features in the Arkoma Basin of Oklahoma, which provides a better understanding of paleokarst occurrence and its possible impact on resource exploration.

Introduction

Paleokarst is karst that is not hydrologically connected to the current earth's surface and buried by younger sediments (Ford and Williams, 2007). Hydrocarbons, minerals, and groundwater are found in paleokarst reservoirs. Paleokarst furnishes information about past geologic and hydrologic conditions, sea level and climatic changes (Palmer and Palmer, 2011). It can cause damage to property and civil engineering works (Waltham and Fookes, 2003), as well as lost circulation and complete loss of mud in hydrocarbon drilling (Andre and Doulcet, 1991; Lomando et al., 1993; Zhao et al., 2014). James and Choquette (1988) note that the development of karst landforms occurs by external and inherent factors. The external factors include climate (precipitation, evaporation, and temperature), base level (relief and elevation, sea level, or local water bodies), plant life, and duration of time; and inherent factors such as structure and stratigraphy (strata attitude, unconfined or confined aquifers, and structural conduits) and lithology (fabric and texture, bedding thickness, fractures, stratal permeability, mineralogy, and bulk purity). Two broad categories of karst development are recognized, epigene and hypogene (Palmer, 1991; Klimchouk, 2015). Epigene, or meteoric, karst is associated with an unconformity surface involving the interaction of meteoric water with carbon dioxide from soil

organic matter to form carbonic acid originating at or close to the earth's surface (Palmer, 2007; Klimchouk, 2015; Milad and Slatt, 2017). Soil biogenic activity increases with temperature in terrains at low altitudes and latitudes, such as humid, temperate, and tropical regions. Hypogene karst is associated with carbonate dissolution by confined, deep-seated hydrothermal fluids (Palmer, 1991; Loucks, 1999; Klimchouk, 2007, 2009a, 2009b), or the acceleration of epigene processes can also produce similar fluids (Palmer, 1991). Those fluids can include sulfuric acid breached from hydrocarbon oilfields (Hill, 1995), as well as high-temperature and -pressure igneous basement hydrothermal fluids migrated along faults (Palmer, 1991; Burberry et al., 2016), or thermal convection of hydrothermal fluids (Wright and Harris, 2013). Unlike epigene karst, hypogene processes are independent of climate (Klimchouk, 2009a, 2009b). Sinkholes are closed depressions of subsurface drainage diagnostic of epigene karst topography (Waltham et al., 2005). Collapse breccias with infill sediments are often present in sinkholes (Loucks, 1999), as well as open shafts into cave networks (Waltham et al., 2005). Figure 3.1 illustrates a generalized karst model. Vertical karst pipe structures become connected by hydrothermal flow, tectonic activity, mineralization, and collapse (Waltham et al., 2005; Sullivan et al., 2006; Sun et al., 2013; Burberry et al., 2016) with hypogene-formed sinkholes enhanced during subaerial exposure (Sullivan et al., 2006; Burberry et al., 2016). Wright (2016) notes that the circular collapse features that occur in hypogene networks may be interpreted as surface sinkholes originally associated with meteoric karst. Sinkholes and associated pipe features have been identified from 3D seismic data in the Fort Worth Basin (Hardage et al., 1996; McDonnell et al., 2007), the Persian Gulf (Burberry et al., 2016), the Pearl River Mouth Basin, China (Story et al., 2000; Heubeck et al., 2004; Sun et al., 2013), and Florida (Cunningham and Walker, 2009; Cunningham, 2015; Cunningham et al., 2018). In 3D seismic data, karst pipes are often seen to

narrow upward, develop a cylindrical to vertical conical geometry, and exhibit a spectrum of disruption of stratal seismic reflections from localized sag features to completely chaotic (Cartwright et al., 2007; Sun et al., 2013).Pipes are believed to have formed over an extensive time period (Waltham et al., 2005).

There have been limited seismic studies of paleokarst in the Arkoma Basin, Arkansas-Oklahoma. Brinkerhoff (2007) uses a waveform classifier to distinguish the various stages of karsting, specifically paleocave development, incipient karst collapse, and noncollapse regions in the Ordovician-Devonian Hunton Limestone in the Arkoma Basin of Oklahoma. Moser (2016) uses curvature to map sinkholes with an average diameter of 630 m (2070 ft) in the Mississippian Boone Limestone in the Arkoma Basin of Arkansas. Milad and Slatt (2017) map sinkholes in the Hunton and Viola Formations in Pottawatomie County, Oklahoma, on the Cherokee platform 92 km (57 mi) northwest of the current study area. Observed sinkhole diameters range from 350 to 700 m (1150–2300 ft). Using the same 3D seismic survey as the current study, Kumbalek (2015) using the same 3D seismic survey as the current study mapped and identified Viola paleokarst expressed as sinkholes with an average diameter of approximately 280 m (780 ft) that occurred in only 4.1% of the 460 km^2 (approximately 180 mi^2) survey area.

This paper reports the first seismic mapping in the study area of the Mississippian Caney Shale, the Pennsylvanian Jefferson Sandstone, and the Pennsylvanian Wapanucka Limestone, as well as the Ordovician Viola Limestone. We identify and measure sinkhole and vertical pipe features in the Arkoma Basin of Oklahoma using horizon time structure maps and isochron maps, optimized seismic attribute volumes of variance, curvature, and amplitude maps, sinkhole feature amplitude analysis is calibrated to the Gassmann equation to form a predictive rock-physics model, and we extend Kumbalek's (2015) Viola sinkhole analysis. Evidence is presented for

paleokarst collapse that extends below the Viola and into shallower horizons and the first published description of sinkhole features in the Wapanucka Limestone. This study has broad applications in paleokarst science and hydrocarbon exploration.

Geology

The study area is in the western Arkoma Basin, a peripheral foreland basin formed by collision of the North American and Gondwanan plates during early Mississippian through middle Pennsylvanian time (Suneson, 2012). It is a structural-sedimentary basin that covers much of eastern Oklahoma and western Arkansas and stretches south to the Choctaw Fault (Amsden, 1984). Figure 3.2a shows the study area, Arkoma Basin, and adjacent basins along the Ouachita fold belt. Figure 3.2b shows a cross section across the Arkoma Basin and the Ouachita fold belt. Surface rocks of the western Arkoma Basin trend east–northeast with regional northwest dip (Berry and Trumbly, 1968). The youngest beds are visible on the northwest edge of the basin, whereas the oldest beds occur near the Choctaw Fault. The Wapanucka Limestone and older rocks dip regionally to the southeast (Berry and Trumbly, 1968). Depositional thinning in the Atoka and younger formations are evident in growth structures (Berry and Trumbly, 1968), whereas south-dipping faults cut through early Pennsylvanian and older rocks to define the basin (Perry 1994). Compressional folds show substantial structural changes in the southern region of the basin adjacent to the Ouachita front (Berry and Trumbly, 1968; Suneson, 2012), and drape anticlines are present in the northern Arkoma Basin over normal faults (Suneson, 2012).

The deposition of Cambro-Ordovician Arbuckle Dolomite and basal sandstone occurred in a gradually subsiding platform near a geosyncline located to the southeast receiving some input of coarse clastics. During Simpson time, the region was subjected to an influx of clastic

sediments that formed the mid-Ordovician Joins and Oil Creek sandstones and shales, and their northern equivalents, the Burgen-Tyner sequence. In the south and southeastern shelf area, carbonate production was high during McLish and Bromide times with marginal amounts of shale and sandstone. The absence of coarse clastic rocks and a stable platform initiated the deposition of the upper-Ordovician Viola Limestone and Sylvan Shale, and the Silurian-Devonian Hunton Limestones (Arkoma Basin Study Group, 1961). In the study area, the Viola has an average thickness of 50 m (163 ft). The deposition of the Viola Limestone occurred in an extensive shallow epicontinental sea with no apparent orogenic activity in south-central Oklahoma (Wengerd, 1948; Mairs, 1966). After the deposition of the Viola, the epeirogenic tectonic movement exposed the Viola Limestone to subaerial erosion (Wengerd, 1948). Sykes et al. (1997a) and Sykes (1997b) note that the timing of karst development in the Viola is pre-Pennsylvanian in age, with vugs, solution-enlarged fractures, and channels in the upper Viola (Welling/Fernvale) suggesting dissolution before deposition of the Sylvan. The presence of sphalerite, copper sulfides, and pyrite with asphalt has been reported in the Viola west of the study area in Pontotoc County (Sykes et al., 1997a), indicating some hydrothermal activity and associated hypogene karst likely due to movement of brine and petroleum below the organic Sylvan Shale, a confining and effective aquitard unit over the Viola.

A marine transgression led to deposition of the Sylvan Shale (Amsden, 1984), with an average thickness in the study area of approximately 29 m (96 ft). The overlying Hunton Limestone does not exceed 2 m (8 ft) thickness in the study area, and thins from the southwest to the northeast due to local erosion. Shelf subsidence of the Hunton surface resulted in the buildup of the transgressive Misener Sandstone and Woodford Shale, with the Woodford thickness of 52 m (171 ft). The Mississippian Mayes-Caney Shale sequence records a clastic

advancement from the south, with a rapid thinning of the shale to the north across the platform due to slower deposition and rapid subsidence of the basin to a southward thickening of the Pennsylvanian Caney Shale, also called the Goddard or Springer Shale (Elias, 1956; Arkoma Basin Study Group, 1961). The average thickness of the Mayes-Caney Shale is approximately 146 m (482 ft) and the Goddard Shale is approximately 54 m (176 ft). Jefferson Sandstone lenses are found at the edge of the platform in the upper section of the Pennsylvanian Springer/Caney Shale (Arkoma Basin Study Group, 1961). The Jefferson is composed of more than one sandstone that divides and amalgamates suggesting bar facies and variable depositional surroundings in a marine environment (Andrews, 2007a, 2007b). The Jefferson Sandstone has an average thickness of 34 m (110 ft) in the study area. Cromwell Sandstone deposition occurred with amplified movement to the south in a stable environment. Thin shale streaks in the sandstone indicate variability in subsidence rates. The average thickness of the Cromwell Sandstone is approximately 50 m (164 ft). The Wapanucka Limestone formed in shallow waters before initiation of basin subsidence characterized by superficial and localized movements of the seafloor with a slow rate of deposition (Arkoma Basin Study Group, 1961; Suneson, 2012). The average thickness of the Wapanucka is approximately 47 m (153 ft). Before the advancement of the Atoka Sea, Morrowan rocks were subject to erosion that increased northward across the basin. During Atokan time, the deposition of coarse clastic rocks occurred throughout the basin with increased subsidence during the evolution of the region into a foreland basin. A northward transgression occurred depositing younger shallow marine sands and shale over older Atoka units in the subsiding trough (Arkoma Basin Study Group, 1961). Figure 3.3 shows the stratigraphy of well C in the study area.

Available Data

The 3D seismic and wireline data from three wells used in this study were made available by Devon Energy. Figure 3.4a shows the seismic data coverage and key well locations. Table 1 shows the formation tops and thicknesses encountered in the three wells. The data straddle the Hughes-Coal County line in southern Oklahoma. The seismic data have a 1 ms sample rate, 2.7 s record length, and bin size of 33.5 × 33.5 m (110 × 110 ft), and they consist of prestack time-migrated data with 798 east–west crosslines and 698 north–south inlines. The processing datum is 274.3 m (900 ft) with a replacement velocity of 3048 m⁄s (10,000 ft⁄s) and areal coverage of 470 km^2 (180 mi^2). Fourier analysis indicates the minimum and maximum frequencies of 13 and 102.5 Hz at negative 20 dB, with a dominant frequency of 57.5 Hz (Figure 3.4b). Vertical seismic resolutions for the Viola and Wapanucka are 27 m (89 ft) and 25 m (82 ft), respectively. Well A is located in Hughes County with total depth (TD) of 1847m (6059 ft) in the Woodford Shale. Well B in Coal County had TD of 2417 m (7931 ft) to the base of the Viola Limestone. Well C, also in Coal County, had TD in the Simpson Group (McLish) at 2469 m (8102 ft).

Methods

Three wells, herein called A, B, and C, were used to correlate seismic events to geologic formation tops. Table 1 shows the formation tops and thicknesses in the three wells. A synthetic seismogram generated in well B is shown in Figure 3.5. This well was used because it had a long interval of sonic and density log data that reached the Viola. Check-shot data were not available. A zero-phase 200 ms wavelet (taper 25 ms) was extracted in an 1100 ms time window based on field traces in a 10 × 10 bin area centered on the well location. A time shift was applied to the synthetic to match the field seismic data, but no stretch/squeeze was required. Wireline log plots were generated for the Viola and the Wapanucka Formations over a 91 m (300 ft) interval. This

interval started 100 ft (30m) above the carbonate formation tops in wells C and B. Figure 3.6 shows the gamma ray (GR) and mineralogy rock fractions in well C. Figure 3.7 shows GR, acoustic (DTCO), and shear (DTSM) velocities in well B. The mapped horizons of interest are shown in the yellow circles labeled V, C, J, and W representing the Ordovician Viola Limestone, Mississippian Caney Shale, Pennsylvanian Jefferson Sandstone, and Pennsylvanian Wapanucka Limestone, respectively (Figures 3.5, 3.8a, 3.8b, 3.9, and 3.10). The horizons are positive amplitude reflections. Time structure maps were generated for the interpreted intervals (Figure 3.11a–3.11d), along with isochron (time-thickness) maps for intervals among the Viola-Caney (VC) (Figure 3.12a), Caney-Jefferson (CJ) (Figure 3.12b), and Jefferson-Wapanucka (JW) (Figure 3.12c).

To optimize imaging of karst-related features, seismic attribute parameter tests for variance were performed on a 1400 ms cropped seismic amplitude data volume (54 km^2 [21 km^2]) covering wells B and C. All variance calculations used a 3 × 3 bin operator. Two triangular weighted time filters were tested (5 and 15 samples), as well as with/without dip correction of two types (horizontal variance and variance computed along a dipping plane). The dipping plane method uses principal component analysis (PCA) with a directional parameter (inline, crossline, and vertical scale) of 1.5 and a 0.6 plane confidence threshold. PCA dip correction was for confidence >0.6, whereas other regions were processed with horizontal variance dip correction (Gersztenkorn and Marfurt, 1999). Dip guided smoothing was the final variance parameter tested in conjunction with the operator size length and dip corrections. In total, six variance volumes were computed and examined for optimum detail at the Viola (Figure 3.3.13) and Wapanucka (Figure 3.14) horizons. A visual inspection determined that the optimum variance parameters for the Viola were those of Figure 3.13c, which were then applied to the

entire survey to extract horizon slices for the Viola, Caney, and Jefferson (Figure 3.15a–3.15c). The variance parameters of Figure 3.14f were deemed optimum for the Wapanucka and were applied to the entire survey to generate the horizon slice of Figure 3.15d.

The most-positive and most-negative curvature volumes (Chopra and Marfurt, 2007) were computed using an operator size of (nt, nx, ny) = (12, 1, 1). Horizon slices were extracted from each curvature volume on four interpreted horizons (Figure 3.16a–3.16d). Amplitude maps were generated for the four horizons (Figure 3.17a–3.17d). Rose diagrams of faults/lineaments for the Viola and Wapanucka from the curvature volumes are shown in Figure 3.18.

Diameters and distances between sinkholes were estimated, along with two-way traveltime (TWT) vertical extent of pipe features converted to depth, using a sonic-derived time-depth function given by

$$Z = 0.0009\ T^2 + 3.8498\ T + 118.57 \quad (1)$$

where T is the TWT (ms) and Z is the depth (ft).

Interpretation of Results

Wireline Analysis

Wireline logs in well C show that the carbonate rock fraction is higher in the Viola (Figure 3.6a) than the Wapanucka (Figure 3.6b): Specifically, mineralogy fractions indicate that the Viola has an average of 88% carbonate, 9% quartz, and 3% clay, whereas the Wapanucka average composition is 77% carbonate, 14% quartz, and 8% clay. Other mineralogy fractions are negligible. Bogli (1980) notes that the presence of impurities such as clay and quartz in limestone lowered the capacity for karstification, implying that the Viola Limestone has greater

karst potential than the Wapanucka. However, we note that other factors such as climate, hydrology, and the structural setting may be preponderant. The mineralogy logs also indicate the presence of coal in the shale section overlying the Wapanucka.

The Viola has an average acoustic velocity (DTCO) of 6224 m⁄s (20,420 ft⁄s or 48.97 µs⁄ft) and an average shear velocity (DTSM) of 3216 m⁄s (10,551 ft⁄s or 94.78 µs⁄ft) (Figure 3.7a). The Wapanucka average DTCO is 5872 m⁄s (19,265 ft⁄s or 51.91 µs⁄ft) and an average DTSM is 3072 m⁄s (10,079 ft⁄s or 99.22 µs⁄ft) (Figure 3.7b). The higher velocities for acoustic and shear in the Viola compared to the Wapanucka are consistent with a higher carbonate fraction. The results from the mineralogy rock fractions and velocities indicate that the Viola has a higher potential for karst development than the Wapanucka.

Seismic Analysis

In this paper, the term “pipe” refers to a disrupted, semichaotic volume of seismic data, “sinkhole” means a concave-upward depression across a seismic reflection event occurring in carbonate, and “sag” means a quasicircular concave-upward depression in siliciclastic rocks.

Figure 3.8a and 3.8b shows dip and strike geoseismic sections, respectively, through well B, which were used to generate the synthetic seismogram of Figure 3.5. The mapped horizons are shown in the yellow circles labeled as V, C, J, and W representing the Viola Limestone, Caney Shale, Jefferson Sandstone, and Wapanucka Limestone, respectively. All of these horizons are positive polarity events representing a soft to hard response at the formation boundary. Vertical pipe features are indicated by bounding dashed white lines and are visible on the horst block (Figures 3.8a, 3.9c, and 3.10c), but not adjacent graben blocks (Figure 3.8b). We observe that sinkholes and sags are often associated with these pipe features.

The faulting architecture consists of normal faults with drags and folds. The faults compartmentalize the section into horst and half-grabens (Figures 3.8–3.10). In map view, the predominant faults strike northeast–southwest, and other strike orientations include west–east, northwest–southeast, and north–south. We observe that these faults compartmentalize the study area into five separate fault blocks (Figures 3.11, 3.12, 3.15, 3.16, and 3.17). For convenience, the fault blocks are named beginning from the north to the south of the study area as follows: HG1, G1, H1, HG2, and HG3, where HG is a half-graben, G is a graben, and H is a horst.

From rose diagrams in Figure 3.18, two principal fault orientations are seen in the Viola along N40°E–N50°E and N50°E–N60°E, whereas only one is evident for the Wapanucka along N50°E–N60°E. This follows the regional trend of the Ouachita fault. This predominant northeast axis along the regional trend of the Ouachita fault suggests that the orientation of tectonic activity is consistent from Ordovician Viola time to Pennsylvanian (Morrowan) Wapanucka time.

Sinkholes on the Viola and sags on Caney reflections are sometimes associated with pipe features. The pipes are subvertical with a probable narrowing upward (Figures 3.8–3.10). Sinkhole and sag features are visible above these pipes. Low amplitudes and disrupted reflections characterize the internal configuration of the pipe. Similar features are known in the Pearl River Mouth Basin (Sun et al., 2013) and Fort Worth Basin (McDonnell et al., 2007). In our data, some pipes extend above 1.2 s, below the Viola into the Simpson Group (Figures 3.8a, 3.9, and 3.10), and possibly extend downward to the acoustic basement. However, this is not clearly visible on the amplitude section due to deep image and resolution limits. Outside of pipe features, reflections show greater continuity. As expected, the volumetric variance is greater in the pipes than adjacent undisturbed data volumes (Figures 3.9b and 3.10b). Taken together, these

observations suggest rock fracturing and/or dissolution. These low-amplitude, high-variance pipe features indicate collapse and infill, which we interpret as probable breccia pipes (Waltham et al., 2005).

Away from the pipes, the surrounding host rock has low variance and consistent amplitude, which we interpret to be unkarsted rock that has not undergone significant dissolution or collapse. Vertical faults are likely bounding the sag/pipe features and may have served as conduits for deep-seated hydrothermal fluids migrating during the Ouachita Orogeny in the Pennsylvanian (Kupecz and Land, 1991), or they may be due to meteoric water that percolated along fracture networks enhancing carbonate dissolution. Fracture networks may be linked with vertical faults bounding pipe and sinkhole features.

Seismic Attribute Maps

Time and isochron. —The structural high in the study area rises toward the west from the H1 horst block. The Viola and Caney maps (Figure 3.11a and 3.11b) show structural relief that highlights circular to elliptical sinkhole features. The Jefferson Sandstone and Wapanucka Limestone time maps (Figure 3.11c and 3.11d) do not exhibit any mappable sag or sinkhole structural relief. Isochron maps for the VC, CJ, and JW are shown in Figure 3.12a–3.12c with sinkholes features indicated by the red arrows. VC and CJ isochores show thinning over sinkhole features. Subtle visible lineaments trending N70°E are seen in the CJ isochron in juxtaposition with sinkholes and sags. The JW isochron shows very subtle sag/sinkhole features indicating that collapse and dissolution may have been active during this interval.

Variance. —On the Viola horizon, an optimum variance was achieved with a 15 ms vertical window and dipguided smoothing, bringing out fine detail on sinkholes in the red oval area of Figure 3.13c relative to the other parameter choices. For the Wapanucka, optimum

variance parameters were 5 ms vertical window and dip guided smoothing (Figure 3.14f). For both horizons, variance shows faults with a higher definition than the associated horizon time or amplitude map. The Viola (Figure 3.15a) and Caney (Figure 3.15b) show high variance inside, and low variance outside, the sinkhole and sag features. A possible subtle circular feature is observed on the H1 block on the Jefferson Sandstone (Figure 3.15c). Sinkholes in the Wapanucka (Figure 3.15d) do not show a well-defined variance compared to the Viola sinkholes or Caney sags. The Wapanucka variance is high around the edges of the sinkhole and low within sinkholes.

Curvature. — Curvature accentuates faults in the study area, showing up-thrown fault blocks with positive curvature, and downthrown fault blocks with negative curvature. Viola and Caney horizon corendered most-positive and most-negative curvature maps (Figure 3.16a and 3.16b) reveal positive curvature on the rim of sinkhole/sag features and negative curvature inside them. For the Jefferson Sandstone, the curvature shows some subtle evidence of sags (Figure 3.16c) The curvature maps of the Caney, Jefferson, and Wapanucka reveal northeast–southwest lineaments expressed on the H1 horst that are also visible on the CJ isochore (Figure 3.12b, the yellow arrows).

Amplitude.—Figure 3.17a–3.17d shows horizon amplitude for the Viola Limestone, Caney Shale, Jefferson Sandstone, and Wapanucka Limestone, respectively, which reveals clear sinkhole/sag features on all horizons except the Jefferson. We have noted elsewhere (Aboaba and Liner, 2018, 2019) that the Viola amplitude (Figure 3.17a) shows strong positive outside sinkholes and very low to negative within sinkholes. Conversely, the Wapanucka amplitude is seen to be weak positive away from sinkholes and stronger positive inside sinkholes. In the vicinity of well B, we were able to combine amplitude, log data, and the Gassmann (1951)

theory to investigate these relationships as explained below. Reflection coefficients R for the Viola and Wapanucka Formation tops were computed for well B using 30.5 m (100 ft) average acoustic impedances

$$R_{out} = (AI_2 - AI_1) / (AI_2 + AI_1) \quad (2)$$

where AI is the acoustic impedance and subscripts 1 and2 refer to the layer properties above and below the reflecting interface, and *R*out indicates that the reflection coefficient is outside of any sinkhole feature. As usual, AI is the product of velocity and density.

To compute the reflection coefficient inside the sinkhole Rin, it is assumed that amplitude A is proportional to reflection coefficient and form a proportionality as

$$A_{out} / R_{out} = A_{in} / R_{in} \ , \quad (3)$$

where the known quantities are (Aout, Rout, and Ain) and the unknown is Rin. Solving for Rin yields

$$R_{in} = A_{in} / (A_{out}/R_{out}), \quad (4)$$

and assuming the overlying shale properties are the same across regions with and without sinkholes, we may write $AI_1 = AI_{shale}$ = constant. The interior reflection coefficient

$$R_{in} = (AI_2 - AI_1) / (AI_2 + AI_1), \quad (5)$$

can be solved for the acoustic impedance of the sinkhole interior as

$$AI_2 = AI_1 (1+R_{in}) / (1-R_{in}), \quad (6)$$

and, finally, limestone AI is related to porosity through Gassmann (1951) calibrated on wireline logs in well B. The details of the Gassmann equation can be found in Appendix A. The Gassmann equation was calibrated to acoustic impedance against total porosity from well B for the Wapanucka (Figure 3.19a) and Viola intervals (Figure 3.19b) independently and plotted across a porosity range of 30%.

Table 2 shows the analysis results for acoustic impedance, reflection coefficient, and amplitude. The key results are: The Viola calculates to a 27% impedance decrease from sinkhole exterior to interior (out-to-in), whereas the Wapanucka calculates to an 82% impedance increase from out to in.

Further investigation using the calibrated Gassmann curve for the Viola (Figure 3.19a) shows that an increase in porosity of approximately 10% can account for the computed impedance drop inside sinkholes. Thus, the inferred acoustic impedance drop for the Viola is consistent with a reasonable porosity increase related to karst activity leading to sinkholes.

The calibrated Wapanucka Gassmann plot (Figure 3.19b) shows that the maximum limestone acoustic impedance does not exceed 18 SI, but our estimated impedance from well B and amplitude ratio is 28 SI for the sinkhole interior. We conclude that no reasonable alteration of the Wapanucka Limestone by itself can explain the observed amplitude behavior. It follows that amplitude brightening seen in Wapanucka sinkholes requires softening (reduced AI) of the overlying shale, perhaps indicating hypogene karst hydrothermal activity not active in the Viola interval. We acknowledge that amplitude pattern behavior is only indirect evidence of hydrothermal activity.

Characteristics and Scale of Sinkhole and Pipe Features

In map view, sinkholes are circular to elliptical features that occur in all the fault blocks for the Viola Limestone (Figures 3.11a, 3.15a, 3.16a, and 3.17a). The sinkholes in HG2 and HG3 are adjacent to the north-bounding faults of these blocks, and not as numerous to G1 and H1. There is an alignment of sinkholes with the major faults and lineaments. Visual inspection of the mapped intervals on the time (Figure 3.11), variance (Figure 3.15), curvature

(Figure 3.16), and amplitude (Figure 3.17) maps reveal that the Viola Limestone has the greatest sinkhole development of the studied horizons. Sags are poorly developed in the Caney Shale (Figures 3.11b, 3.15b, 3.16b, and 3.17b). The Jefferson Sandstone shows no visible sags on the time or amplitude maps (Figures 3.11c and 3.17c), although subtle sags may be indicated on the variance and curvature maps (Figures 3.15c and 3.16c). On the Wapanucka horizon, no sinkholes are evident on the time structure or curvature (Figures 3.11d and 3.16d) but are visible on the variance and amplitude (Figures 3.15d and 3.17d). The Wapanucka sinkholes appear to be in the same location as pipe features that show no visible continuation into the Wapanucka on the vertical seismic sections (Figures 3.9c and 3.10c). Note that these pipes are not seen everywhere in the survey area and are more prominent on the H1 block.

Modern sinkholes with diameters greater than 100 m have been documented in the Yucatan Peninsula, Mexico; Devil's Sinkhole, Texas, and Southern China (Palmer, 2007); and Papua New Guinea, Madagascar, and Puerto Rico (Waltham, 2005). We observe that sag diameters are smaller in the Caney compared to sinkholes in the Viola. We relate this to the narrowing of the pipe features toward the top of the pipe. The sag diameters in the Caney range from 93 to 305 m (304–1000 ft) and 195 to 606 m (640–1990 ft) in the Viola. The depression reliefs measured within the Caney sags are approximately 11–33 m (36–110 ft) and 28–49 m (93–160 ft) in the Viola. As previously stated, we observed no sags or sinkholes with measurable time relief in either the Jefferson or Wapanucka. The pipes originate within the carbonate section (Viola Limestone and below) implying regions of paleokarst, with no evidence of bright spots associated with collapsed paleocave sediments, for example, in the Tarim Basin, China (Zeng et al., 2011a, 2011b). The scale of the pipe features is 150–520 m (500–1700 ft) in diameter, spaced 460–2130 m (1500–7000 ft) apart, and a vertical extent of 213–490 m (700–1600 ft). We

acknowledge that the pipe vertical extent reported here may be considered a minimum due to low seismic data quality below the Viola. Similar pipe features described in the Fort Worth Basin (Hardage et al., 1996; Sullivan et al., 2006; McDonnell et al., 2007) have a vertical extent of 760–1100 m (2500–3610 ft), in the Persian Gulf (Burberry et al., 2016) an extent of 1490–2100m (4900–6900 ft), and in the Pearl River Mouth Basin of China (Sun et al., 2013) an extent of 100–1000 m (330–3300 ft) is reported.

Possible reasons for sinkhole development

Waltham and Fookes (2003) propose an engineering classification for karst recognizing juvenile, youthful, mature, complex, and extreme categories. We use the term “mature” and “immature” to classify paleokarst features: Mature karst exhibits large sinkholes and collapse features commonly found in both temperate regions, and the wet tropics, whereas immature designates juvenile and youthful karst. Juvenile karst is formed in impure carbonates, or at deserts and periglacial zones with rare sinkholes, and youthful karst formed in temperate regions has small sinkhole features.

The higher distribution and greater development of sinkholes in the Viola with time structure relief suggest that the Viola Limestone is a more mature karst system than the immature karst of the Wapanucka. We interpret that these Viola sinkholes to be dissolution/collapse sinkholes, or cockpit karst as found in a tropical environment (Kumbalek, 2015) that formed by the lowering of the Viola Limestone surface (Waltham et al., 2005). Factors promoting karst maturity during Viola time may include clean, pure, high-strength limestone, possible long exposure, and biogenic soil gas interacting with meteoric water to form a more aggressive fluid. We do not expect to observe sinkhole formation in shale or sandstone formations because paleokarst is mainly associated with the chemical dissolution of limestone.

The presence of sags in the clastic material is likely due to the collapse of underlying carbonate sediments followed by infill and compaction. Hydrocarbon generation in the Woodford and Sylvan Shales may have provided the generation of sulfuric acid, which further enhanced dissolution and rock collapse (Sykes et al., 1997a) — factors that may have also created the pipe features. Therefore, we propose that the Viola Limestone and sinkholes and pipes are indicative of a mature paleokarst system.

We interpret the Wapanucka sinkholes to have formed during a period when there was subaerial exposure of the Wapanucka Limestone. Dannenberg (1952) proposes a major uplift known as the postlower Dornik Orogeny, which occurred before Atoka deposition during the final deposition of the Wapanucka Limestone. Seismic amplitude analysis given earlier suggests a hydrothermal alteration of the Wapanucka Limestone and overlying Pennsylvanian shales in sinkhole features. Therefore, we propose that Wapanucka sinkholes represent immature paleokarst, with hydrothermal rock property alteration with no measurable seismic relief (Aboaba and Liner, 2018).

We observe that the Wapanucka sinkhole features are curiously in the same spatial location as the deeper Viola sinkholes. McDonnell et al. (2007) report a similar phenomenon in the Pennsylvanian Marble Falls and Ordovician Ellenburger karst in the Fort Worth Basin. The lower section of the Marble Falls Formation of Central Texas, which is thought to be of Morrowan age and, thus, possibly comparable to the Wapanucka (Strimple and Nassichuk, 1965). Although we do not see any extension of the pipes cutting through the Wapanucka, the pipes may have induced subseismic faults or fractures serving as fluid pathways leading to alteration of the Wapanucka Limestone and overlying Pennsylvanian shale.

Visual examination of the interpreted Marble Falls and Ellenburger intervals on seismic sections in McDonnell et al. (2007) and Qi et al. (2014) reveal a significant structural low or sag, with pipe features extending beyond the Marble Falls into the Lower Atoka Runaway Formation. McDonnell et al. (2007) note that if there had been a paleokarst occurrence in the Marble Falls, it might have followed pathways developed by earlier applicable to our data (Aboaba and Liner, 2018).

Conclusion

We have studied four seismic horizons for evidence of paleokarst: the Ordovician Viola Limestone, Mississippian Caney Shale, Pennsylvanian Jefferson Sandstone, and the Pennsylvanian Wapanucka Limestone. In areas of good seismic data quality, probable karst collapse pipe features are observed with a vertical extent up to 490 m (1610 ft). In map view, the pipes have a diameter of 150–520 m (500–700 ft) and are spaced 460–2130 m (1510–7000 ft) apart (Aboaba and Liner, 2018). The collapse pipes extend below the Viola into the Simpson Group, and upward cutting across the Caney, but not extending to the top of the Jefferson. The pipes are characterized by high variance and are coincident with Viola sinkholes and Caney sags that show measurable relief. The collapse features below the Viola may actually be karsting of deeper features of the Simpson Group, or they may be velocity pushdown effects due to the decreased porosity and increased velocity of the Viola and the increased thickness infill of lower velocity Caney Shale.

A calibrated Gassmann and amplitude analysis for the Viola implies a drop in acoustic impedance corresponding to a porosity increase of approximately 10% inside sinkholes relative to adjacent rock. We interpret the Viola sinkholes and pipe features to be indicative of a mature epigene paleokarst system formed by subareal exposure and dissolution by meteoric waters.

The Wapanucka Limestone shows no measurable relief in sinkhole features that are observed on seismic amplitude. The Wapanucka sinkholes are seen on the H1 horst block and are spatially coincident with deeper Viola sinkholes. Calibrated Gassmann and seismic amplitude analysis of the Wapanucka Limestone shows that observed sinkhole amplitude cannot be reconciled with any plausible alteration of the limestone alone. We conclude that Wapanucka sinkholes represent immature hypogene paleokarst formed by limited subareal exposure, and later hydrothermal alteration of the Wapanucka Limestone and overlying shale.

This study provides an interpretive framework for identifying mature and immature, epigene and hypogene paleokarst, from seismic and well data, which may be applicable to similar subsurface carbonate settings worldwide.

Acknowledgments

We thank Devon Energy for providing seismic and well data, Schlumberger and CGG for software support, and the Python library Petropy used for plotting wireline logs. This paper benefitted from an early review by J. Blackstock. We thank the anonymous reviewers whose positive feedback further improved the quality of this work.

Data and Materials Availability

Data associated with this research are confidential and cannot be released.

References

Aboaba, O., and C. Liner, 2018, 3D seismic interpretation of Paleozoic paleokarst features in the Arkoma Basin of Oklahoma: 88th Annual International Meeting, SEG, Expanded Abstracts, 1698–1702, doi: 10.1190/segam2018-2998630.1.

Aboaba, O., and C. Liner, 2019, 3-D seismic characterization of paleokarst collapse features in the Arkoma Basin, Oklahoma: AAPG Search and Discovery Article #90350.

Amsden, T. W., 1984, Arkoma Basin model: Middle Ordovician through Early Devonian, in J. G. Borger, II, ed., Technical Proceedings of the 1981 AAPG Mid-Continent Regional Meeting: Oklahoma City Geological Society, 116–118.

Andre, P., and A. Doulcet, 1991, Rospo Mare Field — Italy Apulian Platform, Adriatic Sea, in N. H. Foster and E. A. Beaumont, eds., Stratigraphic traps II: AAPG Treatise of Petroleum Geology, Atlas of Oil and Gas Fields: American Association of Petroleum Geologists, 29–54.

Andrews, D. R., 2007a, Scipio NW Field — Part 1: Upper Cromwell and Jefferson Sandstone gas reservoirs in T. 8 N., R. 13 E., southwest McIntosh County, Oklahoma: The Shale Shaker, **57**, 159–171.

Andrews, D. R., 2007b, Scipio NW Field — Part 2: Upper Cromwell and Jefferson Sandstone gas reservoirs in T. 8 N., R. 13 E., southwest McIntosh County, Oklahoma: The Shale Shaker, **57**, 211–224.

Arbenz, J. K., 1989, The Ouachita system, in A. W. Bally and A. R. Palmer, eds., The geology of North America — An overview: Geological Society of America A, 371–396.

Arkoma Basin Study Group, 1961, Stratigraphy of the Arkoma Basin: Tulsa Geological Society Digest, **29**, 55–88.

Batzle, M., and Z.Wang, 1992, Seismic properties of pore fluids: Geophysics, **57**, 1396–1408, doi: 10.1190/1.1443207.

Berry, R. M., and W. D. Trumbly, 1968, Wilburton gas field, Arkoma Basin, Oklahoma, in C. L. Cline, ed., A guidebook to the geology of the western Arkoma Basin and Ouachita Mountains, Oklahoma: Oklahoma City Geological Society, 86–103.

Bliefnick, D. M., 1992, Karst-related diagenesis and reservoir development in the Arbuckle Group, Paschall #2 core, Wilburton field, in M. P. Candelaria and C. L.

Reed, eds., Paleokarst, karst-related diagenesis, and reservoir development: Examples from Ordovician-Devonian age strata of West Texas and the Mid-Continent: SEPM Publication 92-33, 137–152.

Bogli, A., 1980, Karst hydrology and physical speleology: Springer-Verlag.

Brinkerhoff, A. R., 2007, Mapping middle Paleozoic erosional and karstic patterns with 3D seismic attributes and well data in the Arkoma Basin, Oklahoma: M.S. thesis, Brigham Young University.

Burberry, C. M., C. A. L. Jackson, and S. R. Chandler, 2016, Seismic reflection imaging of karst in the Persian Gulf: Implications for the characterization of carbonate reservoirs: AAPG Bulletin, 100, 1561–1584, doi: 10.1306/04151615115.

Cartwright, J., M. Huuse, and A. Aplin, 2007, Seal bypass systems: AAPG Bulletin, **91**, 1141–1166, doi: 10.1306/04090705181.

Chopra, S., and K. J. Marfurt, 2007, Seismic attributes for prospect identification and reservoir characterization: SEG.

Cunningham, K. J., 2015, Seismic-sequence stratigraphy and geologic structure of the Floridan aquifer system near "boulder zone" deep wells in Miami-Dade County, Florida: U.S. Geological Survey Scientific Investigations Report 2015–5013.

Cunningham, K. J., J. W. Kluesner, R. L. Westcott, E. Robinson, C. Walker, and S. A. Khan, 2018, Sequence stratigraphy, seismic stratigraphy, and seismic structures of the lower intermediate confining unit and most of the Floridan aquifer system, Broward County, Florida: U.S. Geological Survey Scientific Investigations Report 2017–5109 Version 1.1.

Cunningham, K. J., and C. Walker, 2009, Seismic-sag structural systems in Tertiary carbonate rocks beneath southeastern Florida, USA: Evidence for hypogenic speleogenesis? in A. B. Klimchouk and D. C. Ford, eds., Hypogene speloeogenesis and karst hydrogeology of Artesian Basins: Ukrainian Institute of Speleology and Karstology, Special Paper 1, **280**, 151–158.

Dannenberg, R. B., 1952, The subsurface geology of Coal County Oklahoma: The Shale Shaker, **2**, 67–78.

Elias, M. K., 1956, Upper Mississippian and Lower Pennsylvanian formations of South-Central Oklahoma, in I. C. Hicks, J. Westheimer, C. W. Tomlinson, D. M. Putman, and E. L. Selk, eds., Petroleum geology of Southern Oklahoma: AAPG Special Publication, 56–79.

Ford, D., and P. Williams, 2007, Karst hydrogeology and geomorphology: John Wiley and Sons Ltd.

Fronterra Integrated Geosciences LLC, 2004, Formation image interpretation report, 1–69.

Gassmann, F., 1951, Elastic waves through a packing of spheres: Geophysics, **16**, 673–685, doi: 10.1190/1.1437718.

Gersztenkorn, A., and K. J. Marfurt, 1999, Eigenstructure-based coherence computations as an aid to 3-D structural and stratigraphic mapping: Geophysics, **64**, 1468–1479, doi: 10.1190/1.1444651.

Grotzinger, J. G., and T. H. Jordan, 2010, Understanding earth: W. H. Freeman.

Hardage, B. A., D. L. Carr, D. E. Lancaster, J. L. Simmons, Jr., R. Y. Elphick, V. M. Pendleton, and R. A. Johns, 1996, 3-D seismic evidence of the effects of carbonate karst collapse on overlying clastic stratigraphy and reservoir compartmentalization: Geophysics, **61**, 1336–1350, doi:/10.1190/1.1444057.

Harrison, W. E., and D. L. Routh, 1981, Reservoir and fluid characteristics of selected oil fields in Oklahoma: Oklahoma Geological Survey, Special Publication 81–1.

Heubeck, C., K. Story, P. Peng, C. Sullivan, and S. Duff, 2004, An integrated reservoir study of the Liuhua 11-1 field using a high-resolution three-dimensional seismic data set, in G. P. Eberli, J. L. Masaferro, and J. F. "Rick" Sarg, eds., Seismic imaging of carbonate reservoirs and systems: AAPG Memoir 81, 149–168.

Hill, C. A., 1995, H2S related porosity and sulfuric acid oil-field karst, *in* D. A. Budd, A. H. Saller, and P. M. Harris, eds., Unconformities and porosity in carbonate strata: AAPG Memoir 63, 301–306.

James, N. P., and P. W. Choquette, 1988, Paleokarst: Springer-Verlag.

Klimchouk, A., 2009a, Morphogenesis of hypogenic caves: Geomorphology, 106, 100–117, doi: 10.1016/j.geomorph .2008.09.013.

Klimchouk, A., 2015, The karst paradigm: Changes, trends, and perspectives: Acta Carsologica/Karsoslovni Zbornik, **44**, 289–313, doi: 10.3986/ac.v44i3.2996.

Klimchouk, A. B., 2007, Hypogene speleogenesis: Hydrogeological and morphogenetic perspective: National Cave and Karst Research, Special paper no 1 I.

Klimchouk, A. B., 2009b, Principal characteristics of hypogene speleogenesis, in K. W. Stafford, L. Land, and G. Veni, eds., Advances in hypogene karst studies: NCKRI, 1, 1–11.

Kumbalek, M., 2015, Analysis of paleokarst sinkholes in the Arkoma Basin using 3-D seismic: M.S. thesis, University of Arkansas.

Kupecz, J. A., and L. S. Land, 1991, Late-stage dolomitization of the Lower Ordovician Ellenburger Group, west Texas: Journal of Sedimentary Petrology, **61**, 551–574, doi: 10.1306/D426775D-2B26-11D7-8648000102C1865D.

Liner, C. L., 2016, Elements of 3D seismology, 3rd ed.: SEG.

Lomando, A. J., P. M. Harris, and D. E. Orlopp, 1993, Casablanca Field, Tarragona Basin, offshore Spain: A karsted carbonate reservoir, in R. D. Fritz, J. L. Wilson, and D. A. Yurewicz, eds., Paleokarst related hydrocarbon reservoirs: SEPM Core Workshop no. 18, 201–225.

Loucks, R. G., 1999, Paleocave carbonate reservoirs: Origins burial-depth modifications, spatial complexity, and reservoir implications: AAPG Bulletin, **83**, 1795–1834, doi: 10.1306/E4FD426F-1732-11D7-8645000102C1865D.

Mairs, T. M., 1966, A subsurface study of the Fernvale and Viola Formations in the Oklahoma portion of the Arkoma Basin: Tulsa Geological Society Digest, **32**, 60–81.

McDonnell, A., R. G. Loucks, and T. Dooley, 2007, Quantifying the origin and geometry of circular sag structures in northern Fort Worth Basin, Texas: Paleocave collapse, pull-apart fault systems, or hydrothermal alteration?: AAPG Bulletin, 91, 1295–1318, doi: 10.1306/05170706086.

Milad, B., and R. Slatt, 2017, Integrated 3D seismic and core data for characterization of natural fractures of the Hunton Limestone and the Woodford Shale in Central Oklahoma: AAPG Search and Discovery Article #51382.

Moser, D., 2016, 3D seismic interpretation of paleokarst sinkholes, Boone Limestone, Lower Mississippian: Subsurface eastern Arkoma Basin, Conway County, Arkansas: M.S. thesis, University of Arkansas.

Palmer, A. N., 1991, Origin of limestone caves: GSA Bulletin, 103, 1–21, doi: 10.1130/0016-7606(1991)103<0001:OAMOLC>2.3.CO;2.

Palmer, A. N., 2007, Cave geology: Cave Books.

Palmer, A. N., and M. V. Palmer, 2011, Paleokarst of the USA: A brief review, in E. L. Kuniansky, ed., U.S. Geological Survey Karst Interest Group Proceedings, U.S. Geological Survey Scientific Investigations Report 2011–5031, 7–16.

Perry, W. J., 1994, Arkoma Basin Province _062_, in D. L. Gautier, G. L. Dolton, K. I. Takahashi, and K. L. Varnes, eds., 1995 National Assessment of United States oil and gas resources — Results, methodology, and supporting data: U.S. Geological Survey, Digital Data Series 30, CD–ROM.

Perry, W. J., 1997, Structural settings of deep natural gas accumulations in the conterminous United States, Chapter D, in T. S. Dyman, D. D. Rice, and W. A. Westcott, eds., Geologic controls of deep natural gas resources in the United States: U.S. Geological Survey Bulletin 2146-D, 41–46.

Qi, J., B. Zhang, H. Zhou, and K. Marfurt, 2014, Attribute expression of fault-controlled karst — Fort Worth Basin, Texas: A tutorial: Interpretation, 2, no. 3, SF91–SF110, doi: 10.1190/INT-2013-0188.1.

Romero, A. M., and R. P. Philp, 2012, Organic geochemistry of the Woodford shale, southeastern Oklahoma: How variable can shales be?: AAPG Bulletin, **96**, 493–517, doi: 10.1306/08101110194.

Story, C., P. Peng, C. Heubeck, C. Sullivan, and J. D. Lin, 2000, Liuhua 11-1 Field, South China Sea: A shallow carbonate reservoir developed using ultrahigh-resolution 3-D seismic, inversion, and attribute-based reservoir modeling: The Leading Edge, **19**, 834–844, doi: 10.1190/1.1438721.

Strimple, H. L., andW.W. Nassichuk, 1965, Correlation notes on the upper Wapanucka Limestone of southeastern Oklahoma: Oklahoma Geology Notes, 25, 287–293.

Sullivan, C. E., K. J. Marfurt, A. Lacazette, and M. Ammerman, 2006, Application of new seismic attributes to collapse chimneys in the Fort Worth Basin: Geophysics, **71**, no. 4, B111–B119, doi: 10.1190/1.2216189.

Sun, Q., J. Cartwright, S. Wu, and D. Chen, 2013, 3D seismic interpretation of dissolution pipes in the South China Sea: Genesis by subsurface, fluid induced collapse: Marine Geology, 337, 171–181, doi: 10.1016/j.margeo.2013.03.002.

Suneson, H. S., 2012, Arkoma Basin petroleum — Past, present and future: The Shale Shaker Digest, **63**, 38–70.

Sykes, M., 1997b, Paleokarst characteristics of the surface and subsurface in the Viola Limestone (Ordovician), Arbuckle Mountains, Oklahoma: The Shale Shaker, **37**, 107–121.

Sykes, M., J. Puckette, A. Abdalla, and Z. Al-Shaieb, 1997a, Karst development in the Viola Limestone in southern Oklahoma, in K. S. Johnson, ed., Simpson and Viola Groups in the southern Midcontinent, 1994 Symposium, Oklahoma Geological Survey Circular 99, 66–75.

Waltham, A. C., 2005, Tiankengs of the world, outside China: Cave and Karst Science, **32**, 67–74.

Waltham, A. C., and P. G. Fookes, 2003, Engineering classification of karst ground condition: Journal of Engineering Geology and Hydrogeology, **36**, 101–118, doi:10.1144/1470-9236/2002-33.

Waltham, T., F. Bell, and M. Culshaw, 2005, Sinkholes and subsidence: Karst and cavernous rocks in engineering and construction: Springer-Praxis Publishing.

Wengerd, S. A., 1948, Fernvale and Viola Limestones of south central Oklahoma: AAPG Bulletin, 32, 2183–2253, doi: 10.1306/3D933C89-16B1-11D7-8645000102C1865D.

Wright, P., 2016, Hypogene Palaeokarst and burial corrosion, http://www.force.org/Global/Seminars/2016/20160419.-21.%20Siliciclastic%20and%20carbonate%20sedimentology/Presentasjoner/Paul%20Wright%20-%20Hypogene%20Palaeokarst%20and%20Burial%20Corrosion.pdf, accessed 7 August 2017.

Wright, P., and P. Harris, 2013, Carbonate dissolution and porosity development in the burial (mesogenetic) environment: AAPG Search and Discovery Article #50860.

Zeng, H., R. Loucks, X. Janson, G. Wang, Y. Xia, B. Yuan, and L. Xu, 2011b, Three-dimensional seismic geomorphology and analysis of the Ordovician paleokarst drainage system in the central Tabei Uplift, northern Tarim Basin, western China: AAPG Bulletin, **95**, 2061–2083, doi: 10 .1306/03111110136.

Zeng, H., G. Wang, X. Janson, R. Loucks, Y. Xia, L. Xu, and B. Yuan, 2011a, Characterizing seismic bright spots in deeply buried, Ordovician paleokarst strata, Central Taibei Uplift, Tarim Basin, western China: Geophysics, **76**, no. 4, B127–B137, doi: 10.1190/1.3581199.

Zhao, W., A. Shen, Z. Qiao, J. Zeng, and X. Wang, 2014, Carbonate karst reservoirs of the Tarim Basin, northwest China: Types, features, origins, and implications for hydrocarbon exploration: Interpretation, **2**, no. 3, SF65–SF90, doi: 10.1190/INT-2013-0177.1.

Appendix

Gassmann's Equation

We computed Gassmann's equation in python to visually fit acoustic impedance and total porosity observed in wireline logs from well B. The python function is

```
def Gassmann(km,mum,rhom,kf,rhof,phi,a,b,c):
    rhosat = rhom*(1-phi) + phi*rhof
    kdry = km / (a + b*np.power(phi,c))
    mudry = mum / (a + b*np.power(phi,c))
    musat = mudry
    q = (kf*(km-kdry))/(phi*(km-kf))
    ksat = km * (kdry + q)/(km + q)
    vp = np.sqrt((ksat + 4*musat/3)/rhosat)
    vs = np.sqrt(musat/rhosat)
    rho = rhosat
    return (vp, vs, rho)
```

where km is the mineral bulk modulus, mum is the mineral shear modulus, rhom is the mineral density, kf is the pore fluid bulk modulus, rhof is the pore fluid density, phi is the porosity, kdry is the dry rock bulk modulus, mudry is the dry rock shear modulus, and (a, b, c) relate the dry rock moduli to mineral moduli and act as free parameters of the theory to fit real data (Liner, 2016), and the saturated rock has bulk modulus ksat, shear modulus musat, and density rhosat. Bulk modulus and density for brine at 100% saturation were computed using Batzle and Wang (1992) using a salinity of 0.2 ppm (Viola) and 0.12 ppm (Wapanucka) estimated from Harrison and Routh (1981).The NumPy numerical library is assumed to have been imported as

np such that np.sqrt() is the NumPy square root function, etc. Parameters (a, b, c) were adjusted to fit the observed wireline data of acoustic impedance and total porosity for the Viola and Wapanucka interval. Our results indicate that the best fit parameters for the Viola are (a, b, c) = (1.2, 0.9, 0.9) and for the Wapanucka are (a, b, c) = (1.1, 0.9, 0.8).

Figures

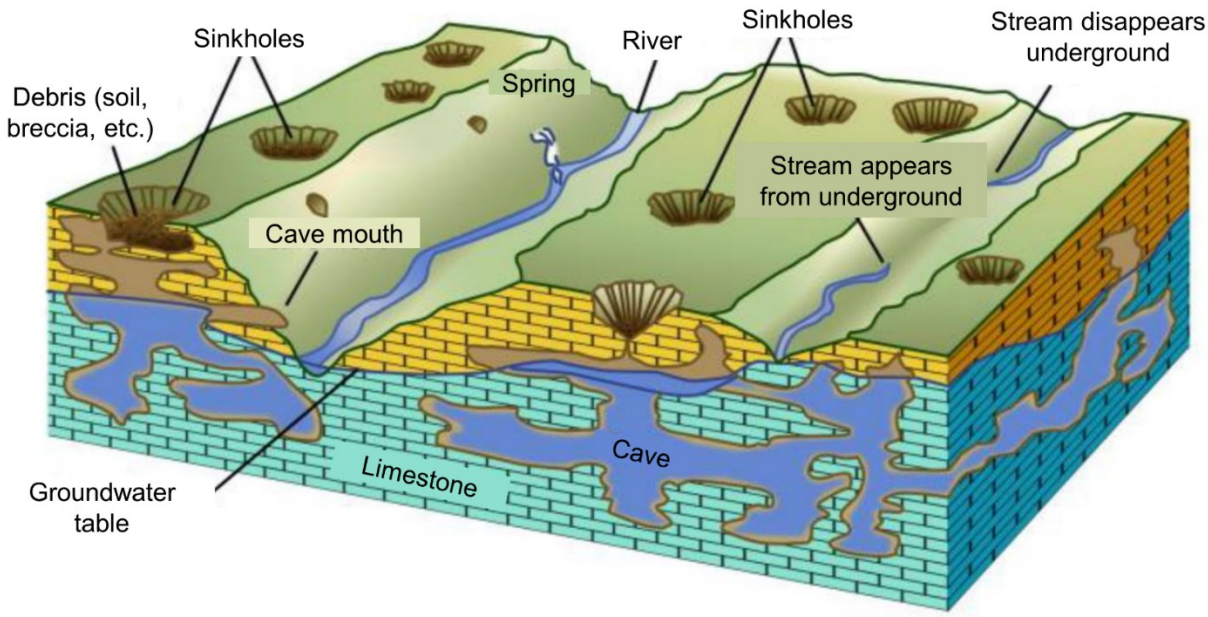

Figure 3.1. Generalized karst model showing incised valleys, collapsed caves and sinkholes (modified from Grotzinger and Jordan, 2010).

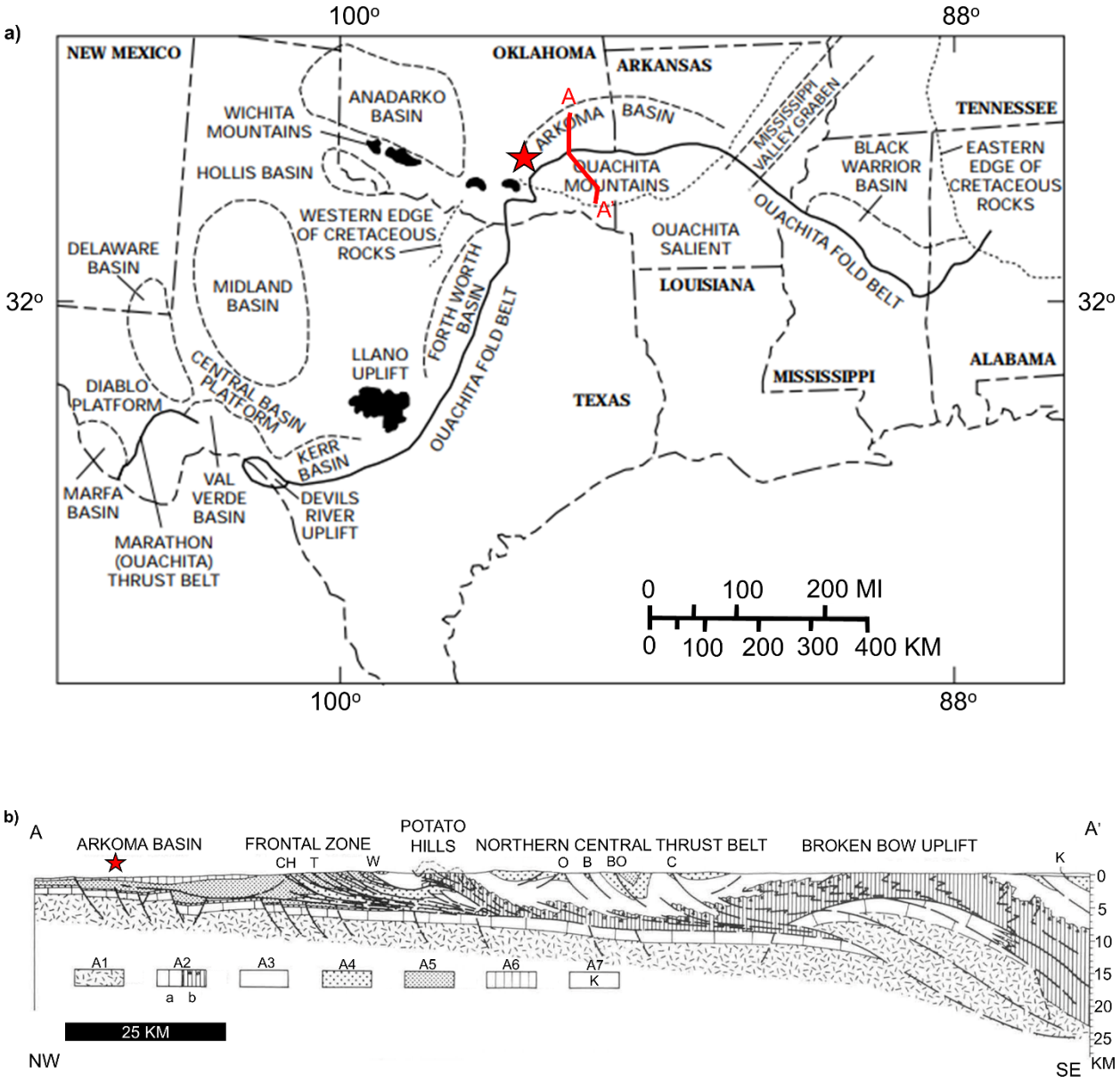

Figure 3.2. (a) Regional geology. The study area is in the red star in relation to the Arkoma Basin in Oklahoma and adjacent basins along the Ouachita fold belt in the southern mid-continent (modified from Perry, 1997) (b) Generalized cross section across the Arkoma basin and frontal Ouachita system in Oklahoma. A1 = Precambrian basement, A2a =Cambrian through Mississippian platform rocks, A2b = Cambrian through Early Mississippian deep water rocks (pre-orogenic), triangles represent Ordovician to Devonian cherts, A3 = Mississippian flysch, A4 = Morrowan flysch and platform rocks, A5 = Atoka Formation, A6 = Desmoinesian, A7 = Cretaceous, CH = Choctaw fault, T = Ti Valley fault, W = Windingstair fault, O = Octavia fault, B = Boktukola fault, BO = Big One fault, C = Cloudy fault. (Modified after Arbenz, 1989).

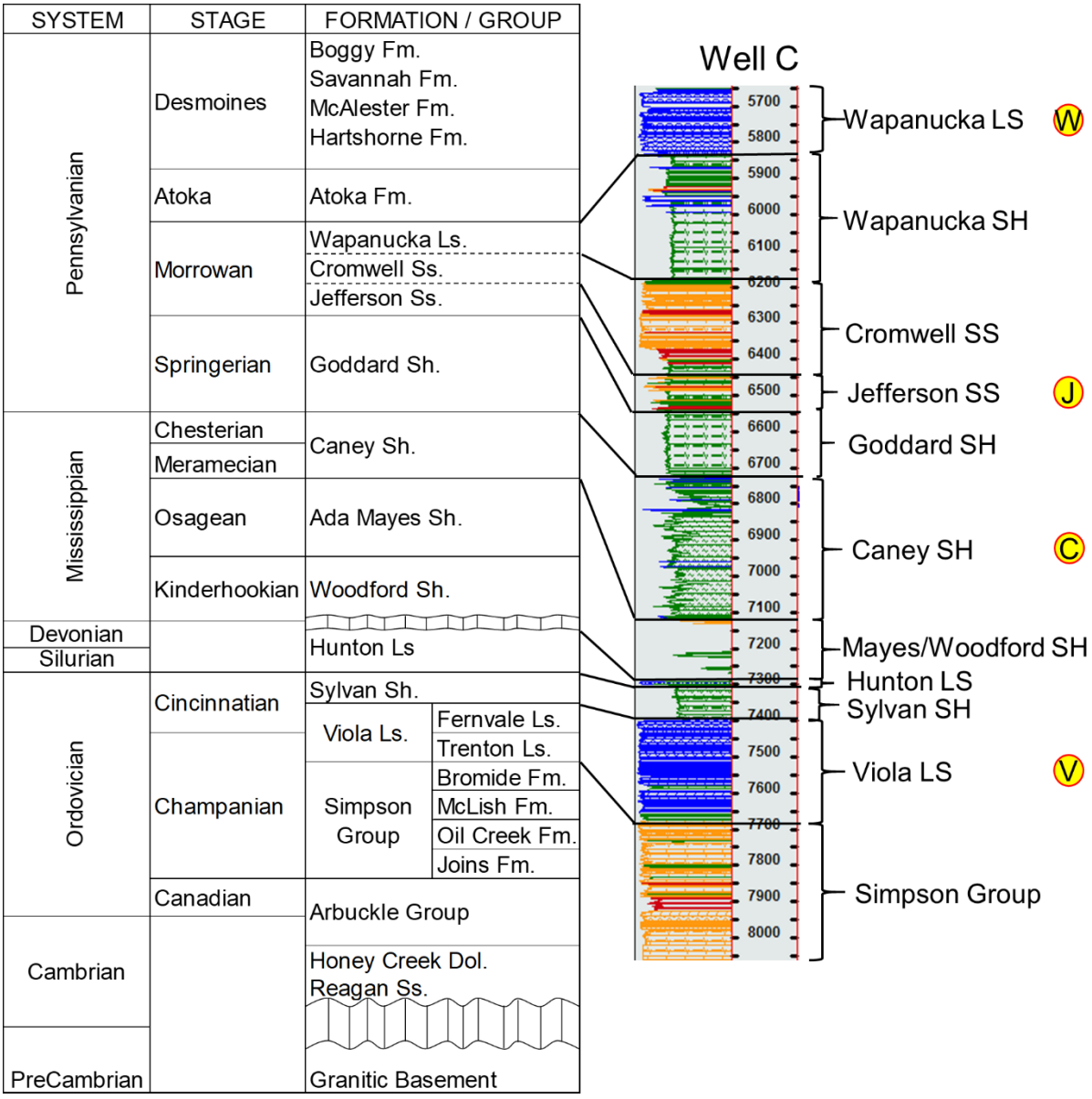

Figure 3.3. Stratigraphy of Well C relative to the geology of the western Arkoma Basin. Circles V, C, J and W represent interpreted horizons on seismic. (Stratigraphic column modified after Bliefnick (1992); Romero and Philp, (2009)), (Well C log, modified after Fronterra Integrated Geosciences LLC, 2004).

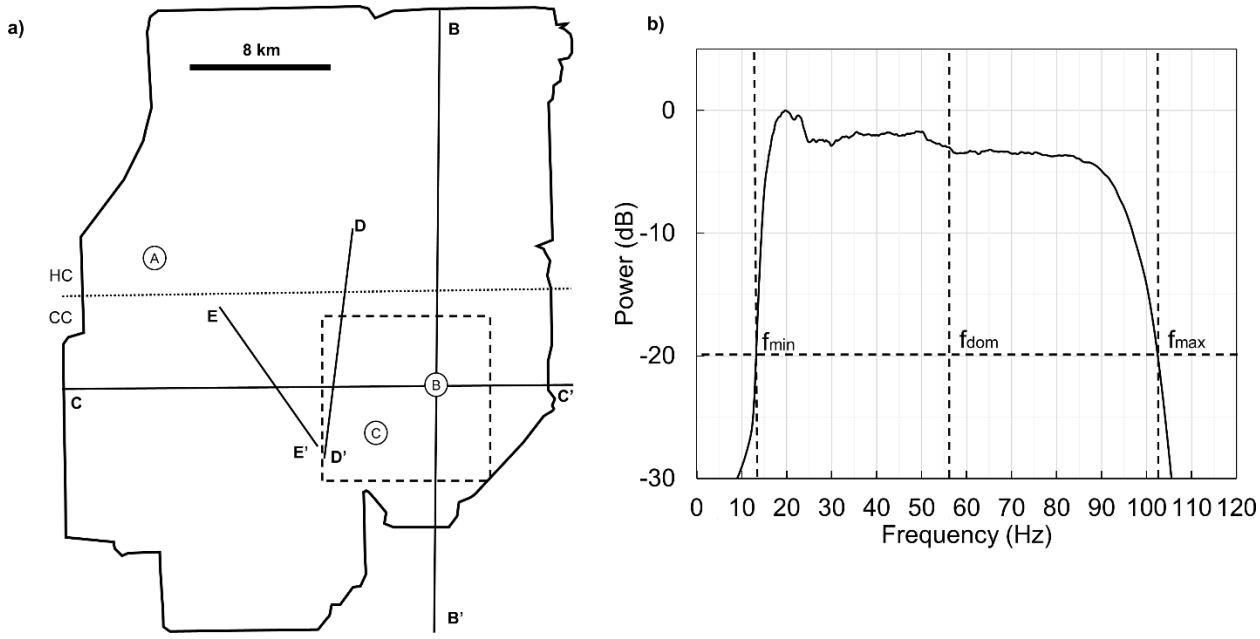

Figure 3.4. (a) Map of 3D seismic coverage with an area of about 180 sq. mi (~470 sq. Km). Circles A, B, C are well locations. Dashed box detail area about 54 sq. km (21. sq. mi.) used for variance parameter test. County line between Hughes County (HC) and Coal County (CC) is shown dotted. Cross sections lines AA' to DD' are referenced in later figures, and (b) Frequency spectrum of entire survey. Minimum frequency (fmin) is 13Hz, dominant frequency (fdom) is 57.5Hz, and maximum frequency (fmax) is 102.5Hz.

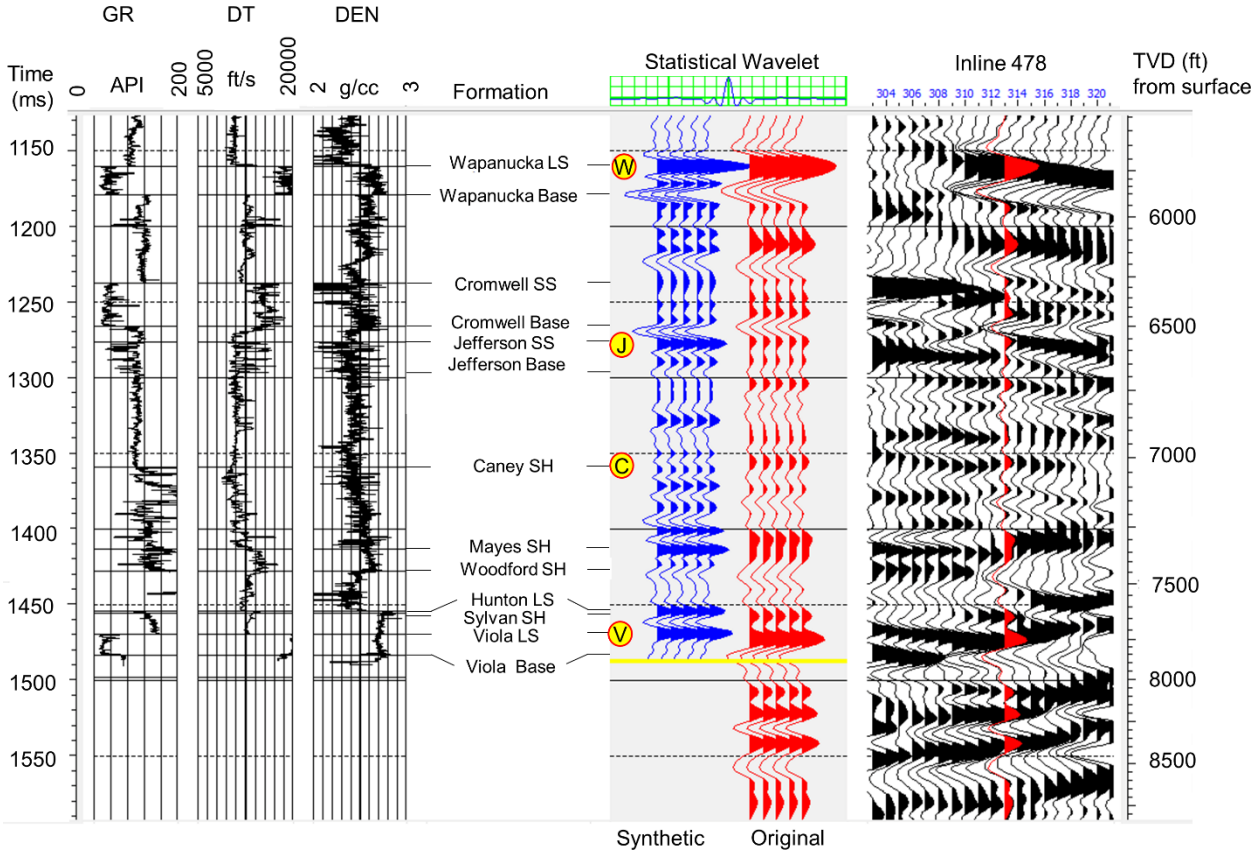

Figure 3.5. Well B synthetic seismogram showing gamma ray (GR), P-wave sonic (DT), density (DEN), formation tops, tracked horizons in circles, synthetic (blue) and field data (red), and overlay on section of 3D seismic data.

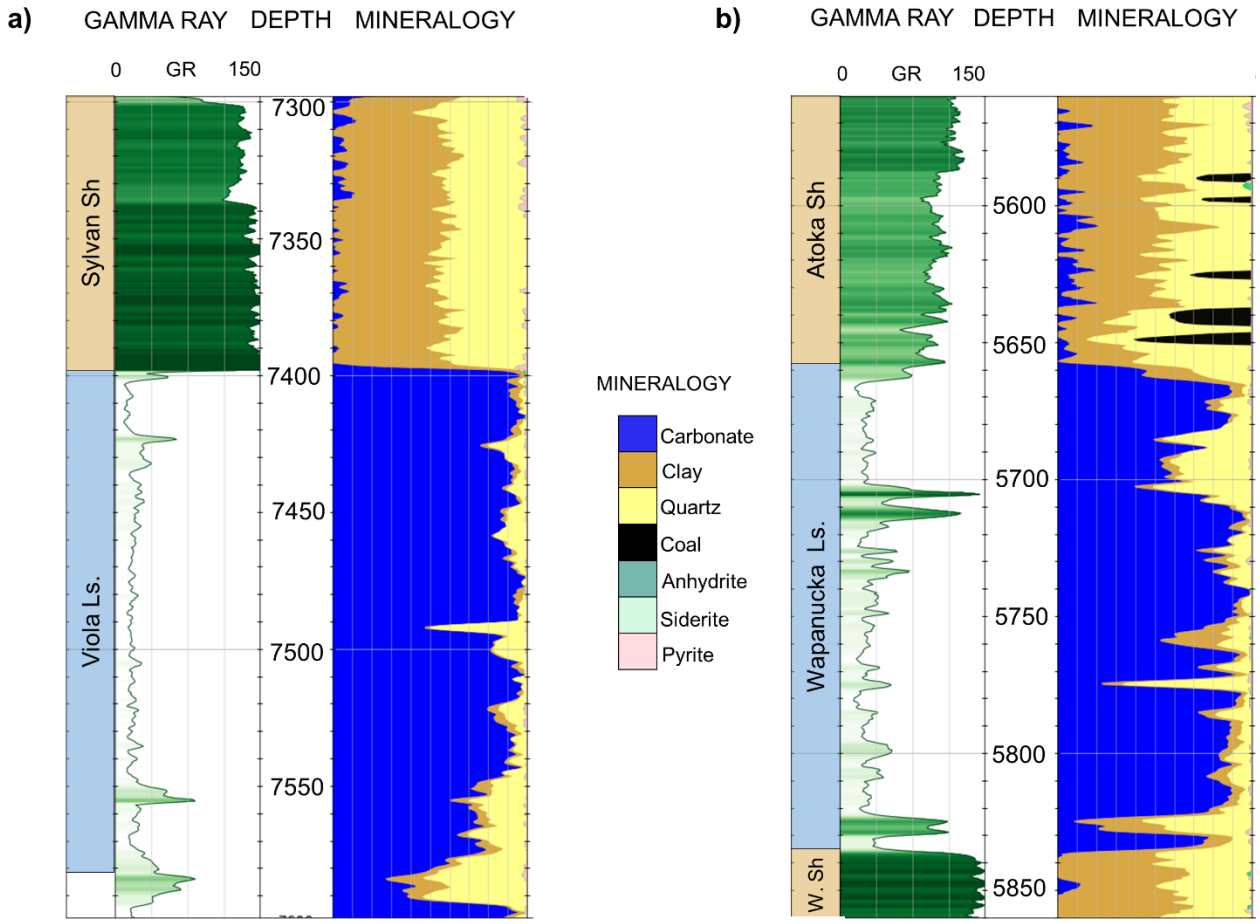

Figure 3.6. Well C wireline log plots of gamma ray and mineralogy over a 300 ft (91 m) interval including the (a) Viola Limestone, and (b) Wapanucka Limestone. Note higher carbonate content fraction in Viola compared to the Wapanucka.

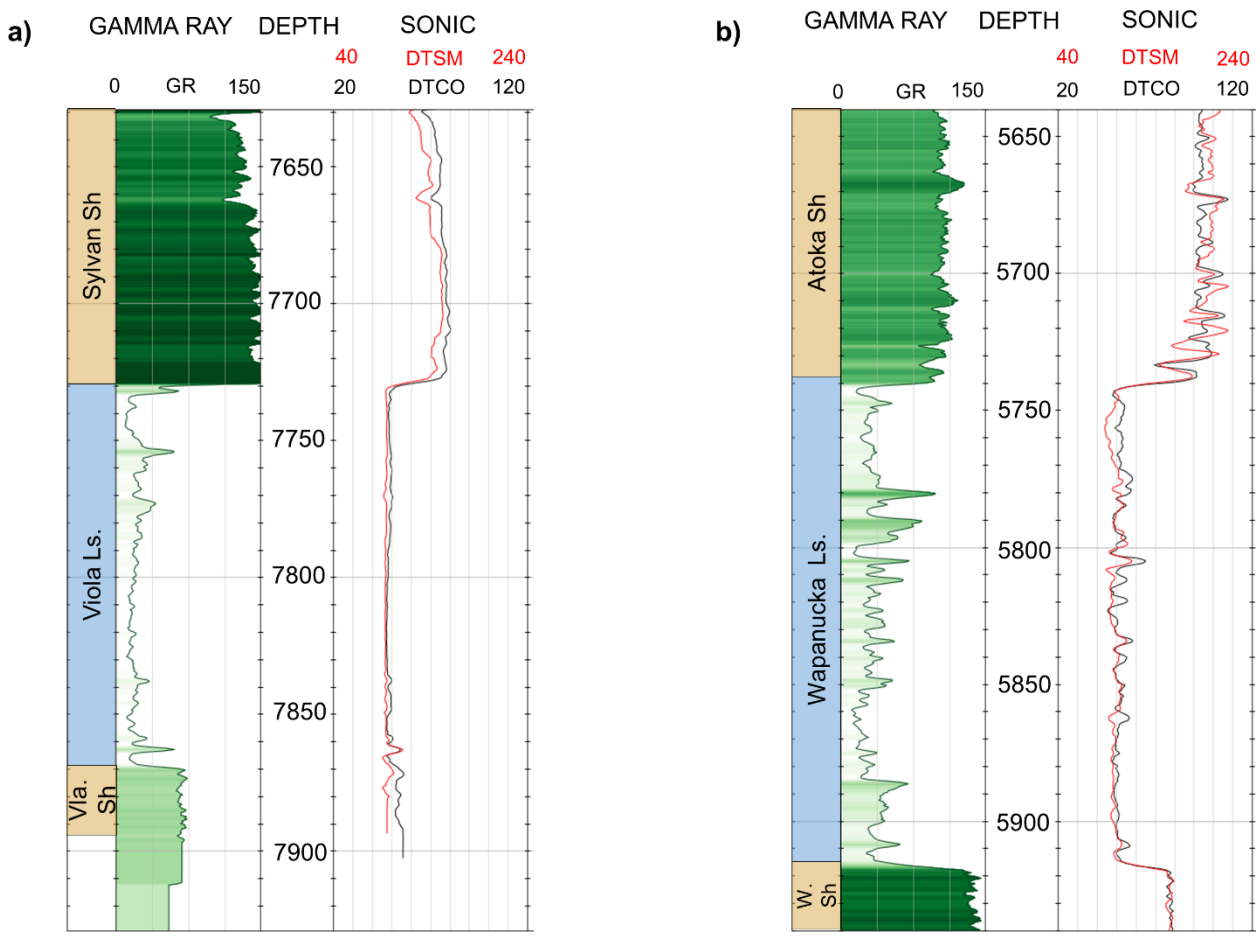

Figure 3.7. Log plots of Well B over a 300 ft (91 m) interval showing GR, gamma ray (API), DTSM and DTCO, S-wave and P-wave sonic (us/ft) (a) Viola Limestone, and (b) Wapanucka Limestone.

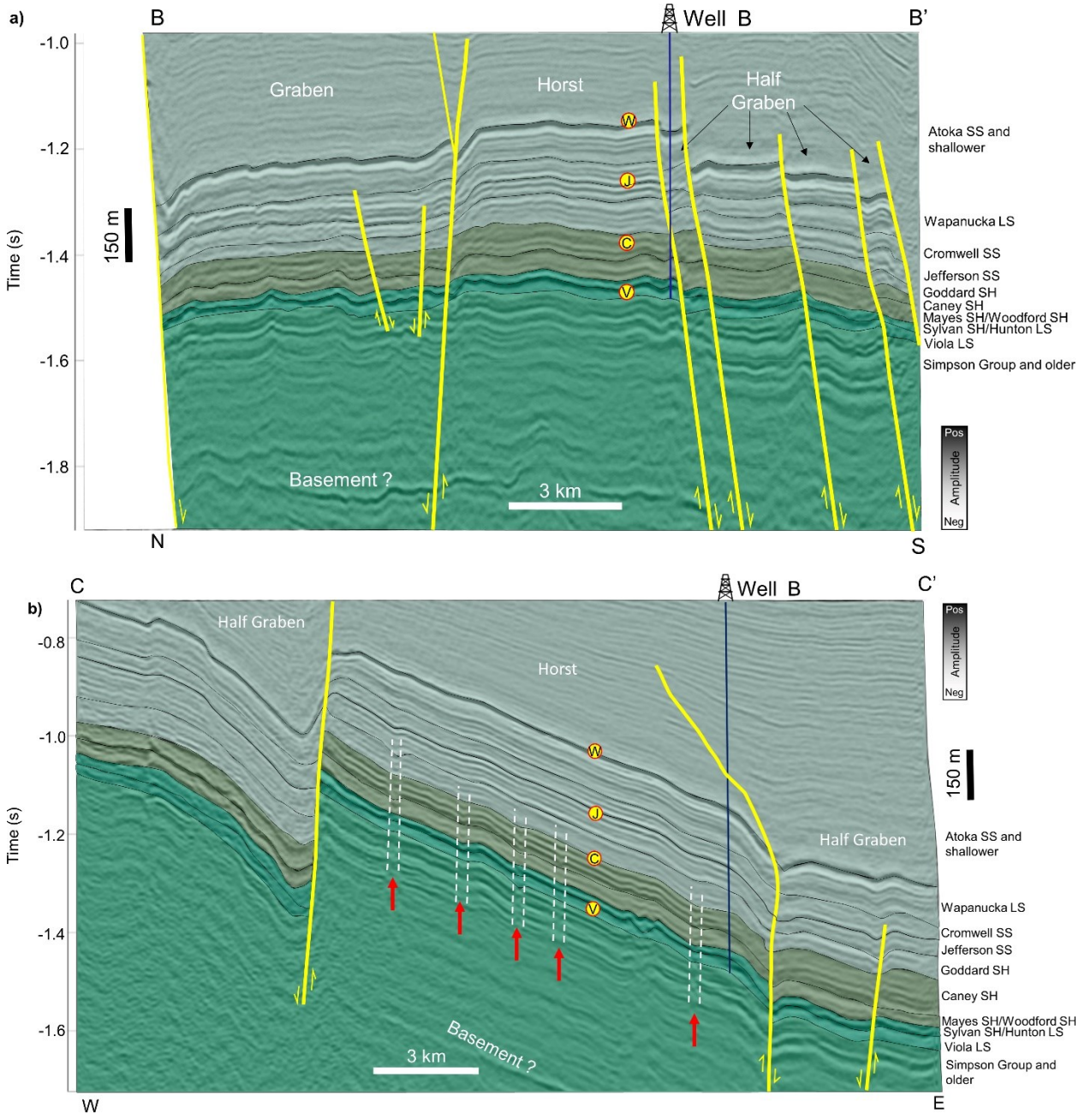

Figure 3.8. Geoseismic sections through Well B. Yellow lines are faults. Broken white lines show vertical collapse features (pipes) associated with sinkholes. Red arrows indicate vertical collapse features emanating from the Simpson Group and older. Circles V, C, J and W represent Viola Limestone, Caney Shale, Jefferson Sandstone and Wapanucka Limestone respectively. The circles are interpreted horizons. (a) Line BB' geoseismic dip section and (b) Line CC' geoseismic strike section. See Figure 3a for the location of Line BB' and Line CC'. SH = Shale, LS = Limestone, SS = Sandstone.

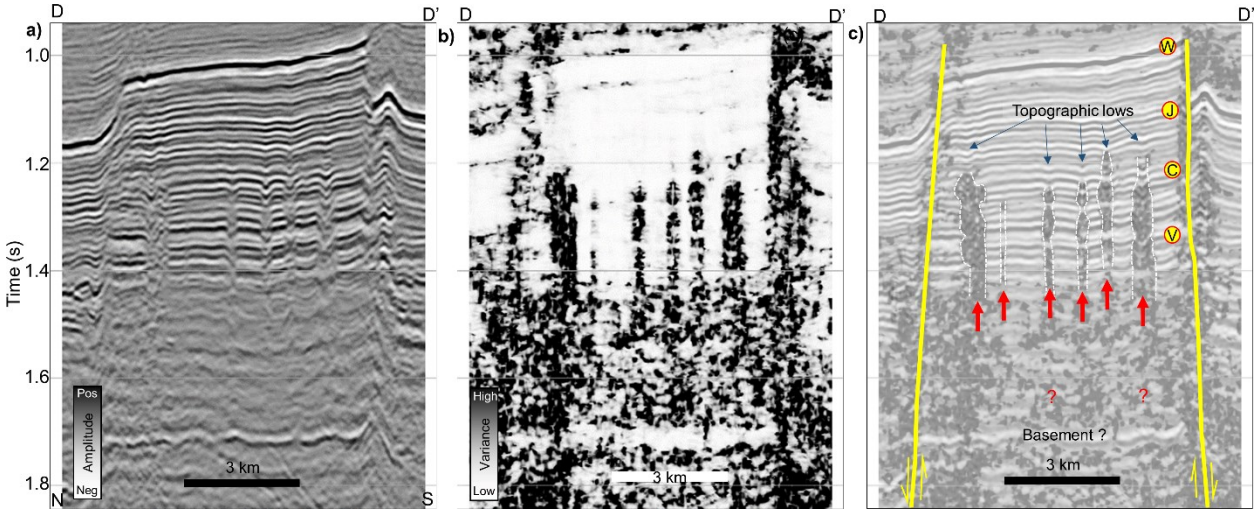

Figure 3.9. Line DD' across sinkholes showing sags and pipes. (a) Uninterpreted amplitude section, (b) Uninterpreted variance section, and (c) Co-rendered amplitude and variance showing major faults in yellow and collapse pipes in dashed white lines indicated by red arrows. Circles V, C, J, and W represent Viola Limestone, Caney Shale, Jefferson Sandstone, and Wapanucka Limestone, respectively. Internal configuration within the pipes show high variance relative to outside the pipes. Note pipe features vary in size and vertical extent. See Figure 3a for the location of Line DD'.

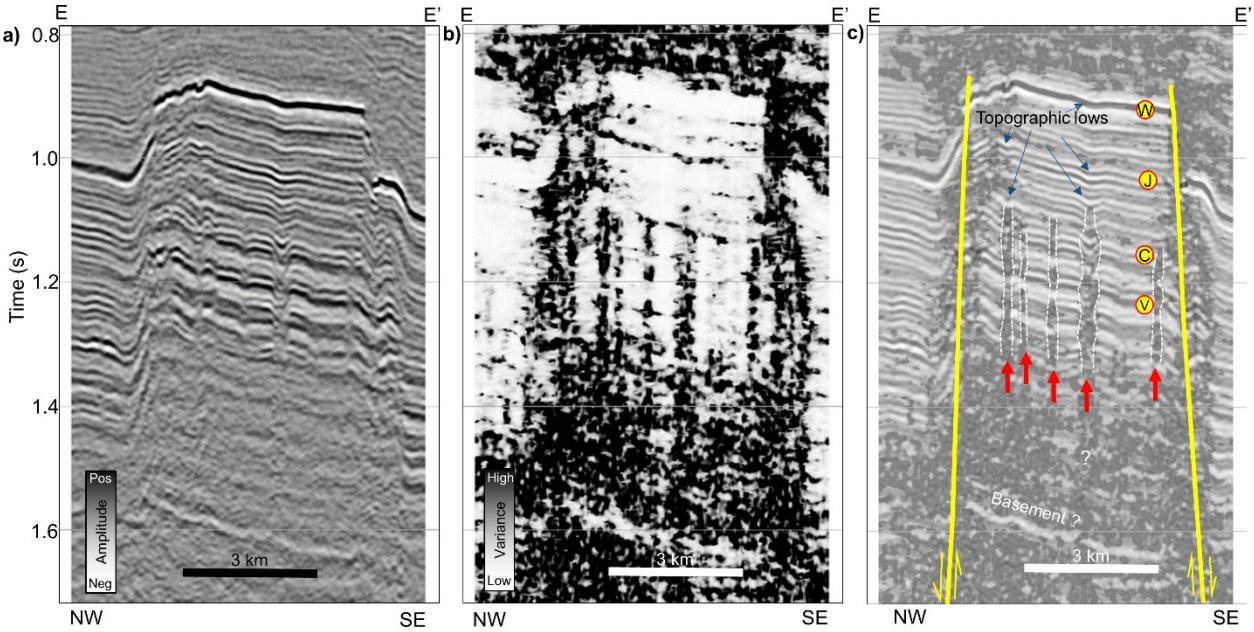

Figure 3.10. Line EE' across sinkholes showing sags and pipes (a) Uninterpreted amplitude section (b) Uninterpreted variance section, and (c) Co-rendered amplitude and variance section showing major faults in yellow. Dashed white lines show extent of collapse pipes. Internal configuration within the pipes show high variance relative to outside the pipes. Note how the pipes differ from each other in terms of size and extent. Circles V, C, J, and W represent Viola Limestone, Caney Shale, Jefferson Sandstone, and Wapanucka Limestone, respectively. See Figure 3.3a for location of Line EE'.

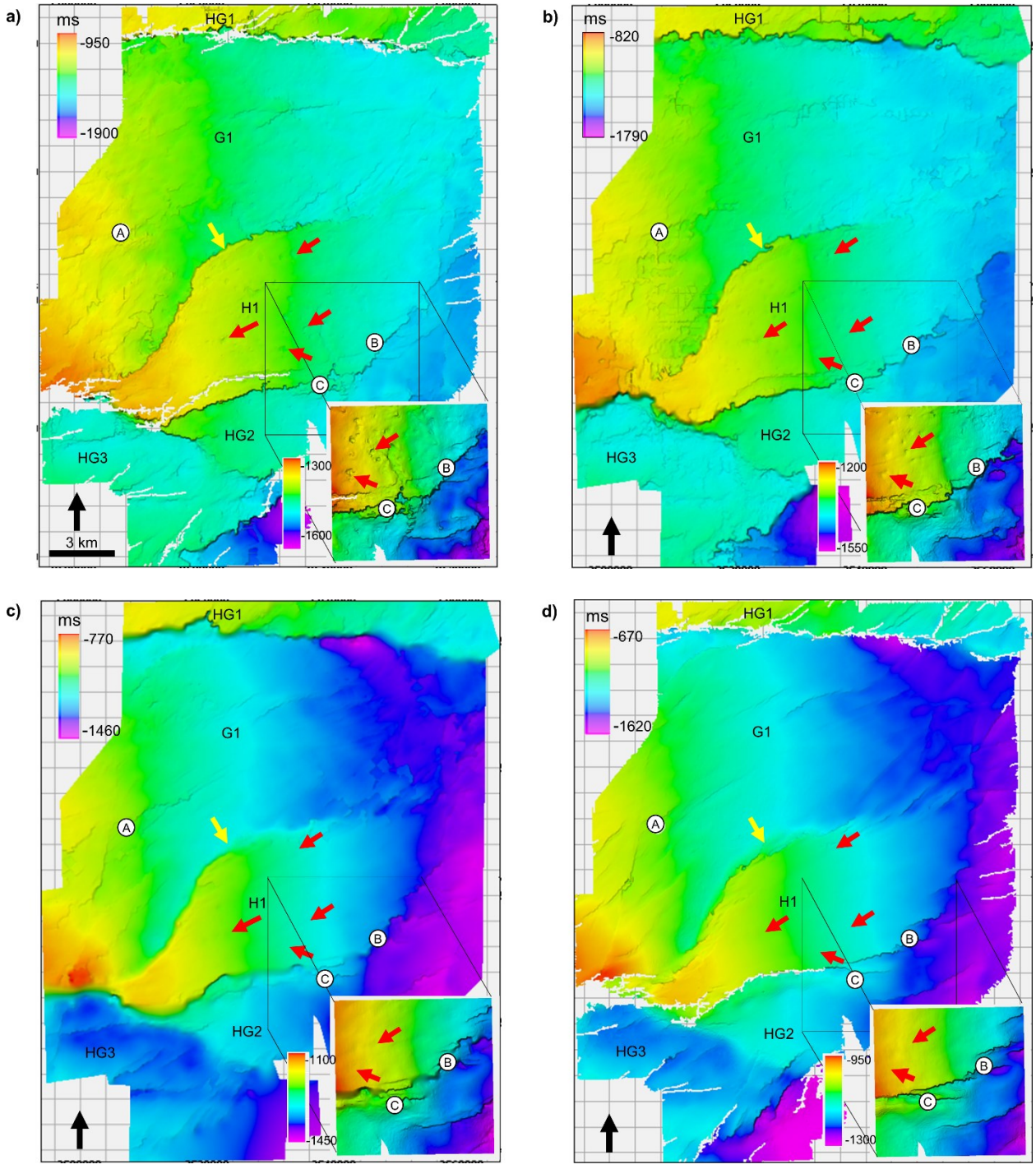

Figure 3.11. Horizon time structure maps showing half-grabens (HG1, HG2, HG3), full graben (G1), and horst (H1). Yellow arrow indicates a major fault and red arrows are selected sinkholes. (a) Viola Limestone (b) Caney Shale (c) Jefferson Sandstone and, (d) Wapanucka Limestone.

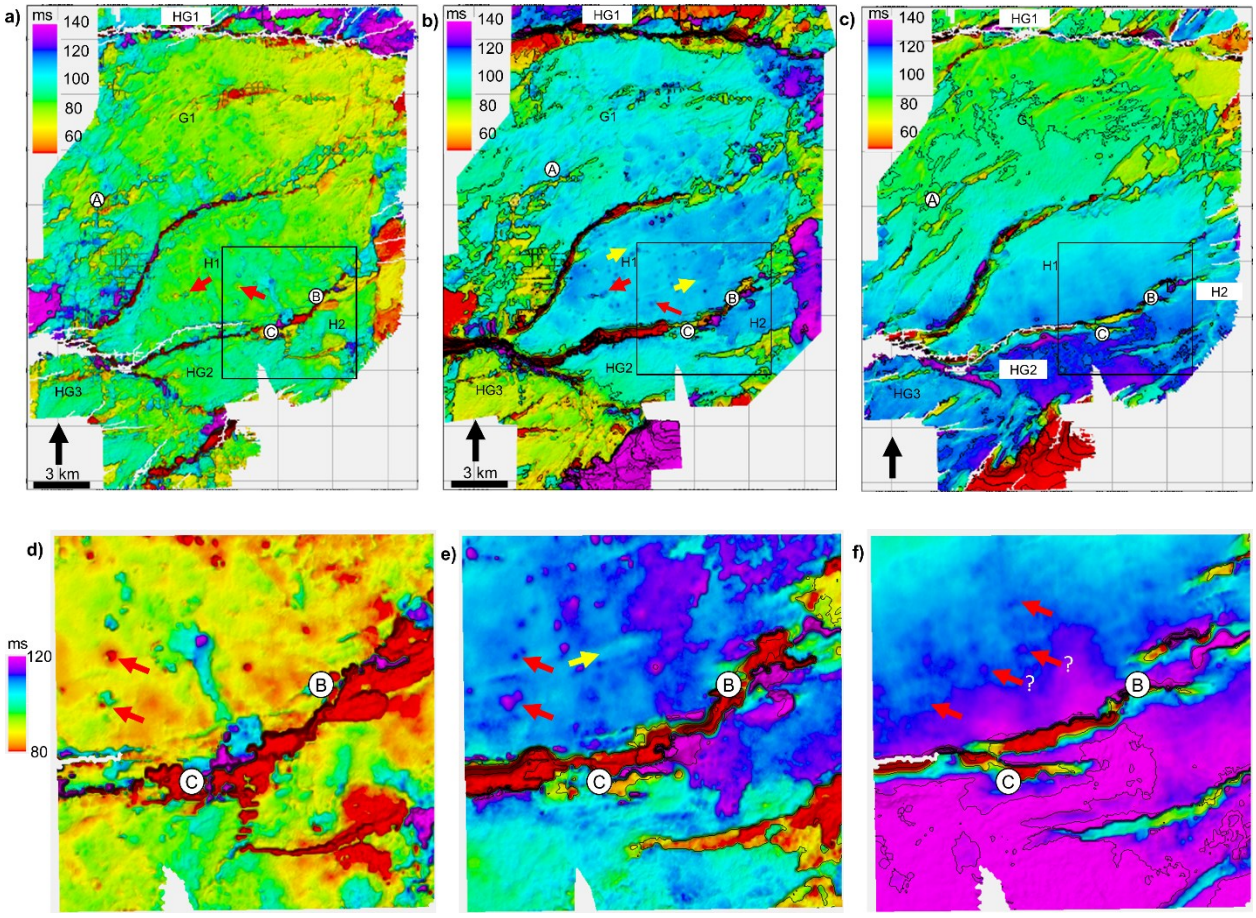

Figure 3.12. Isochron maps. (a) Viola Limestone to Caney Shale (VC), (b) Caney Shale to Jefferson Sandstone (CJ), and (c) Jefferson Sandstone to Wapanucka Limestone (JW). Red arrows signify sinkholes. Yellow arrows show lineaments N70ºE on H1 not visible on Figures 11a and 11b. Isochron maps showing inset maps in a, b and c (d) VC (e) CJ and (f) JW.

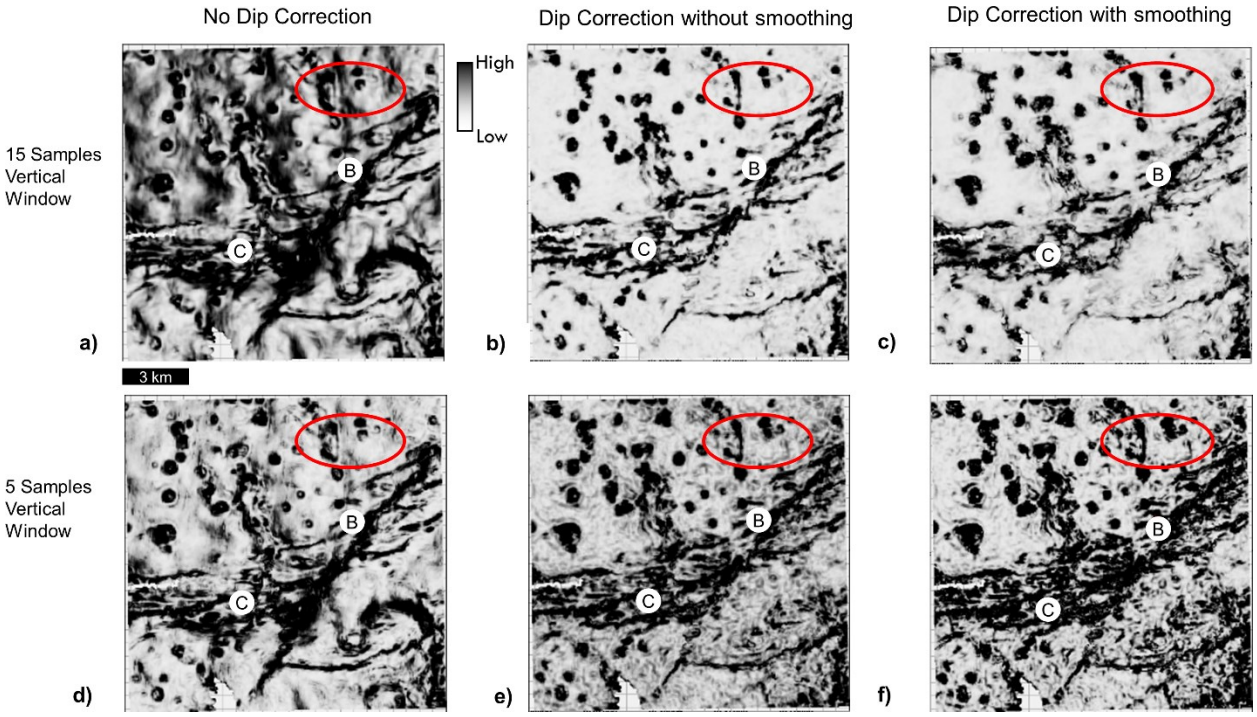

Figure 3.13. Variance parameter test for the Viola event. Top row images used 15 sample vertical smoothing, and bottom used 5 sample vertical smoothing. (a, d) Variance calculated horizontally (no dip correction) (b, e) Variance calculated along a dipping plane (dip correction) without dip guided smoothing and (c, f) Dip correction with orthogonal smoothing operator (dip guided smoothing). Based on visibility and resolution of paleokarst features in the red oval, the optimum variance parameter choice for the Viola horizon was judged to be variance c (vertical window 15, dip correction, dip-guided smoothing).

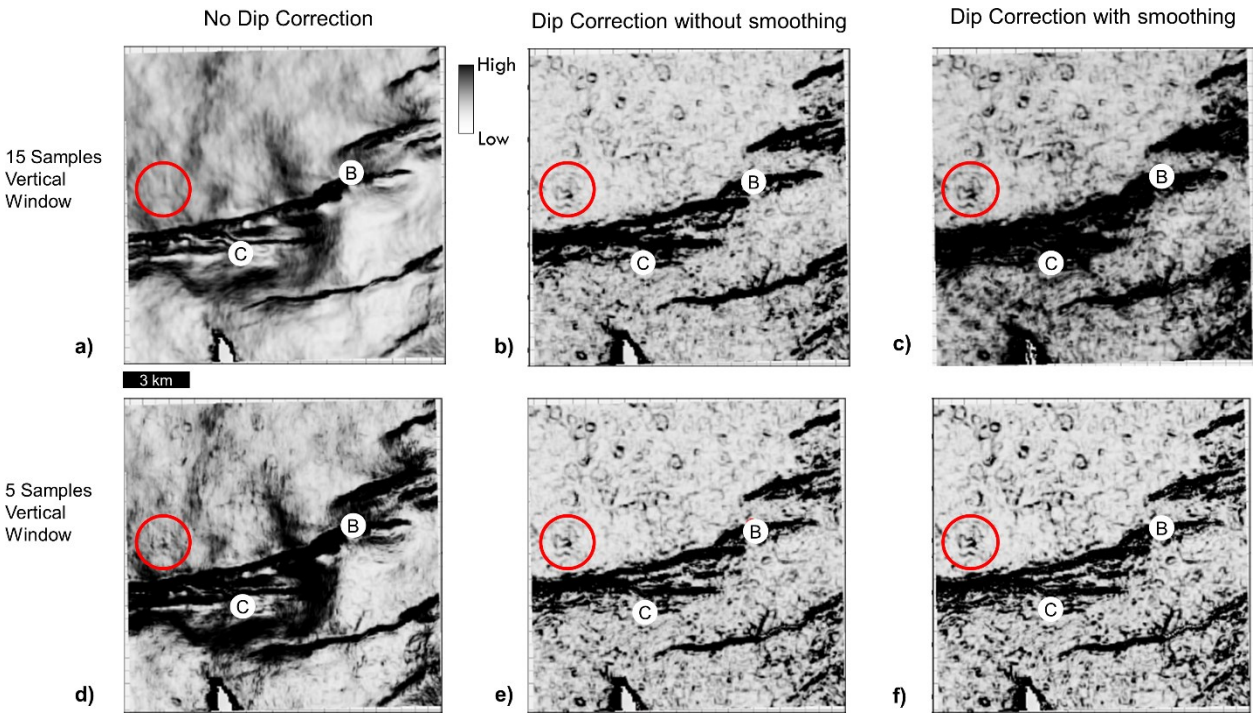

Figure 3.14. Variance parameter test for the Wapanucka event using same parameter matrix as Figure 12. Based on visibility and resolution of paleokarst features in the red circle, the optimum variance parameter choice for the Wapanucka horizon was judged to be variance f (vertical window 5, dip correction, dip-guided smoothing).

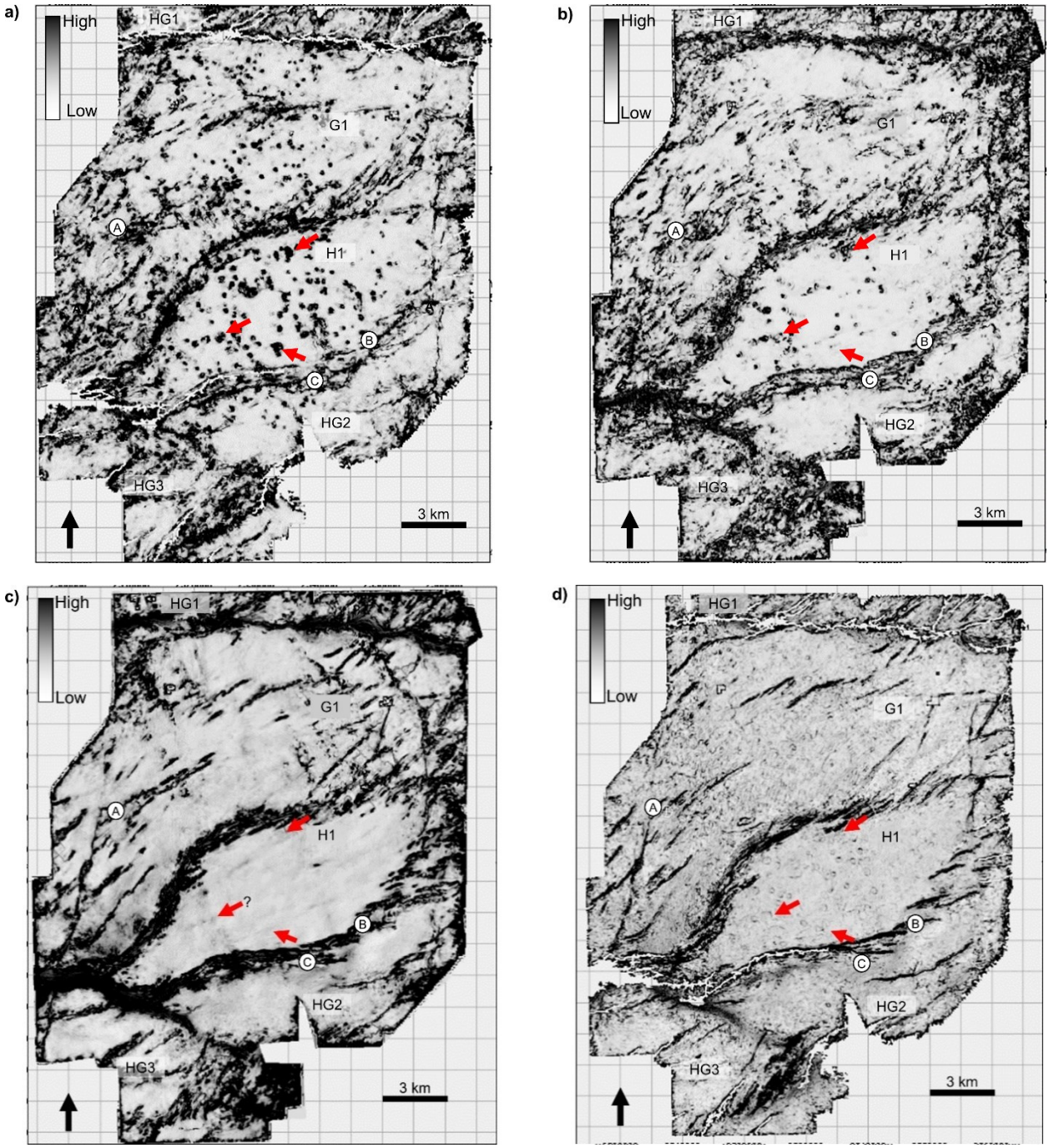

Figure 3.15. Horizon variance attribute maps. (a) Viola Limestone horizon showing mature paleokarst landscape and strong sinkhole signatures. Red arrows point to selected sinkholes. (b) Caney Shale horizon with sinkhole red arrows at same locations as shown on Viola. Being insoluble shale, this formation cannot undergo true paleokarst development. However, many sinkhole-type features are observed coincident with sinkholes in the deeper Viola, likely representing infill and compaction of Viola sinkholes, (c) Jefferson Sandstone horizon with sinkhole red arrows at same locations as shown on Viola. No sinkhole indication is observed, and (d) Wapanucka Limestone horizon with sinkhole red arrows at same locations as shown on Viola. Subtle sinkhole indications exist in the variance attribute and many of these features are

coincident with much deeper Viola sinkholes, perhaps indicating the sinkholes act as conduits for later migration of hydrothermal fluids.

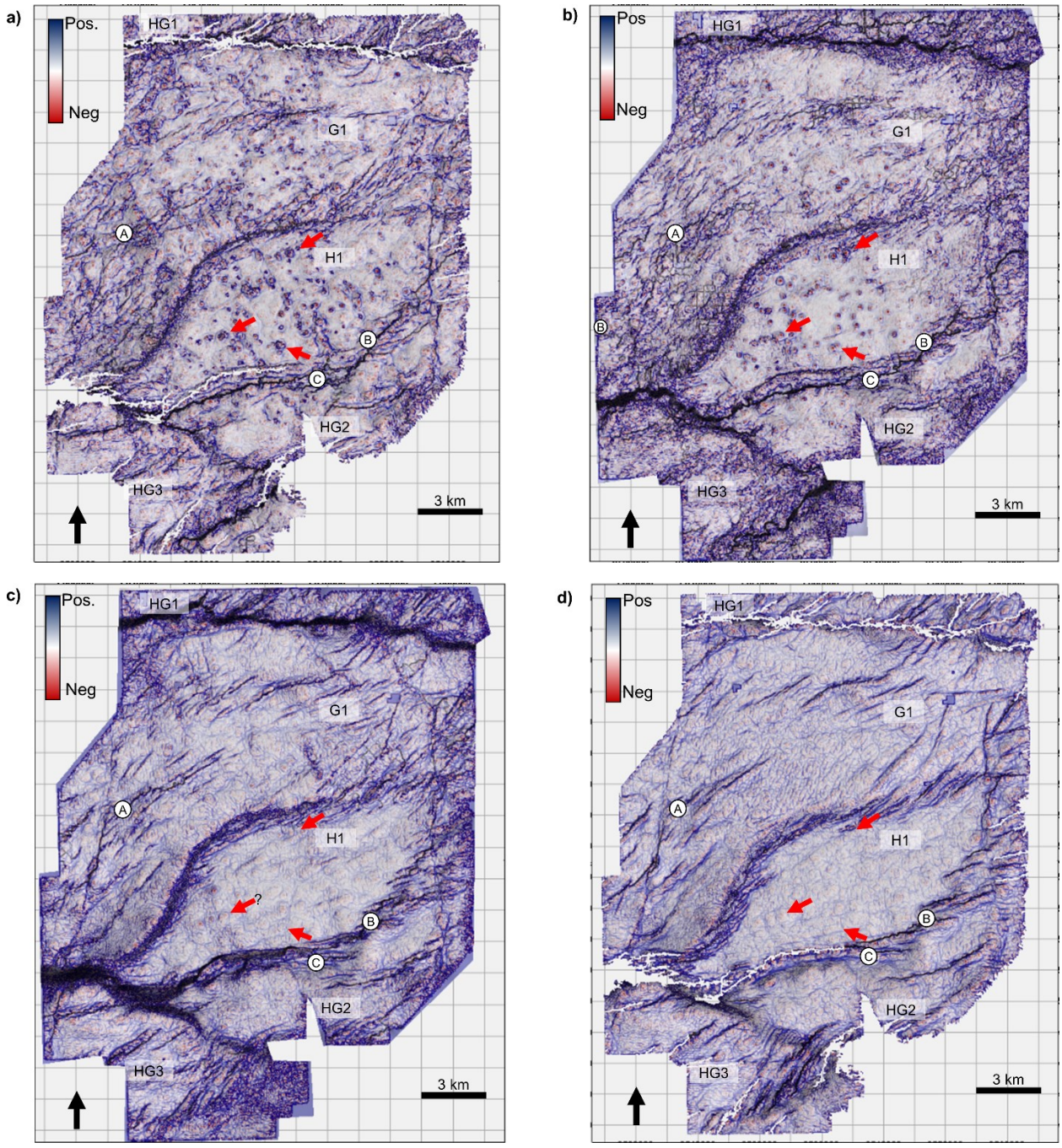

Figure 3.16. Horizon slices through most positive curvature (zero transparency) co-rendered with most negative curvature (20% transparency). Red arrows are coincident with those in Figure 15 (a) Viola Limestone, (b) Caney Shale, (c) Jefferson Sandstone, and (d) Wapanucka Limestone.

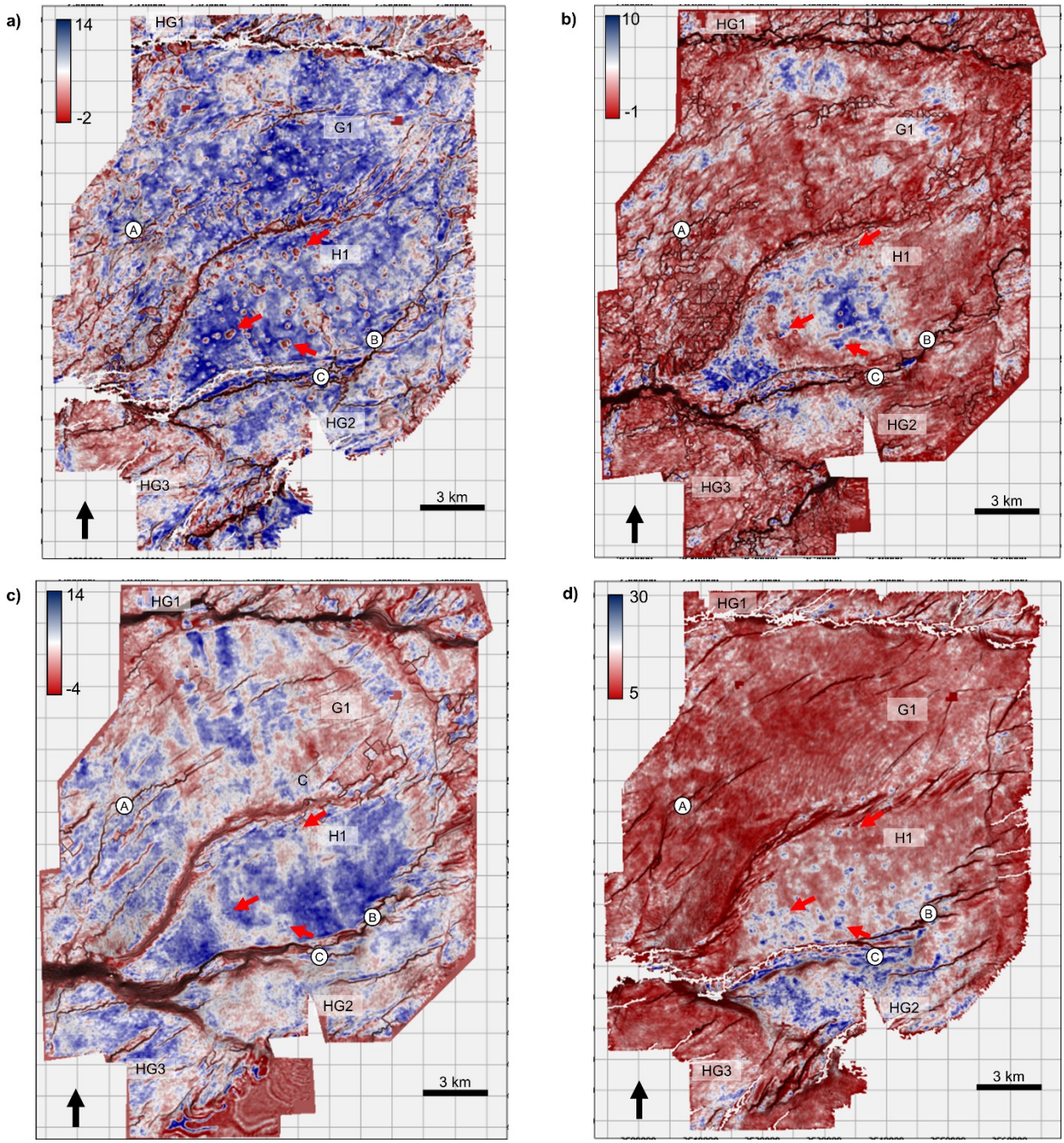

Figure 3.17. Horizon amplitude maps (a) Viola Limestone, (b) Caney Shale, (c) Jefferson Sandstone, and (d) Wapanucka Limestone.

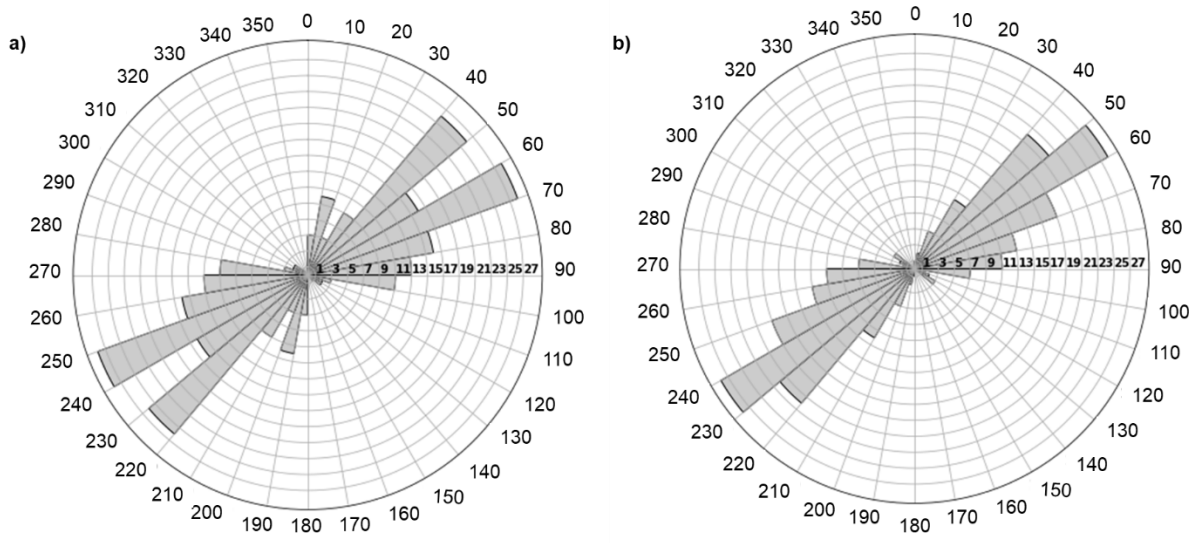

Figure 3.18. Rose diagrams lineaments and faults. (a) Viola Limestone, showing principal azimuth directions are 40-50^{o} and 60-70^{o} respectively, and (b) Wapanucka Limestone, with principal azimuth of 60-70^{o}.

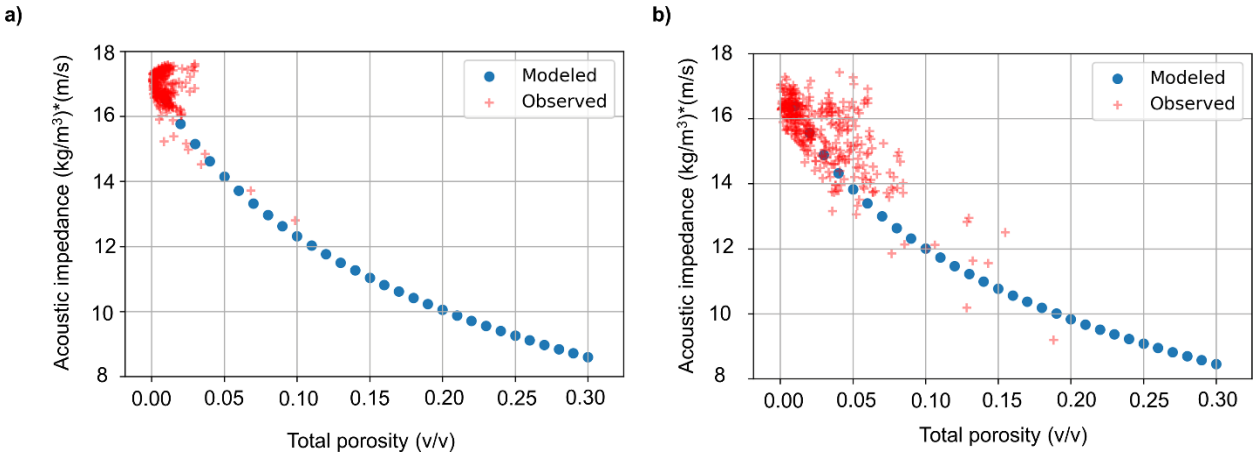

Figure 3.19. Gassmann model calibrated on Well B wireline log data. Total porosity is defined as the root-mean-square of neutron and density porosity. (a) Viola Limestone, and (b) Wapanucka Limestone.

Tables

Table 3.1. Formation tops, thicknesses and total depth for Wells A, B, and C. All depths are measured depth.

		Well A (ft)			Well B (ft)			Well C (ft)		
Lithology		**Top**	**Base**	**Thickness**	**Top**	**Base**	**Thickness**	**Top**	**Base**	**Thickness**
Hartshorne Coal		N/A			3079	N/A	N/A	N/A		
Atoka Sh					3200	N/A	N/A			
Wapanucka Ls		4511	4616	105	5740	5918	178	5660	5835	175
Cromwell Ss		4854	5016	162	6290	6510	220	6180	6289	109
Jefferson Ss		5071	5182	111	6575	6702	127	6449	6543	94
Goddard /Penn Caney Sh		5182	5488	306	6702	7048	346	6543	6719	176
Caney Sh		5488	5710	222	7048	7352	304	6719	7020	301
Mayes Sh		5710	5806	96	7352	7462	110	7007	7120	113
Woodford Sh.		5806	N/A	N/A	7462	7630	168	7120	7292	172
Hunton Ls		N/A			7630	7636	6	7292	7300	8
Sylvan Sh					7636	7729	93	7300	7398	98
Viola Ls					7729	7870	141	7398	7583	185
Simpson Group	Simpson Dol.				N/A			7592	7675	83
	1st Bromide Ss							7676	7887	211
	Upper Tulip Creek Ss							7736	7887	151
	Lower Creek Ss.							7887	8008	121
	McLish Formation							8008	8075	67
	TD (ft)	5850			7931			8103		
	KB (ft)	710			692			643		

Table 3.2. Well B rock properties and related quantities for estimation of reflection coefficient and acoustic impedance in sinkhole areas.

	Measured from Well B						Estimated	
Lithology	**Acoustic Velocity (m/s)**	**Density (kg/m3)**	**Acoustic Impedance (SI)**	**Reflection Coefficient Outside**	**Amplitude Inside Sinkhole**	**Amplitude Outside Sinkhole**	**Acoustic Impedance Inside Sinkhole (SI)**	**Reflection Coefficient Inside Sinkhole**
Sylvan Shale	4016	2748	11.04					
Viola	6224	2712	16.88	0.21	2.03	7.79	12.31	0.05
Atoka Shale	3251	2258	7.35					
Wapanucka	5872	2653	15.59	0.36	11.39	18.65	28.21	0.59

CHAPTER 4

Mississippian Chat and Tripolite Zones in Osage County, Oklahoma: Paleokarst Interpretation Based on 3D Seismic and Well Logs

Olanrewaju Aboaba[1] and Christopher Liner[1], University of Arkansas, Department of Geosciences

This paper was submitted to AAPG/SEG journal Interpretation in 2020 and under revision

Abstract

Mississippian paleokarst Chat and tripolitic chert (tripolite) zones associated with the Miss Lime have been hydrocarbon exploration targets in Osage County for many decades. Chat is residual chert, either in place or transported, weathered out of chert-bearing Mississippian Limestone that was eroded at the Mississippian-Pennsylvanian unconformity (MPU). Thus, formation of Chat is an epigene paleokarst process. Previous studies have reported that some Chat cores contain dioptase and dickite, high-temperature minerals implying hydrothermal alterations, indicating a late episode of hydrothermal activity. Tripolite occurs as a highly porous, silica-rich interval within the Miss Lime. It is formed by in-place alteration of limestone by silica-rich surface waters or deep-seated hydrothermal fluids, making tripolite formation a mixed or hypogene paleokarst process. Here, we distinguish Chat and tripolite by seismic analysis calibrated by well control with full-wave sonic log data. Chat and tripolite show clear separation on log-based acoustic impedance, but no separation with V_P/V_S and both exhibit total porosities greater than 20% with evidence of fracture porosity. Sonic-based normal incidence wedge models for Chat bounded above by Pennsylvanian Shale and below by Miss Lime indicate two seismic expressions are plausible: first, a strong negative amplitude when Chat thickness is above tuning and, second, a weak or absent amplitude associated with small impedance contrast

between Chat and overlying Penn shale. Our analysis suggests that both the traditional Chat 'strong response' and a new 'dim-out' exploration strategy may be usefully applied in Osage County. Tripolite response is consistently a negative amplitude event that strengthens with increasing tripolite thickness. This study provides an interpretive framework for characterizing Chat and tripolite zones associated with the Mississippian Lime in the US Midcontinent, which may be applicable to regions around the world.

Introduction

Non-biogenic chert reservoirs can either be formed in the near surface as an epigene paleokarst process or at depth by a hypogene paleokarst process through alteration of carbonates by deep hydrothermal silica-rich fluids (Rogers and Longman, 2001). Conditions that influence the formation of chert reservoirs include depth to the water table, a silica source, shaliness, brecciation, weathering, temperature, and hydrocarbon emplacement (Rogers and Longman, 2001).

In the US midcontinent, "Chat" is an informal name for high-porosity Mississippian chert reservoirs (Watney et al. 2001). Chat is a residual product formed by weathering of chert-bearing limestone and either deposited by in-situ brecciation or as transported breccia (Parham and NorthCutt, 1993; Montgomery et al., (1998); McGilvery Pers. Comm. 2020). Chat reservoirs in Osage County, Oklahoma that formed by epigene processes are associated with the Mississippian-Pennsylvanian Unconformity (MPU) (Montgomery et al. 1998).

Tripolite is a distinct chert reservoir facies that has been diagenetically altered and linked to the migration of hydrothermal fluids or paleowater decalcification (Manger, 2014; McGilvery Pers. Comm. 2020). It occurs at a variable depth below the Chat (Mikkelson, 1966; Rogers, 2001; Snyder, 2016; Liner, 2018) and is internal to the upper Miss Lime. Liner (2018) studied

twenty shallow wells that cut a full section of Mississippian (Boone) Limestone to find tripolite occurring at depths of 6-69 m (20-255ft) below top of the Boone, with a maximum frequency of occurrence at 46 m (150 ft). Figure 4.1 (left image) shows a schematic diagram to illustrate the distinction between Chat and tripolite in Osage County.

Chat reservoirs are challenging to characterize because of their intricate diagenetic history, varied depositional source and diverse pore networks (Montgomery et al., 1998). A good understanding of the influence of porosity and heterogeneity is critical for exploration and management of these reservoirs (Elebiju et al., 2011). Rogers et al. (1995) noted that fractures are not critical for Chat production. However, Montgomery et al. (1998) noted that fractures, vugs and spicule molds enhance reservoir quality and promote high production rates. Chat reservoirs are produced not only from fractures, but other pore space types (Rogers and Longman, 2001). MPU Chat breccias exhibit fracture porosity associated with concurrent or later Pennsylvanian tectonic movement, vuggy solution porosity formed by subaerial weathering (Zajic, 1956), and are typically characterized by low resistivities with high porosities ranging from 30-50% for good reservoirs (Rogers, et al., 1995; Montgomery et al., 1998; Watney et al., 2001). Low resistivities are attributed to wet and non-productive zones based on petrophysical evaluation (Rogers, 2001). Chat wells can be very productive in the southern midcontinent with daily production rates up to 40 million cubic ft of gas and 1500 bbl of oil (Montgomery et al., 1998). Cumulative Chat production in Oklahoma is over 105 million bbl of oil and 1 TCF of gas (Rogers, 2001). Watney et al. (2001) noted that tripolitic chert has greater production potential and economic viability than Chat reservoirs.

Thomasson et al. (1989) identified productive Chat formations on seismic data as irregular thick low-porosity pods surrounded by dense Mississippian Limestone, with uncommon

acoustic properties relative to adjacent formations. Yenugu et al. (2010), Matos et al. (2011) and Roy et al. (2013) used self-organizing maps of gray level co-occurrence matrix attributes to characterize chert reservoirs. Elebiju et al. (2011) used volumetric seismic attributes to delineate faulting and karst features such as sinkholes and cockpit karst in Mississippian chert and Ordovician Arbuckle reservoirs. Dowdell et al. (2012, 2013) used coherence, curvature, impedance inversion calibrated to well logs to delineate zones with high porosity and density, indicative of chert. Guo et al (2014) used vector correlation and curvature attribute to characterize Mississippian tripolitic chert. Jennings (2014) subdivided the Miss Lime into seven zones based on elastic properties estimated from dipole sonic and density logs, with no internal tripolite development occurring in the wells he studied. Benson (2014) mapped and quantified seismic bright spots attributing them to occurrence of tripolitic chert. Liner (2018) quantified the stratigraphic position of tripolite in the Boone Limestone from well logs.

In this study we clarify Chat and tripolite zones associated with the Miss Lime in Osage County, Oklahoma using an ensemble of analytical techniques applied to digital well logs and poststack seismic data to understand the seismic response and its relationship to geology and rock properties. We correlate Chat and tripolite on well logs to determine their lateral and vertical continuity. We generated a compressional velocity (V_P) / shear velocity (V_S) versus acoustic impedance plot, modified after Odergaard and Avseth (2004), acoustic impedance versus total porosity plot, and histograms of V_P, V_S, density, and acoustic impedance. Wedge models and fracture porosities were computed. Chat X-ray fluorescence data were analyzed. Chat and tripolite reflections were mapped on seismic data, and attributes extracted for amplitude, acoustic impedance, and porosity to delineate favorable regions for Chat and tripolite development. This study provides a context for distinguishing and delineating Chat and tripolite zones associated

with the Mississippian Lime in the US Midcontinent, which may be applicable to global carbonate provinces.

Geology of Osage County

The study area is in Osage County, northeastern Oklahoma, lies to the west of the Ozark uplift and east of the Nemaha ridge. Surface and subsurface Paleozoic strata have a gentle westerly dip and are composed of sandstone, shale, limestone, and dolomite (Thorman and Hibpshman, 1979). Paleozoic rocks in the area overlie Precambrian igneous basement (Liner, 2015). Four cycles of marine transgression and regression have been recorded in the Paleozoic separated by unconformities representing periods of non-deposition and erosion (Thorman and Hibpshman, 1979). These unconformities record hundreds of thousands to millions of years of exposure between depositional cycles.

The first cycle designated the Absaroka began in the Cambrian - Lower Ordovician, with an inundation of marine seas in the Cambrian. The formations overlying the basement include the granite wash and the Reagan Sandstone (Thorman and Hibpshman, 1979). The Arbuckle Group overlies the Reagan Sandstone, completely covering Precambrian rocks in the Lower Ordovician. This followed an erosional phase exposing Precambrian rocks (Thorman and Hibpshman, 1979). The Arbuckle Group thickness is 305-610 m (1000-2000 ft) on the Cherokee Platform, thickening to approximately 2133 m (7000 ft) southward in the Arbuckle Mountains (Johnson, 2008). It consists primarily of limestone and dolomite with locally developed cherty oolitic beds (Bass, 1942). The top and base of the Arbuckle are characterized by major unconformities, as well as six internal unconformities recognized (Reeder, 1976). In the study area, an oil-bearing interval is sometimes developed between 2-15 m (5-50 ft) from the top of the Arbuckle Group in a zone consisting of cherty dolomite which was

weathered during or after the Ordovician (Bass, 1942). Large volumes of water are associated with Arbuckle oil production. Karst sinkholes, collapse features, and lineaments with associated increase in porosity and permeability are present in the upper Arbuckle Group. These enhanced reservoir properties are attributed to focused weathering and erosion (Elebiju et al., 2011). Evidence of paleokarst has been found in outcrop studies in the Arbuckle Mountains of southern Oklahoma, and south of the Ozark uplift in northeast Oklahoma (Fritz et al., 2013; Milad et al., 2017; Milad and Slatt, 2018).

The second cycle designated the Tippecanoe, occurred in the Middle Ordovician – Lower Devonian intervals, which deposited the Simpson Group that is subdivided into three units (oldest to youngest): Burgen Sand, Tyner Formation, and the Wilcox Sand. These units correspond to subtle pulses of Simpson sea level change through the area. Upper Ordovician, Silurian, and Lower Devonian units have been removed by erosion (Thorman and Hibpshman, 1979).

The third cycle is Middle Devonian – Mississippian, designated the Kaskaskia, with transgression that reworked the Simpson sands to create the Misener Sandstone of Middle to Late Devonian age (Thorman and Hibpshman, 1979). The Woodford Shale was deposited in the Late Devonian to Early Mississippian, overlying the Misener, where it is present, or the Arbuckle Group where the Misener is absent (Thorman and Hibpshman, 1979). The Woodford Shale is less than 2 m (5 ft) thick in the study area, and less than 15 m (50 ft) thick throughout Osage County (Thorman and Hibpshman, 1979). The informal “Miss Lime” name designates thick Mississippian limestones in the subsurface of northern Oklahoma (Johnson, 2008) of lower Mississippian age overlying the Woodford Shale. The Miss Lime comprises limestone, cherty limestone, and chert (Bass, 1942) as well as dolomitic limestone (Thorman and Hibpshman,

1979; Milad et al. (2020)). The Miss Lime is found throughout Osage County (Bass, 1942), and reaches a thickness approximately 122 m (400 ft) (Bass, 1942; Thorman and Hibpshman, 1979). The top boundary of the lime is an erosional surface comprising mainly weathered chert (Bass 1942; Thorman and Hibpshman, 1979). As a result, the Miss Lime and the overlying Chat interval is approximately 100 m (330 ft) in thickness across the study area. The thickness of the early Mississippian Limestones suggests tectonic stability during the early and middle Paleozoic (Johnson, 2008).

The last cycle designated the Absaroka, occurred in the Pennsylvanian, and was influenced by tectonic events during the Early and Middle Pennsylvanian. The uplift of the Nemaha ridge divided the Arkoma and Anadarko Basins to the east and west, respectively. In contrast, Osage County to the northeast was part of a stable shelf, when cyclic, transgressive-regressive seas flooded and exposed the area at various intervals in the Middle and Late Pennsylvanian (Thorman and Hipshman, 1979). Transgression occurred in a general southeast to northwest direction. Marine reworking and/or fluvial activity concentrated chert fragments into structural lows with subsequent cementation to form a chert conglomerate termed the Mississippian Chat (Thorman and Hipshman, 1979). The erosion and concentration of the chert fragments that characterize the Mississippi Chat occurred on the exposed limestone surface at the Mississippian-Pennsylvanian Unconformity (Figure 4.1). Subsequent diagenetic modifications, where the Chat is highly porous or dense, weathered, and/or detrital are attributed to uplift, erosion, and weathering (Rogers, 2001). Chat deposition was concentrated along discontinuous channel systems resulting in variable thickness from nonexistent on structural highs to greater than 30 m (100ft) in channel deeps. Rogers (2001) proposed a twofold diagenetic history for the Mississippian Chat in Oklahoma consisting of (1) silica replacement of calcite, and (2)

dissolution of calcite remnants. The source of silica found in Mississippian chert may have been dissolution of sponge spicules, hydrothermal fluids, volcanic ash dissolution, weathering of silica-rich rocks, or a combination of these (Rogers, 2001).

Mikkelson (1966) reported the existence of a second Chat which is (100+ ft) below the Chat overlying the Miss Lime (first chat), and noted that in some cases the first and second Chat may combine as a continuous Chat section. The second Chat was reported as “cotton rock” in the subsurface tri-state mining district by McKnight and Fisher (1970) and is characterized in wireline logs by nearly pure quartz mineralogy. Rogers (2001) identified two separate Chat intervals on the Osage-Davis Bros. 24-5-6 1C, which is well C in this study. Snyder (2016) found two Chat units and called the deeper occurrence “Secrest or Highway 60”. Rogers (2001) suggested these two intervals may have formed as a result of numerous episodes of karst development or eustatic changes, where the first Chat is related to weathering (epigene karst) and the second Chat which we term “tripolite” is related to subsurface groundwater dissolution in karst terrain (hypogene paleokarst). The tripolite top or “tripolite” is the paleo-water table contact between the phreatic and vadose zones, with local and multiple tripolitic chert intervals formed above the paleo-water table (Manger, 2014). The tripolite may be due to hydrothermal fluids that occurred during the Ouachita Orogeny, classified as tripolitic chert (McGilvery, Manger and Zachry, 2016). Cains (2019) reported that the tripolite is not found along bedding planes. Figure 4.1 (left image) shows a schematic diagram to illustrate the distinction between Chat and tripolite in Osage County. Figure 4.1 (right image) shows the stratigraphy of Osage County. Mikkelson (1966) noted that the term “Chat “does not indicate a specific geologic time interval nor a rock unit. Mazzullo and Wilhite (2010) suggested the abandonment of the term because it denotes any type of chert and does not correlate to a specific lithology.

Available Data

This study utilized a 116 km^2 (45 mi^2) of 3D seismic data. Figure 4.2a is the location of the study area in Oklahoma relative to the United States. Figure 4.2b is the seismic coverage map and adjoining wells. The seismic volume was acquired in the 1990s, and poststack migrated using FX-X Stolt migration. The seismic data has a 2 ms sample rate, 2.0 s record length, bin size of 20 x 20 m (66 x 66 ft), 400 W-E in-lines and 721 N-S crosslines. The processing datum is 274 m (900 ft) with a replacement velocity of 3048 m/s (10000 ft/s) and a CDP nominal fold of 70. Fourier analysis shows the bandwidth is 10.6 and 104.1 Hz at -20dB, with a dominant frequency of ~57.5 Hz.

Table 1.0 shows wells with available logs, core photos, X-ray fluorescence (XRF) and the formation depths encountered in ten wells (A - J). These wells were drilled between 1955 and 2012. Wells F, G, H, I and J are outside the seismic coverage. Wells A - F except for C has digital logs; C is a raster log from Rogers (2001). Well B has full wave sonic (V_P and V_S) and penetrated the top Arbuckle. Well F reached the Precambrian granite, and the remaining wells penetrated the Miss Lime. Wells G - J have cores with characteristic red staining in G and H. Wells I and J have XRF.

Methods

We correlated wells A through F with a lateral extent of 18.3 km (Figure 4.3). Datum for the cross section is the MPU. The Miss Lime was divided into informal zone designations of upper Miss Lime above the tripolite and lower Miss lime below the tripolite, where tripolite is present. We analyzed available core photos and XRF data in wells.

A full wavelet with a length of 100 ms, a 25 ms taper and a sample interval of 2 ms to match seismic data was extracted from the seismic data at a time window of 500-700 ms at well

B location on the seismic data. The extracted wavelet showed that phase varied with frequency with an average phase of -32 degrees (Figure 4.4). The wavelet was convolved with the reflection coefficient from well B to generate a synthetic seismogram. Chat shows a weak positive peak, tripolite shows a strong negative peak, and limestone indicate a strong positive peak (Figure 4.4).

Gamma ray, resistivity, density, mineralogy, acoustic and shear sonic logs for Well B were plotted with the intervals of interest (Chat and tripolite) projected to an seismic amplitude section (Figure 4.5). A model-based inversion estimates acoustic impedance from field post stack seismic data calibrated to well logs, formation depths, and thicknesses (Barclay et al., 2008) A model-based inversion was computed for the 3D seismic volume to estimate acoustic impedance (Figure 4.6c). This involved creating an initial model that used the density and sonic logs of wells A and B, iterating over the 3D seismic volume (0 - 1000 ms) at a 2 ms sample interval and a high cut filter of 10/15 Hz for model filtering after lateral interpolation. Seismic horizons guiding the inversion include Pawhuska, Avant, Oswego Lime, Miss Lime, Arbuckle, and Precambrian basement.

Using log data from well B, V_P/V_S ratio against acoustic impedance was plotted to characterize the nature of Chat, upper Miss Lime, tripolite, and lower Miss Lime (Figure 4.6).

We plotted acoustic impedance versus total porosity (root mean square of neutron porosity and density porosity) for the Chat, upper Miss Lime, tripolite, and lower Miss Lime intervals in well B (Figure 4.8) which revealed a robust relationship across all these zones of the form

$$AI = 59168 * (TPHI)^2 - 97780 * TPHI + 52111 \quad (1)$$

$$TPHI = 2.50 * 10^{-10} * (AI)^2 - 3.16*10^{-5} * (AI) + 0.988 \quad (2)$$

where the correlation coefficient R = -0.96. These equations are empirical least squares fit to data points using polyfit - a python numPy function.

Well B histogram plots for primary velocity (V_P), shear velocity (V_S), density and acoustic impedance (AI) were generated respectively for the Pennsylvanian Shale, Chat, upper Miss Lime, tripolite, and lower Miss Lime (Figure 4.9). Table 2.0 shows the mean values for V_P, V_S and density for the Pennsylvanian Shale, Chat, upper Miss Lime, tripolite and lower Miss Lime. The number of sample points are 200, 36, 246, 62 and 326 for Penn Shale, Chat, upper Miss Lime, tripolite and lower Miss Lime, respectively.

We generated zero offset synthetic wedge models for shale/chat/limestone interfaces (Figure 4.10) and limestone/tripolite/limestone interfaces (Figure 4.11) with a thickness of 80 ft, at 5 ft increments respectively, using sonic and density logs from Well B. This provided information about amplitude changes with variable thickness for the upper and lower interfaces of Chat and tripolite, respectively.

Fracture porosity in Well B was calculated for the chat, upper Miss Lime, tripolite and lower Miss Lime (Figure 4.12). Fracture porosity (secondary porosity) is the difference between total porosity and sonic porosity. Sonic porosity was calculated using Wyllie equation.

Continuous Chat and tripolite negative amplitude reflections with high confidence tracking on seismic data were mapped. We produced maps of time; amplitude extracted at 0 ms; acoustic impedance extracted below 4ms; and porosity using equation 2 for the Chat and tripolite respectively (Figures 4.13 and 4.14).

Interpretation of Results

Well Analysis

The stratigraphic section that is the focus of this study is 152 m (500 ft) in thickness, which includes 30 m (100 ft) of the overlying Pennsylvanian Shale. The correlation illustrated in Figure 4.3 shows an increase in Chat thickness from Wells A - F towards the northeast (Figure 4.3). Note, that Well F is not within the seismic coverage (Figure 4.2). Chat, upper Miss Lime, tripolite and lower Miss Lime were correlated. This cross section shows the laterally variability of the Chat at the top of the upper Miss Lime with maximum thickness of 21 m (70 ft) in Well F. Note a reduction in density (RHOB) values documented by the RHOB curve from values ~2.2 g/cm^3 in wells A-C down to 2.0 g/cm^3 in Wells D-F (Figure 4.3).

Tripolite was encountered in wells B and C. It is about 100 feet below the Chat, as observed by Mikkelson (1966), Rogers (2001) and Snyder (2016). The thickness varies from 10 m (30 ft) in well B diminishing to 3 m (10 ft) in Well C (Figure 4.3). Liner (2018) reported an average thickness of about 30 m (100 ft) and a density of less than 2.1 g/cc for the tripolite in the Mississippian Boone Limestone in northwest Arkansas, 160 km (100 mi) east of Osage County. Wells D and E were not drilled deep enough to ascertain and correlate tripolite occurrence.

Characteristic red staining was observed on core of Chat in Wells G, H, and I (Liner, 2015), and probably in Well D. X-ray fluorescence (XRF) analysis of these red stains in Well I show the presence of 2% dickite, 25% dioptase, 36% kaolinite and 37% quartz at a depth of 846 m (2775 ft). Stylolite related fractures are associated with the red stains in well I. XRF on the Chat in Well J shows no dickite and dioptase. XRF analysis of red stains in Well I suggests possible presence of dioptase and dickite in Wells D, G and H.

Dioptase is an uncommon copper silicate mineral linked with quartz and calcite inclusions along with many other copper and lead secondary minerals formed from weathering of hydrothermally formed copper sulfides. Dickite is a kaolin mineral which occurs in limestones and shows evidence that acidic, organic-rich (hypogene) fluids caused rock alteration (Wright and Harris, 2013; Wright, 2016), leaching silica oxide and aluminum (Wright, 2016). Schroeder and Hayes (1968) noted that dickite formation in Pennsylvanian limestones in southeastern Kansas occurred when groundwaters significantly mixed with up-dip migrating waters of magmatic origin. The presence of corroded stylolite-related fractures indicates deep burial corrosion associated with hypogene activity (Wright and Harris, 2013; Wright, 2016). The combined evidence of dioptase, dickite and stylolites indicates a hydrothermal aspect for the Chat.

There was no XRF or geochemical analysis carried out on the tripolite in any of the wells. However, studies of the tripolite in the Boone Limestone, northwest Arkansas using scanning electron microscopy (SEM) by Minor (2013), Manger (2014), Chick et al. (2017) and McKim et al. (2017) show the presence of quartz crystals with double terminations. Manger (2014) indicated the tripolitic chert experienced a subsequent inundation by hydrothermal fluid rich in silica that permitted quartz crystallization in voids produced by previous decalcification. He suggested that the hydrothermal fluids may be the same medium that deposited Mississippi Valley Type deposits in northeastern Oklahoma, Kansas, and Missouri, during the Ouachita Orogeny.

Figures 4.5 and 4.6 show well B with the intervals of interest - Chat and tripolite correlated to seismic data as two distinct elements. Note the low resistivity, low density of about 2.2 g/cc indicating high porosity, high acoustic, and high shear transit times of Chat and tripolite

relative to the Miss Lime. The mineralogy log indicates very negligible fractions of dolomite in the tripolite, and no occurrence with the Chat. In the Miss Lime, the carbonate is predominantly calcite with limited quantities of dolomite, higher in the lower Miss Lime than in the upper Miss Lime. The presence of quartz in the upper and lower Miss Lime suggests the Miss Lime is a cherty limestone. Both Chat and tripolite are characterized by dominant quartz fractions of 82% and 91% respectively, with no carbonate fraction in the Chat. Table 2.0 shows mean values for silica, carbonate and clay in the Pennsylvanian Shale, chat, upper Miss Lime, tripolite, and lower Miss lime.

The rock physics plot of V_P/V_S versus acoustic impedance (Figure 4.7) shows a clear distinction between chat/tripolite clusters from limestone at 40000 g/cm^3 x ft/s based on acoustic impedance alone. However, we note that there is not a distinct separation of V_P/V_S between Chat and tripolite.

The Chat and tripolite show total (primary and secondary) porosities up to 30% (Figure 4.8) which is consistent with a low acoustic impedance (Figure 4.7). The Miss Lime has a total porosity of less than 10 % with a higher acoustic impedance than Chat and tripolite (Figures 4.7 and 4.8). There is a subtle separation between the Chat and tripolite along the line of best fit, with Chat plotting above the polynomial fit relative to tripolite for porosities greater than 25%. Equations 1 and 2 may be used as a proxy to compute for acoustic impedance and total porosity respectively for limestone, Chat and tripolite formations in Osage County, Oklahoma.

Figure 4.9 shows the histogram plots of elastic parameters for shale, Chat, upper Miss Lime, tripolite and lower Miss Lime. V_P shows separation of limestone, from chat, tripolite and shale, but no distinct partition between chat/tripolite and shale. The lack of distinction between shale and Chat supports the lack of a notable acoustic impedance contrast at the well location.

This lack of separation probably reflects the high total porosity in the Chat and the high micro porosity in the shales. V_S shows a clear separation of chat/tripolite, from shale and limestone. This suggests a shear impedance inversion may characterize Chat and tripolite zones when available. The density histogram shows significant departure of Chat and tripolite from limestone, and not shale, which suggests that a density inversion volume with available prestack gathers can delineate Chat and tripolite from limestone without shale. This confirms work by Dowdell et al. (2013) who used density inversion to map low density chert in the Miss Lime. Table 2.0 shows the mean values for V_P, V_S, density and AI for shale, Chat, limestone and tripolite.

Constructive interference occurs when the reflections from the upper and lower interfaces interfere creating a strong event at the tuning thickness (Robinson and Treitel, 2008). Amplitude below tuning thickness can be used to estimate sub-resolution thickness (Liner, 2016). The Chat thickness at well B is below the limit of seismic vertical resolution (Table 2.0) and therefore will be investigated by use of a sonic-based normal incidence wedge model. Figure 4.10a shows the wedge model for the Chat zone. The thickness of the Chat in Well B is about 5 m (17 ft, red circle), and is approximately impedance matched yielding a very weak positive amplitude at the upper interface on the amplitude versus thickness plot (Figure 4.10b) in agreement with observed seismic response (Figures 4.5 and 4.6b) and corroborated by the synthetic seismogram which shows a weak positive amplitude for the Chat (Figure 4.4). The wedge model indicates low seismic Chat visibility at the well B location may be caused by sub-resolution Chat thickness (Table 4.2) and nearly matched impedance between Penn shale and Miss Chat (Figure 4.9d). The upper interface amplitude-thickness plot indicates that at least 6 m (20 ft) of Chat is required to create a negative amplitude seismic response. The lower interface amplitude-thickness plot

shows positive amplitudes for all Chat thicknesses with a maximum positive amplitude at 15 m (50 ft) (Figure 4.10c). This wedge model implies resolution of top/base Chat events requires at least 12 m (40 ft) thickness, agreeing with Snyder (2016) who showed that the top and base of the Chat at 12 m (40 ft) with a negative amplitude at the Chat top and positive impedance at the Chat base.

Figure 4.11a shows the wedge model for the tripolite zone. The upper interface amplitude versus thickness plot shows a negative amplitude for the 10 m (30 ft) thick tripolite at the well location (Figure 4.11b, red circle), this is corroborated with negative amplitude on the seismic (Figure 4.6b). We can detect negative amplitudes for thicknesses as low as 3 m (10 ft). The lower interface amplitude versus thickness plot shows a maximum amplitude at 14 m (45 ft) (Figure 4.11c). The top and base of tripolite can be mapped for thicknesses greater than 30 ft.

Chat fracture porosity (FPHI) shows a mean of 12% and a maximum of 15% (Figure 4.12a). The upper Miss Lime shows negligible FPHI, which is relatively unfractured (Figure 4.12b). The tripolite shows 1-13% fracture porosity with more vertical variation than Chat FPHI (Figure 4.12c), and the lower Miss Lime shows an unfractured rock (Figure 4.12d). The high FPHI in Chat may be due to breccia collapse or Pennsylvanian tectonic movement (Zajic, 1956). Chat may need a lesser hydraulic frac pressure compared to the tripolite and may also have a higher permeability and flow rate compared to the tripolite.

Seismic Analysis

Figure 4.6a-c shows geo-seismic, amplitude and acoustic impedance section for a north-south crossline across well B. The Chat is below the MPU which is an erosional unconformity with a rugged topography around the well and shows continuity away from the well. Chat is seen on the amplitude data as a strong negative event (Label C), which is a well-developed Chat north

and probably south of well B, but thin and poorly developed with low amplitude on the well (Figure 4.6b). The upper Miss Lime is below the Chat which a weak positive amplitude (Figure 4.4) or approximately impedance matched reflection, followed by the underlying tripolite zone that is well developed, and seen as a strong negative event (label T) continuing across well B (Figure 4.6a and 4.6b). Note, there is no remarkable negative amplitude in the wellbore for the Chat, in contrast to the deeper tripolite which shows a continuous high negative amplitude at and away from the well location. Variation in Chat and tripolite acoustic impedance is seen on the acoustic impedance as low impedance in the inversion result (Figure 4.6c).

Chat Attribute Maps

Figure 4.13a-d shows Chat horizon time structure, amplitude, acoustic impedance, and porosity maps, respectively. Wells A-E all encountered Chat. Regions with no data show low confidence, where the Chat is not mappable on seismic data. These non-mappable regions may represent limestone, shale, or missing Chat at the unconformity as shown on Figure 4.3.6. The horizon time structure map (Figure 4.13a) shows Chat occurs between 550 and 640 ms with regional dip from northeast to southwest and high regions (hot colors) to the northeast with low regions (cool colors) in the south and south west. The Chat horizon amplitude (Figure 4.13b) is uses hot colors to show strong negative values. The well B location has a weak positive amplitude consistent with wedge model discussed earlier. The extracted Chat acoustic impedance map (Figure 4.13c) indicates values below 25000 g/cm^3 * ft/s near wells A and C, values at the lower limit of those observed in the well B histogram (Figure 4.9d). High porosities indicated south and north of Well A and east of well C (Figure 4.13d) have substantial ambiguity because seismic response in those areas seems to indicate Chat conditions not encountered in well B (Figure 4.8). A combination of strong negative amplitude, low acoustic impedance, and high

porosity south of wells A-C and east of well C indicate thick, well-developed Chat. This is the classic ‘strong signal’ Chat indicator, but the well B acoustic impedance histograms (Figure 4.9) show Chat can be approximately impedance matched with lower Pennsylvanian shale – in such a case Chat could be seismically transparent even though it is geologically a thick, high-porosity target. A ‘Chat dim-out’ seems a plausible exploration strategy based on our analysis. Prestack characteristics of the Chat reflection event may be a useful delineation tool in such cases, but this is beyond the scope of the current study.

However, we note that well A which has a thickness of less than 20 ft is in the region of high negative amplitude. This may due to the limit of visibility which is a changeable fraction of a wavelength, the acoustic contrast of the layer of interest relative to the surrounding material, random and coherent noise in the data, and the seismic wavelet phase (Brown, 2011). The well-developed Chat is greater than 3 km in lateral extent in the west-east direction, which could be tested by horizontal drilling. Strong negative amplitudes in low structural relief suggest thick transported Chat breccias.

Tripolite Attribute Maps

Figure 4.14a-d shows tripolite horizon time structure, amplitude, acoustic impedance, and porosity maps, respectively. Regions with no data are interpreted as an absence of tripolite where upper and lower Miss Lime are in contact. The time map for the tripolite shows where high-confidence tracking is feasible. The regional dip is northeast-southwest with time ranges from -570 to -650 ms. The shallowest areas (hot colors) are in the northeast and northwest, which has a northeast-southwest trending fault. This fault may have served as a conduit for hydrothermal waters that altered the Miss Lime to tripolite. Deeper regions (cool colors) are in the southwest (Figure 4.14a). Hot colors on the horizon amplitude map indicate greater negative values (Figure

4.14b). The modest negative amplitude at the Well B location is consistent with the wedge model (Figure 4.11). The acoustic impedance at Well B shows the values range from 28000 to 30000 (g/cm^3 * ft/s) which is consistent with the histograms in Figure 4.3.9d. Impedance results away from Well B show tripolite with lower acoustic impedance (<20000 g/cm^3 * ft/s) (Figure 4.14c). Anomalously high porosities shown to the northwest, northeast and east may have considerable ambiguity due to seismic response in those areas seems to show tripolite conditions unlike those encountered in well B (Figure 4.14d). A strong relationship between high negative amplitude, low acoustic impedance and high porosity indicates well-developed tripolite zones located on structural highs. These strong negative amplitudes may also indicate regions with thick tripolite units. Wells B and C on the map are the only wells that encountered tripolite (Figure 4.3). The tripolite map suggests that wells D and E may have encountered tripolite if it was drilled beyond the Miss Lime. The presence of tripolite on the structural high relief areas may have occurred during deformation of the structure during the Ouachita Orogeny with migrated fluids leaching and dissolving the Miss Lime. The distribution of the tripolite based on the maps shown in Figure 4.14 suggests a larger area of development relative to the Chat as shown in Figure 4.13. The delineated tripolite spatial geometry in the east of the study area shows the lateral extent in the north-south direction exceeding 6 km (3.7 mi). This suggests that the distribution of the Chat, both above and below the MPU is more locally controlled by structure and erosion versus the distribution of the tripolite attributed to regional subsurface flow of hydrothermal fluids.

Conclusion

We have characterized Mississippian paleokarst zones of Chat and tripolite associated with the Miss Lime using seismic and well logs. Chat is associated with an erosional unconformity found at the Mississippian-Pennsylvanian boundary, the top of the Miss Lime, while tripolite is internal to the Miss Lime. Well B acoustic impedance histograms show that Chat has a weak positive amplitude or approximate impedance match with overlying Pennsylvanian shales while low impedance tripolite is embedded in tight Miss Lime to produce a net strong negative amplitude based on sonic-based normal incidence wedge models. The wedge models indicate that Chat and tripolite generally show an increase in negative amplitudes with increase in thickness, but importantly Chat can be nearly transparent to seismic reflection under plausible circumstances. Such is the case at Well B that encountered 17 ft of chat but is essentially invisible on the seismic data. We note that high negative amplitudes observed for Chat are not solely due to thicknesses greater than the seismic resolution but also depend on acoustic impedance contrast, noise, and phase of the wavelet.

Chat shows a greater mean fracture porosity than tripolite while Miss Lime exhibits negligible fracture porosity in well B. Dioptase and dickite minerals associated with hypogenic (hydrothermal) fluids show that Chat had hydrothermal imprints apart from near-surface epigene processes as observed from XRF data. Outcrop SEM results show double terminated quartz crystals in tripolite which indicate hydrothermal fluid incursion probably during the Ouachita orogeny along with emplacement of nearby Mississippi Valley Type ore deposits.

Seismic analysis shows that well-developed Chat and tripolite regions are often characterized by strong negative amplitudes, the classic ‘strong response’ exploration target, but may also be effectively transparent to seismic reflection, suggesting a new exploration method of

mapping ‘Chat dim-outs’. This may reflect transport and concentration of eroded chert fragments in these lows. Attribute maps indicate that tripolite has slightly lower acoustic impedance and higher porosity away from well control used in this study. The best Chat development is found in low structural relief. Well-developed tripolite is associated with structural highs located in the northwest, northeast and east of the 3D seismic area. This suggests flow focusing of hydrothermal fluids key to the development of tripolite toward structural highs. Mapping indicates tripolite has a larger coverage area than Chat, although only two wells in the study area were deep enough to encounter tripolite.

This study provides an interpretive framework for characterizing Chat/tripolite zones associated with the Mississippian Lime in the US Midcontinent, which may be applicable to regions around the world.

Acknowledgments

The authors are grateful to the Osage Mineral Council for providing the seismic data. Sullivan and Company for donating the well data for Wells A, B, D and E; Ceja corporation for providing data for Well F. Stephens Production Company for wells G-J. Schlumberger and CGG for Petrel and Hampson Russell software licenses, respectively. Python Petropy library was used for log plots and Seaborn library for scatter plots. Dr. Walter Manger and Dr. Thomas A. McGilvery contributed to an early revision of this manuscript.

References

Barclay, F., A. Bruun, K. B. Rasmussen, J. C. Alfaro, A. Cooke, D. Cooke, D. Salter, R. Godfrey, D. Lowden, S. McHugo; et al., 2008, Seismic inversion: Reading between the lines: Oilfield Review, **20,** 42–63.

Bass, N. W., 1942, Subsurface geology and oil and gas resources for Osage County, Oklahoma, Part II, Summary of subsurface geology with special reference to oil and gas: U.S. Geological Survey Bulletin 900-K, 343–393.

Benson, R. C., 2014, 3D seismic mapping of probable tripolitic chert bodies in Osage County, Oklahoma: M.S. thesis, University of Arkansas.

Brown, A. R., 2011, Interpretation of three-dimensional seismic data, 7ed.: AAPG Memoir 42, SEG Investigations in Geophysics No. 9.

Cains, J. M., 2019, Geochemical analysis of Mississippian cherts and Devonian-Mississippian novaculites, southern midcontinent region: M.S. thesis, University of Arkansas.

Chick, J., J. Cains, F. McFarlin, S. McKim, and A. Potra, 2017, Hydrothermally emplaced Lower Mississippian, tripolitic chert and its possible relationship to the Tri-State lead-zinc mining district: Journal of the Arkansas Academy of Science, **71**, 169–172.

Dowdell, B. L., A. Roy, and K. J. Marfurt, 2012, An integrated study of a Mississippian tripolitic chert reservoir — Osage County, Oklahoma, USA: 82nd Annual International Meeting, SEG, Expanded Abstracts, 1–5, doi: 10.1190/segam2012-1563.1.

Dowdell, B. L., J. T. Kwiatkowski, and K. J. Marfurt, 2013, Seismic characterization of a Mississippi Lime resource play in Osage County, Oklahoma, USA: Interpretation, **1**, no. 2, SB97–SB108, doi: 10.1190/INT-2013-0026.1.

Elebiju O. O, S. Matson, G. R. Keller, and K. J. Marfurt, 2011, Integrated geophysical studies of the basement structures, the Mississippi chert, and the Arbuckle Group of Osage County region, Oklahoma: AAPG Bulletin, **95**, 371–393, doi: 10.1306/08241009154.

Fritz, R. D., P. Medlock, M. J. Kuykendall, and J. L. Wilson, 2013, The geology of the Arbuckle Group in the midcontinent: Sequence stratigraphy, reservoir development, and the potential for hydrocarbon exploration: AAPG Search and Discovery Article #30266.

Guo, S., B. Zhang, S. Verma, and K. J. Marfurt, 2014, Vector correlation of AVAz and curvature attribute-Application to Mississippian Tripolitic Chert, Osage County, Northeast Oklahoma: 84th Annual International Meeting, SEG, Expanded Abstracts, 346–350, doi: 10.1190/segam2014-1353.1.

Jennings, C., 2014, Mechanical stratigraphy of the Mississippian in Osage County, Oklahoma: M.S. thesis, University of Arkansas.

Johnson, K. S., 2008, Geologic History of Oklahoma in K. S. Johnson, and K. V. Luza, eds., Earth sciences and mineral resources of Oklahoma: Oklahoma Geological Survey Educational Publication 9, 3–5.

Liner, K., 2015, An investigation of 3D seismic deep basement events in Osage County, Oklahoma: M.S. thesis, University of Arkansas.

Liner, C. L., 2016, Elements of 3D seismology, 3rd ed.: SEG.

Liner, T., 2018, Subsurface analysis of Mississippian tripolitic chert in northwest Arkansas: M.S. thesis, University of Arkansas.

Manger, W. L., 2014, Tripolitic chert development in the Mississippian lime: New insights from SEM: AAPG Search and Discovery Article #50957.

Matos, M. C., M. Yenugu, S. M. Angelo and K. J. Marfurt, 2011, Integrated seismic texture segmentation and cluster analysis applied to channel delineation and chert reservoir characterization: Geophysics, **76**, no. 5, P11–P21, doi: 10.1190/GEO2010-0150.1.

Mazzullo, S. J., and B. W. Wilhite, 2010, Chert, tripolite, spiculite, Chat – what's in a name?: Kansas Geological Society Bulletin, **85**, 21–25.

McGilvery, T. A., Manger, W. L., and Zachry, D. L., 2016, Summary and Guidebook to the Depositional and Tectonic History of the Carboniferous Succession Northwest Arkansas. Guidebook: AAPG Mid-Continent Field Conference.

McKim, S., J. Cains, J. Chick, F. McFarlin and A. Potra, 2017, Lithologic stratigraphic position, sequence and diagenetic history, lower Mississippian tripolitic chert, northern Arkansas, and southern Missouri: Journal of the Arkansas Academy of Science, **71**, 165–168.

McKnight, T. W., and R. P. Fischer, 1970*,* Geology and ore deposits of the Picher field, Oklahoma and Kansas, Geological Survey Professional Paper 588: USGS, 1–165.

Milad, B., R. Slatt, and Z. Fuge, 2020, Lithology, stratigraphy, chemostratigraphy, and depositional environment of the Mississippian Sycamore rock in the SCOOP and STACK area, Oklahoma, USA: Field, lab, and machine learning studies on outcrops and subsurface wells: Journal of Marine and Petroleum Geology, 115, 1–18, doi: 10.1016/j.marpetgeo.2020.104278.

Milad, B., and R. Slatt, 2018, Impact of lithofacies variations and structural changes on natural fracture distributions: Interpretation, **6**, no. 4, 1–15, doi: 10.1190/INT-2017-0138.1.

Milad, B., Ghosh, S., and R. Slatt. 2017, Comparison of rock and natural fracture attributes in karsted and non-karsted Hunton Group Limestone: Ada and Fittstown area: Shale Shaker Journal, **69**, no. 2, 70-86.

Mikkelson, D. H., 1966, The origin and age of the Mississippian "Chat" in north-central Oklahoma: OCGS – The Shale Shaker Digest, **5**, 255–265.

Minor, P. M., Analysis of tripolitic chert in the Boone Formation (lower Mississippian, Osagean), northwest Arkansas and southwestern Missouri: M.S. thesis, University of Arkansas.

Montgomery, S. L., J. C. Mullarkey, M. W. Longman, W. M. Colleary and J. P. Rogers, 1998, Mississippian "Chat" Reservoirs, South Kansas: Low-resistivity pay in a complex chert reservoir: AAPG Bulletin, **82**, 187–205.

Odegaard, E., and P. Avseth, 2004, Well log and seismic data analysis using rock physics template: First Break, **22**, no. 10, 37–43, doi: 10.3997/1365-2397.2004017.

Parham, K. D., and R. A. Northcutt, 1993, Mississippian chert and carbonate and basal Pennsylvanian sandstone—Central Kansas uplift and northern Oklahoma, *in* D. G. Bebout, W. A. White, T. F. Heritz, and M. A. Grasmick, eds., Atlas of major midcontinent gas reservoirs: Gas Research Institute and Texas Bureau of Economic Geology, 57–60.

Reeder, L. R., 1976, The control of potential Arbuckle hydrocarbon traps in Northeastern Oklahoma by Precambrian topography: OCGS - The Shale Shaker Digest, **24**, 176–186.

Robinson, E. A., and S. Treitel, 2008, Digital imaging and deconvolution: The ABCs of seismic exploration and processing: SEG.

Rogers, J. P., M. W. Longman, and R. M. Lloyd, 1995, Spiculitic chert reservoir rocks in Glick field, south-central Kansas: The Mountain Geologist, **32**, no. 1, 1–22.

Rogers, S. M., 2001, Deposition and diagenesis of Mississippian Chat reservoirs, north-central Oklahoma: AAPG Bulletin, **85**, 115–129.

Rogers, J., and M. W. Longman, 2001, An introduction to chert reservoirs of North America: AAPG Bulletin, **85**, 1–5.

Roy, A., B. L. Dowdell, and K. J. Marfurt, 2013, Characterizing a Mississippian tripolitic chert reservoir using 3D unsupervised and supervised multiattribute seismic facies analysis: An example from Osage County, Oklahoma: Interpretation, **1**, no. 2, SB109–SB124, doi:10.1190/INT-2013-0023.1.

Schroder, R. J., and J. B. Hayes, 1968, Dickite and kaolinite in Pennsylvanian limestones of southeastern Kansas: Clays and Clay Minerals, **16,** 41–49.

Snyder, R., 2016, A case history of the East Hardy Unit, Mississippian highway to trend, Osage County, OK: AAPG Search and Discovery Article #20345.

Thomasson, M. R., R. W. Kettle, R. M. Lloyd, R. K. McCormack, and J. P. Lindsey, 1989, Seismic detection and interpretation of porosity in Carboniferous age rocks of Kansas and Oklahoma: Geophysics, **54**, 1371–1383.

Thorman, C. H., and M. H. Hibpshman, 1979, Status of mineral resource information for the Osage Indian Reservation, Oklahoma: U.S. Geological Survey and Bureau of Mines, Administrative Report BIA-47, 1–60.

Watney, W. L., W. J. Guy, and A. P. Byrnes, 2001, Characterization of the Mississippian Chat in south-central Kansas: AAPG Bulletin, **85**, 85–113.

Wright, P., and P. Harris, 2013, Carbonate dissolution and porosity development in the burial (mesogenetic) environment: AAPG Search and Discovery Article #50860.

Wright, P.W., 2016, https://www.npd.no/globalassets/2-force/2019/documents/archive-2010-2018/advances-in-siliciclastic-and-carbonate-sedimentology/paul-wright---hypogene-palaeokarst-and-burial-corrosion.pdf, accessed 26 May 2020.

Yenugu, M., K. J. Marfurt, and S. Matson, 2010, Seismic texture analysis for reservoir prediction and characterization: The Leading Edge, **29**, 1116–1121.

Zajic, W. E., 1956, Nichols pool *in* Kansas oil and gas pools (south central Kansas): Kansas Geological Society, **1**, 69–73.

Figures

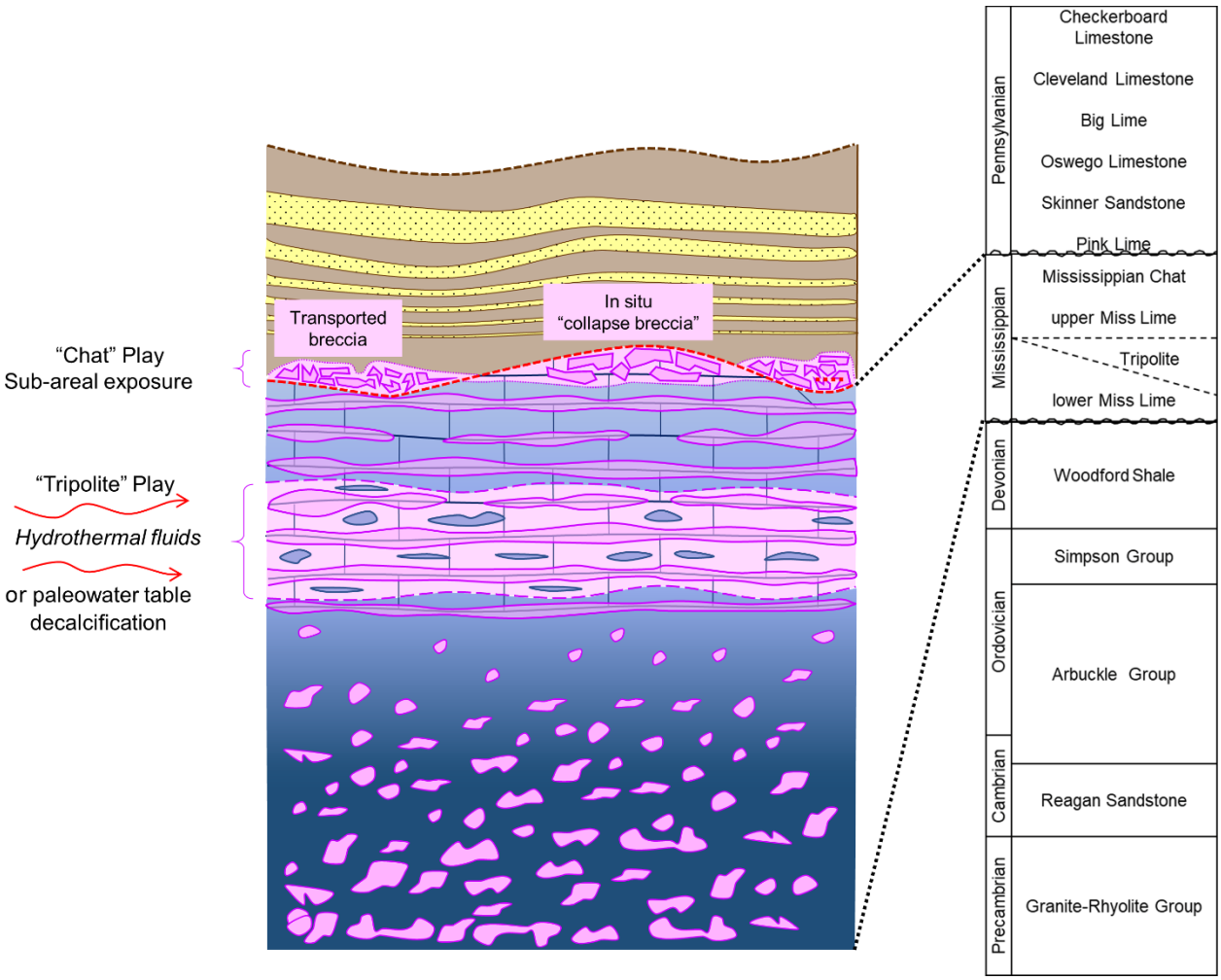

Figure 4.1. (left) Schematic diagram of the Mississippian (source: T. McGilvery personal comm.) and (right) stratigraphic column as encountered in well B with stratigraphy below Arbuckle

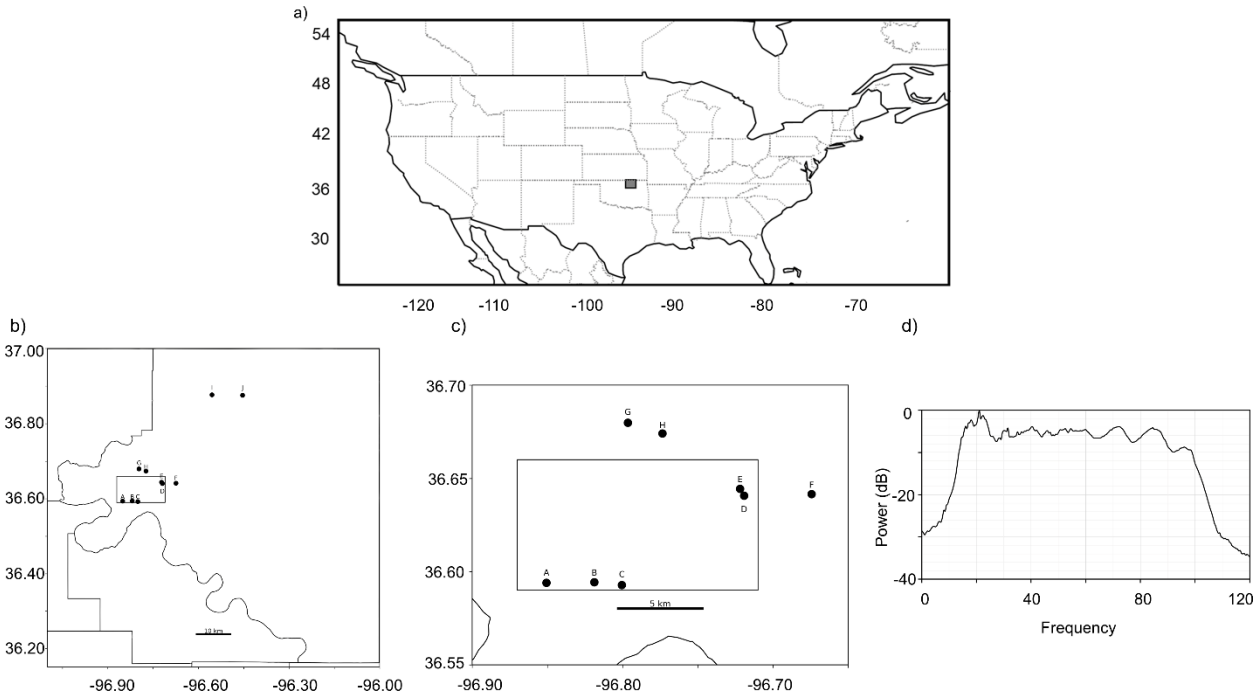

Figure 4.2. Study area (a) USA map showing study area is dark square in NE Oklahoma, (b) Osage County map showing wells (black circles) and 3D seismic coverage (black rectangle). The seismic was acquired in the 1990s (c) Detailed map of study area showing wells in and near the 3D seismic (d) Frequency spectrum of 3D seismic.

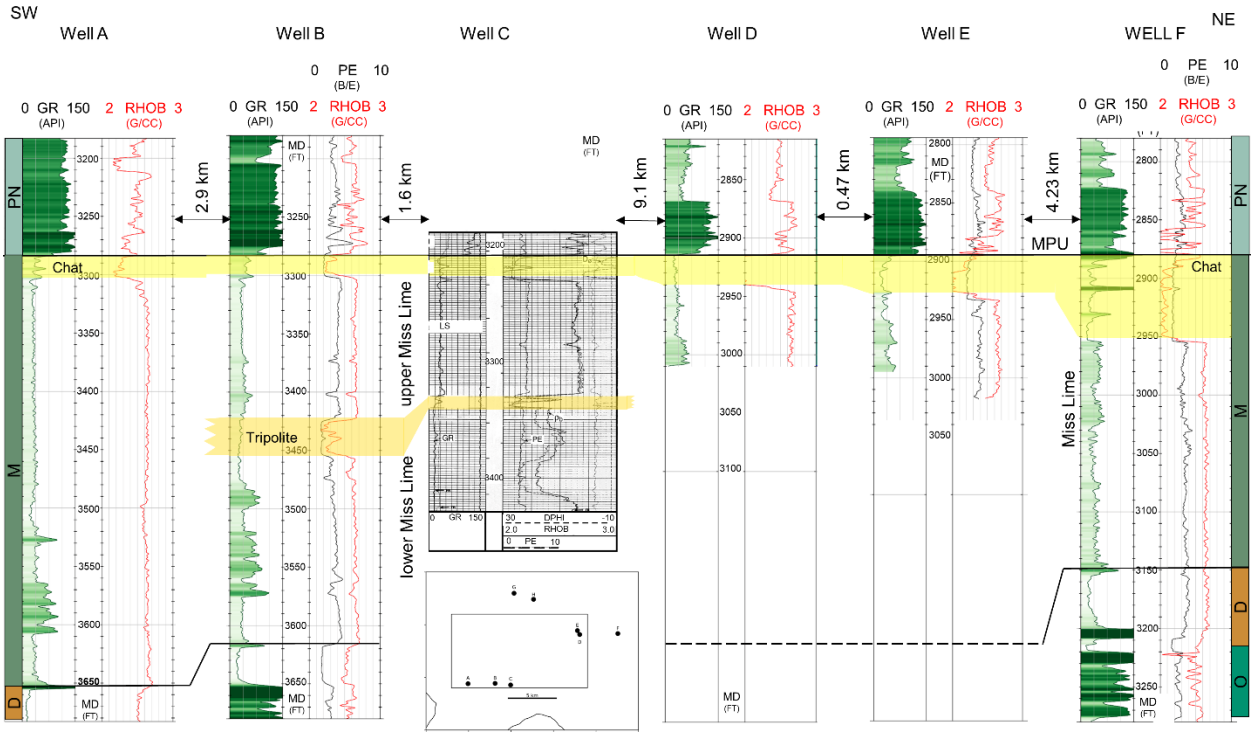

Figure 4.3. Correlation of selected well logs hung on the top Chat marker, note inset map at center bottom for well locations and inter-well distances noted between well tracks. The Chat is persistent across this section, tripolite is observed only in wells B and C.

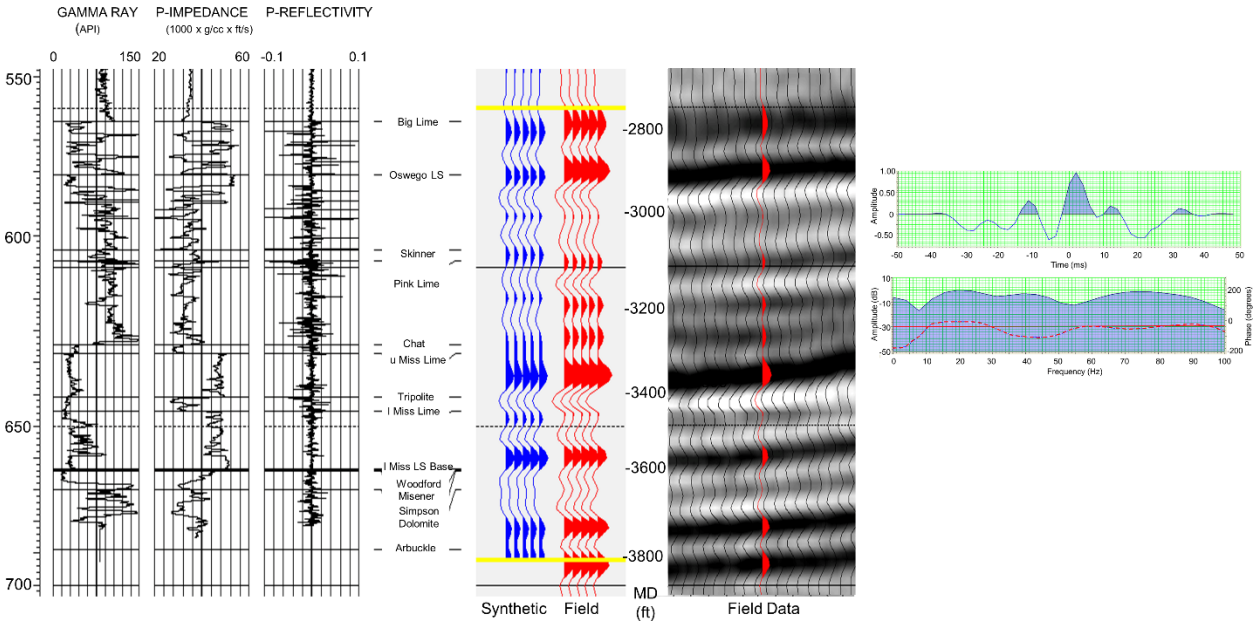

Figure 4.4. Well B seismic tie. Left panel show Gamma ray, P impedance and P-reflectivity. Centre panels show synthetic in blue, field data in red, and target interval between yellow lines (correlation ~80%) and seismic section through well. Right panel show full wavelet extracted from well B location for synthetic seismogram, phase is dashed red line, average phase is red line.

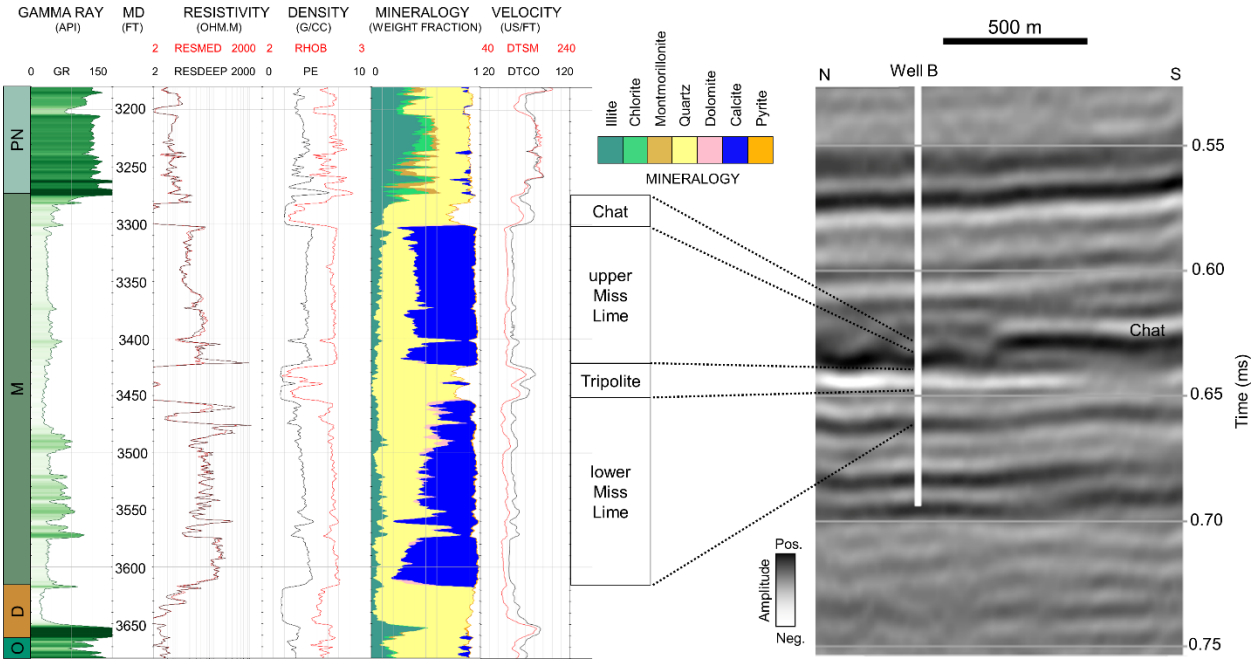

Figure 4.5. Well B wireline log plot tied to a seismic image through the well. Well logs are plotted over a 500 ft interval (152 m) showing gamma ray in API units, resistivity (RES) in ohm-m, density (RHOB) in g/cc, deep resistivity (RESDEEP), medium resistivity (RESMED), photoelectric effect (PE) in barns/electrons, mineralogy, P-wave sonic (DTCO) and S-wave sonic (DTSM) in us/ft.

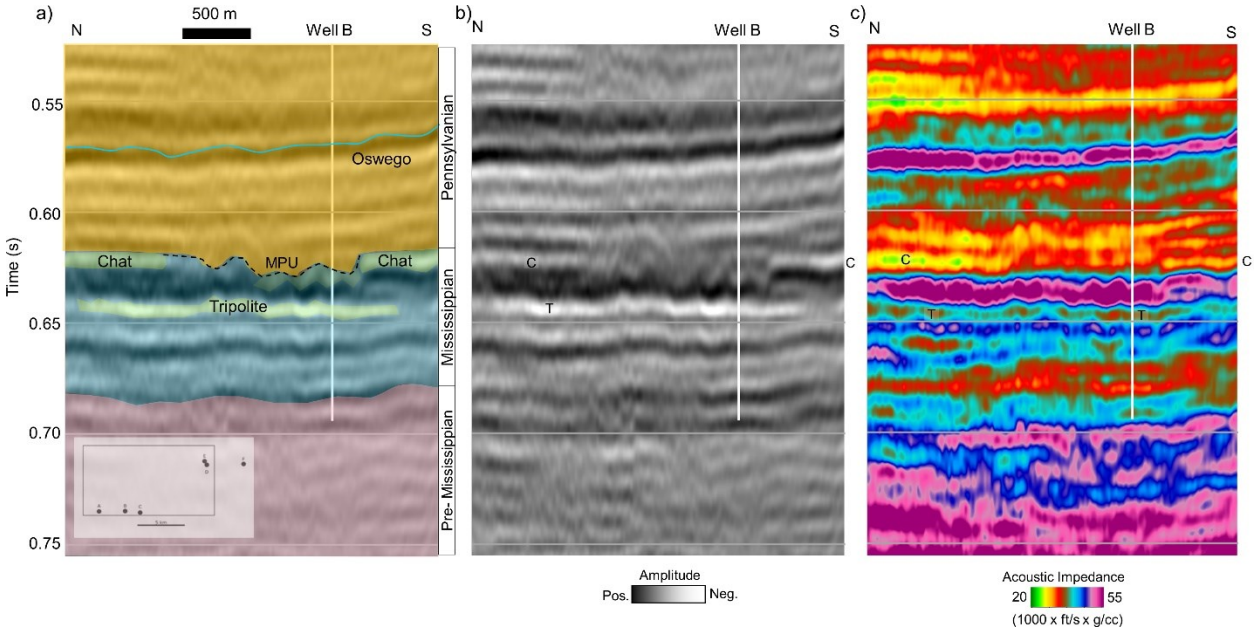

Figure 4.6. North to south seismic crossline across Well B. (a) Geoseismic section showing Mississippian-Pennsylvanian unconformity (MPU), as well as Chat and tripolite, which occur in the Mississippian section. (b) Uninterpreted seismic amplitude section. Chat (C) shows weak amplitude at well location and strong negative amplitude, north and south of well B. Tripolite (T) shows strong negative amplitude (c) Coincident acoustic impedance section indicating low impedance for both Chat and tripolite. Further, the laterally discontinuous nature of these zones is well represented in the impedance data.

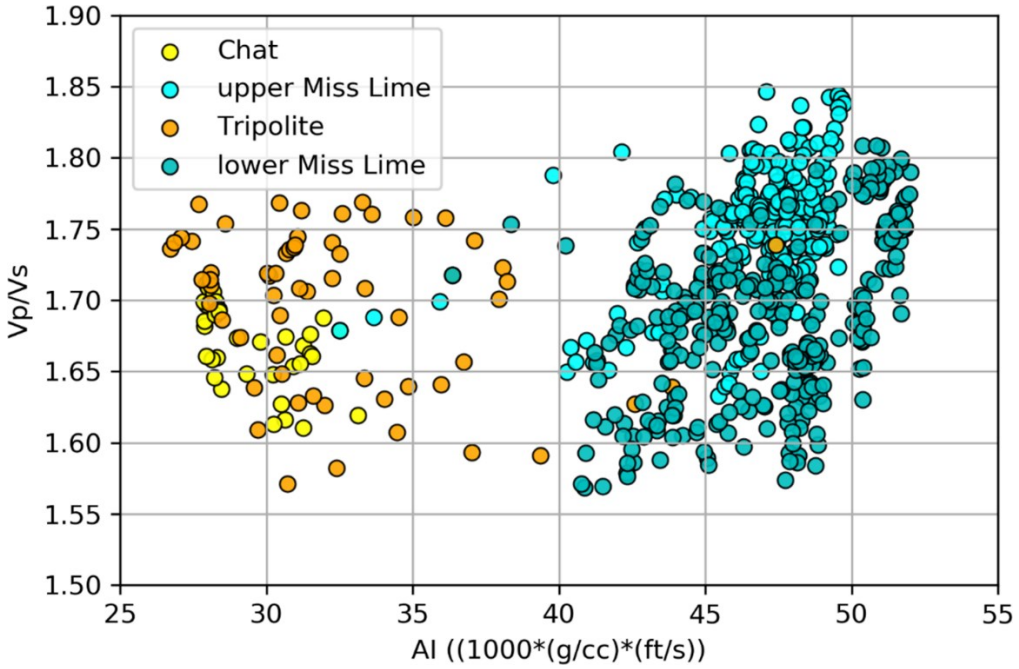

Figure 4.7. Well B plot of V_P/V_S versus acoustic impedance. On AI alone it is possible to separate U/L Miss Lime from Chat/tripolite. VP/VS the separation is not perfect, showing significant overlap on VP/VS.

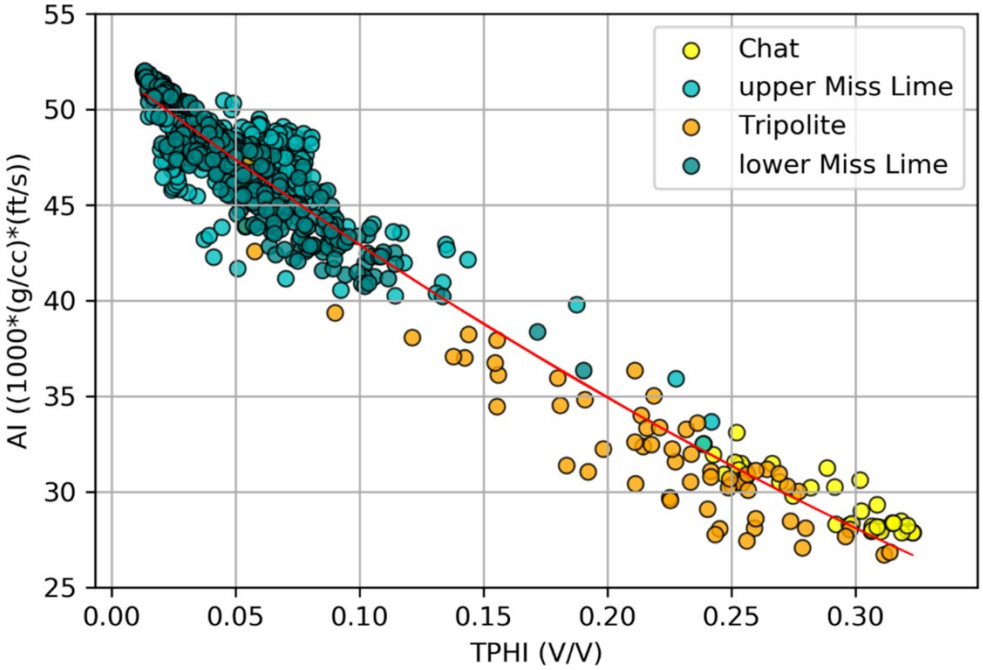

Figure 4.8. Well B plot of acoustic impedance (AI) versus total porosity (TPHI). TPHI is root mean square of neutron and density porosities.

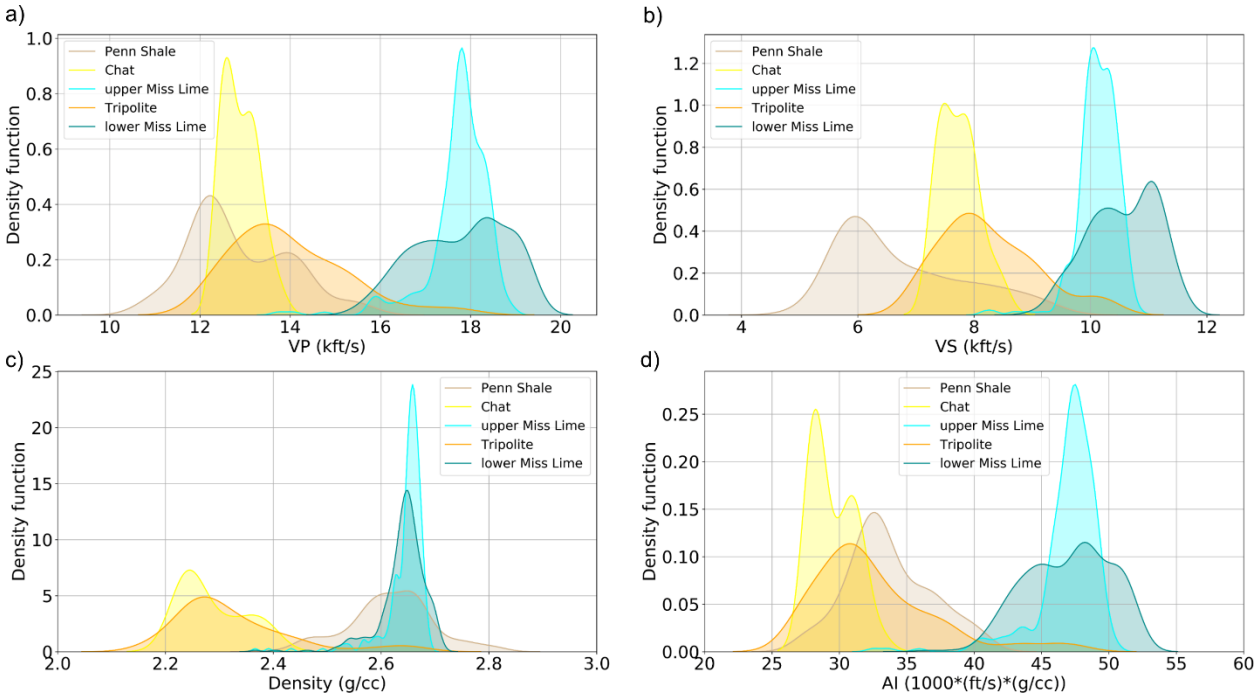

Figure 4.9. Well B histogram plots of elastic parameters, including 100 ft of lower Pennsylvanian and the complete Mississippian section (333 ft). (a) P-wave velocity (VP). (b) S-wave velocity (VS). (c) Density (d) Acoustic impedance (AI). Tripolite and Chat with very similar central values and with only small separation from central value of Pennsylvanian shale.

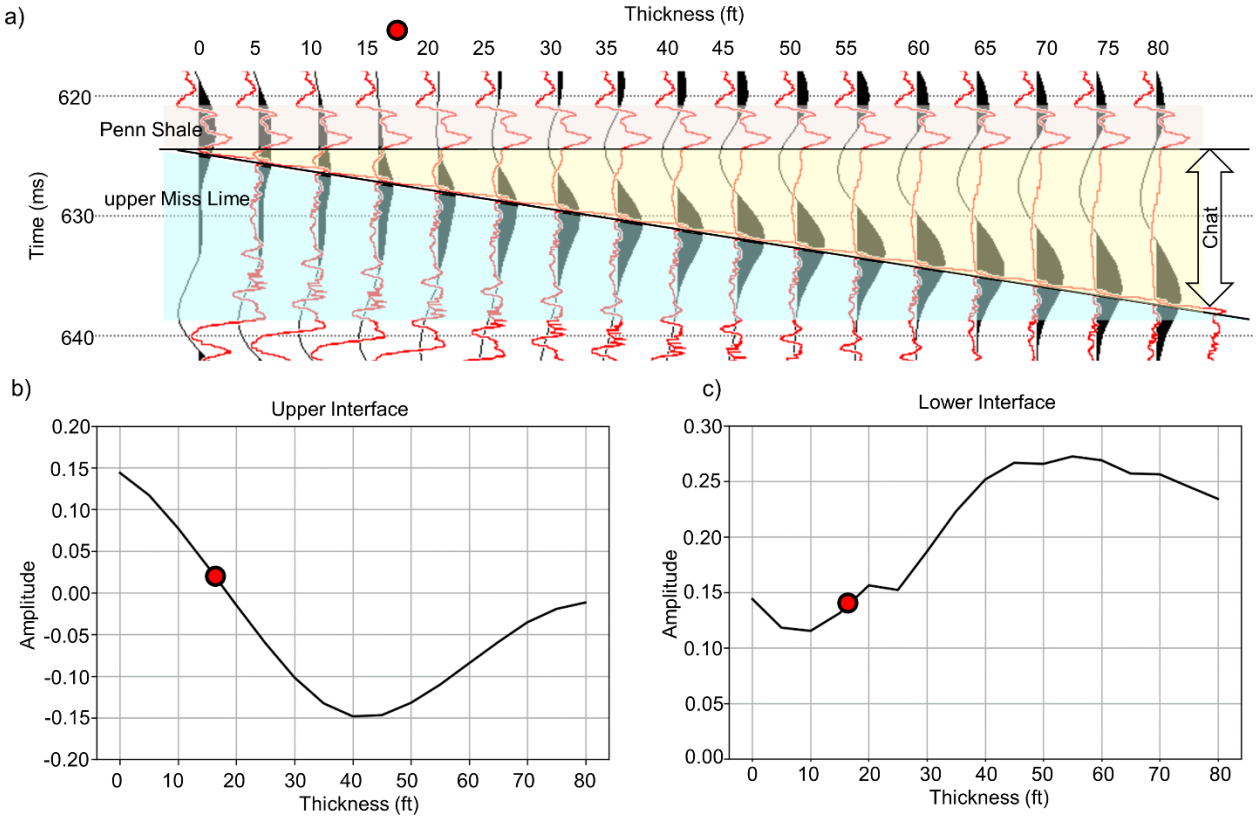

Figure 4.10. Normal incidence wedge model of variable Chat thickness in well B based on sonic log. (a) Wedge model produced by thickness variation of Chat interval. Red curve is P-wave sonic for each Chat thickness as labeled at the top. Red circle is thickness observed in well B. (b) Upper interface (shale/chat) amplitude versus thickness plot. Red circle shows weak amplitude at the well location. Amplitude becomes negative for Chat thickness > 20 ft. (c) Lower interface (chat/limestone) amplitude versus thickness plot. Maximum positive amplitude is at 55 ft.

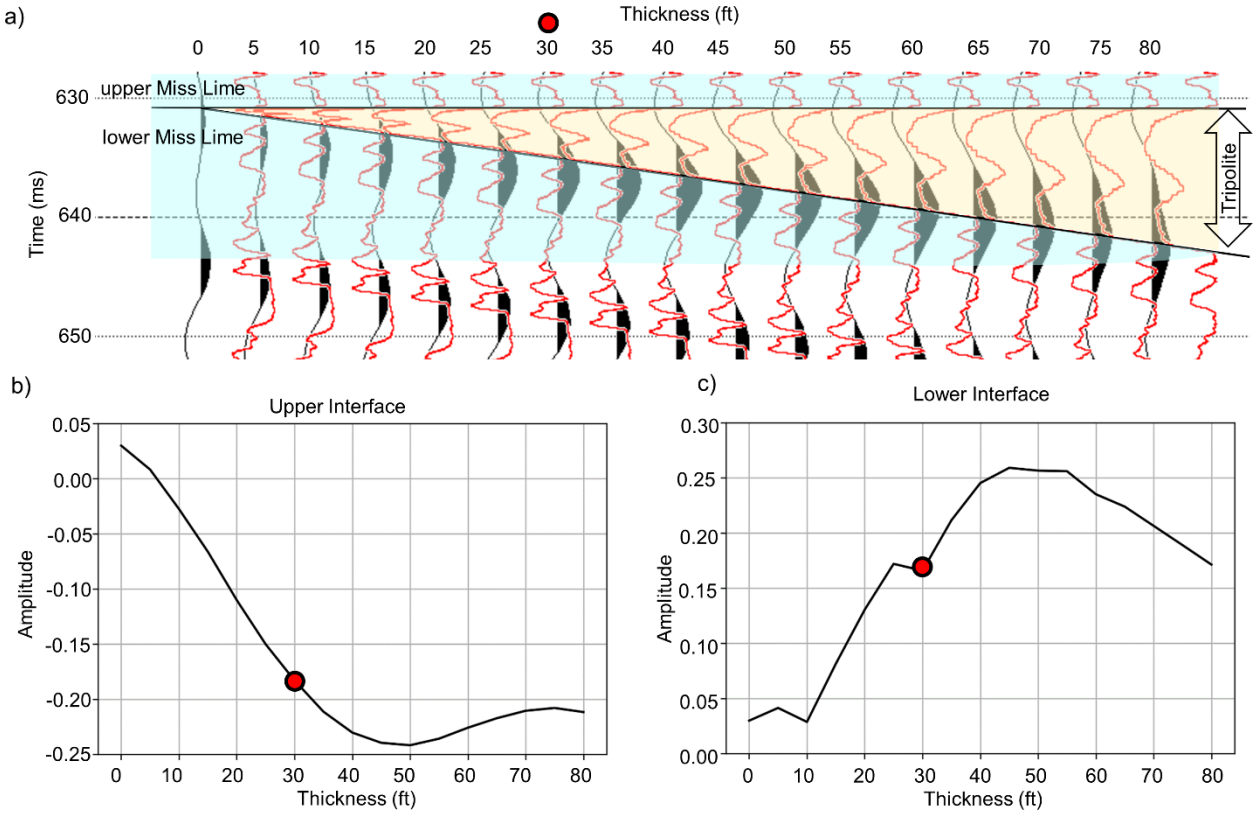

Figure 4.11. Normal incidence wedge model of variable tripolite thickness in Well B based on sonic log. (a) Wedge model produced by thickness variation of tripolite interval. Red curve is P-wave sonic for each tripolite thickness as labeled at the top. Red circle is thickness observed in well B. (b) Upper interface (U Miss Lime/tripolite) amplitude versus thickness plot. Maximum negative amplitude occurs at tripolite thickness of about 50 ft. (c) Lower interface (tripolite/L Miss Lime) amplitude versus thickness plot with well B case as red dot. Maximum positive amplitude occurs at tripolite thickness of 45ft.

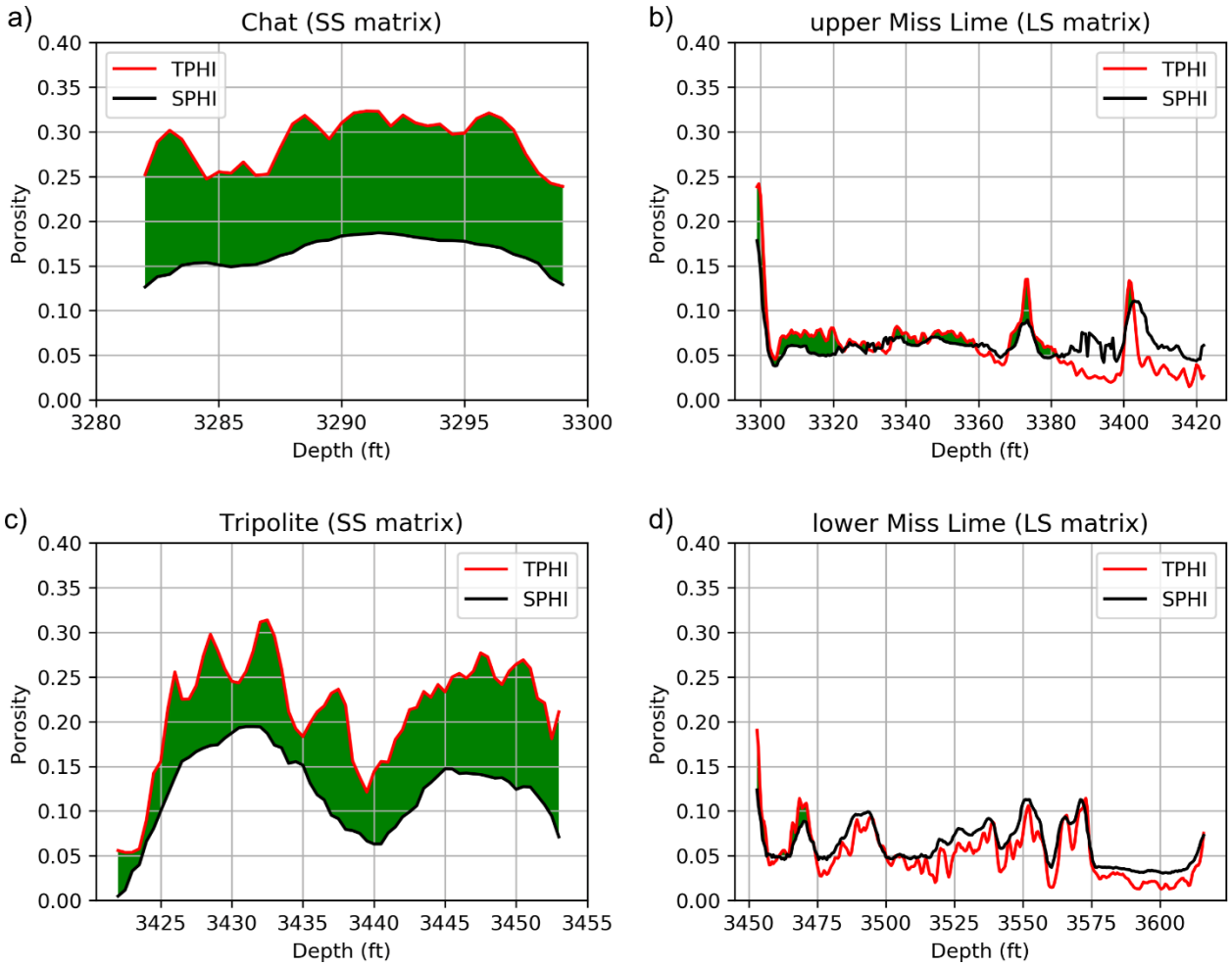

Figure 4.12. Well B log indications of fracture porosity in Chat, upper Miss Lime, tripolite and lower Miss Lime. Miss Lime porosities run on limestone matrix and Chat/tripolite porosity curves are computed on sandstone (quartz) matrix. Sonic porosity calculated using Wyllie equation. Red curve is total porosity (TPHI). Black curve is sonic porosity (SPHI) indicating matrix porosity. Green fill denotes fracture porosity (a) Chat interval porosity versus depth. which averages 12% (b) upper Miss Lime shows only minor fracture porosity. (c) Tripolite shows more vertical variation than Chat fracture porosity. (d) lower Miss Lime effectively calculates to be unfractured.

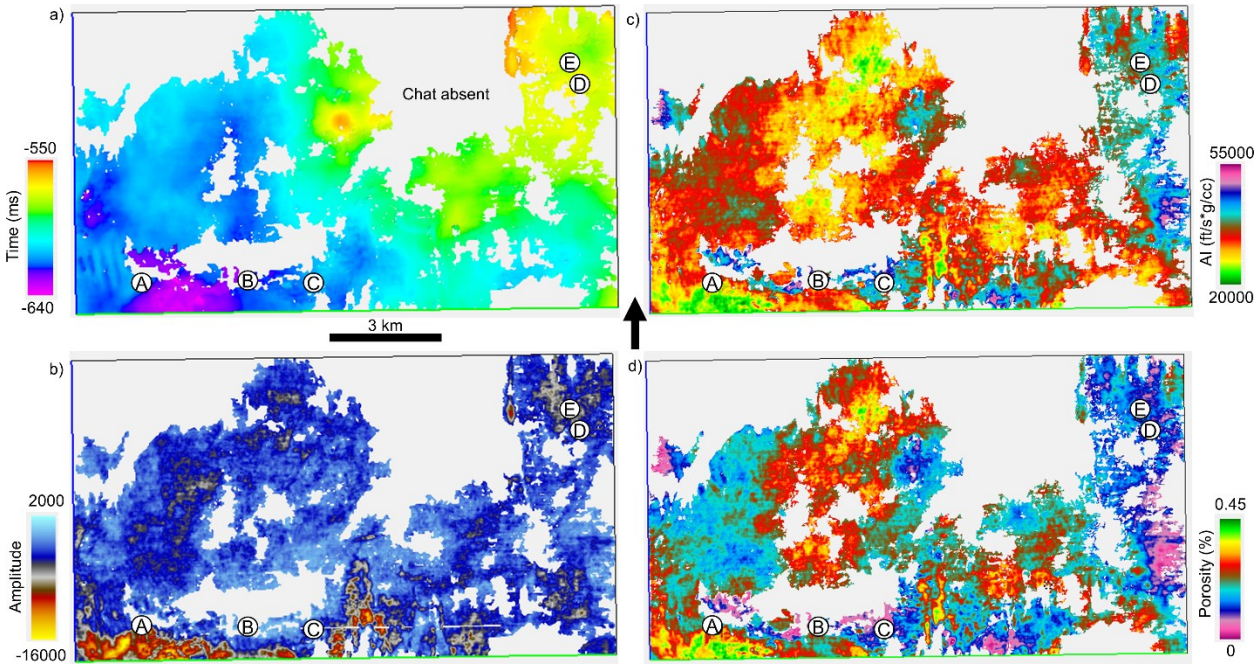

Figure 4.13. Chat attribute maps. White circles are well locations and mapped quantity is indicated on each color bar. (a) Horizon time structure shown only where high-confidence tracking is possible. Hot colors are shallow and cool colors are deeper. (b) Horizon amplitude with hot colors indicating stronger negative values. (c) Acoustic impedance (AI). (d) Total porosity. Chat properties show rapid and extreme lateral variability.

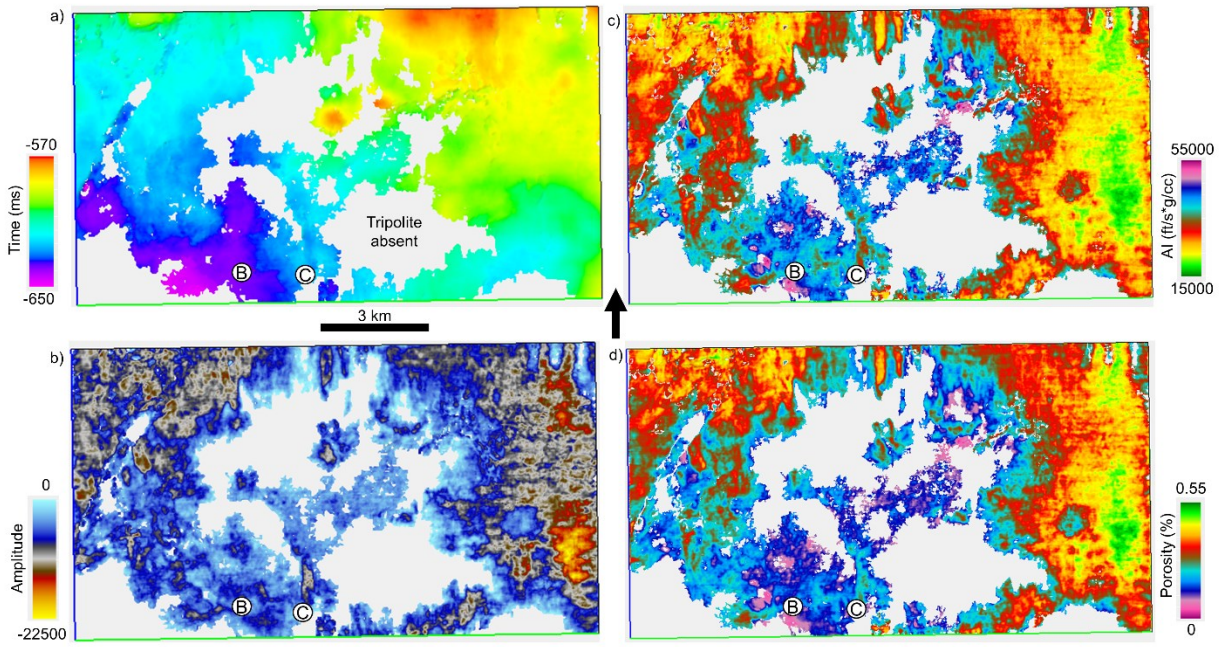

Figure 4.14. Tripolite attribute maps. White circles are well locations and quantity being mapped is indicated on each color bar. (a) Horizon time structure shown only where high-confidence tracking is possible. Hot colors are shallow and cool colors are deeper. Regional dip from NE to SW is evident, perhaps indicating that diagenetic processes that developed the tripolite occurred along bedding planes. (b) Horizon amplitude with hot colors indicating stronger negative values.. The strongest negative amplitudes are generally associated with high structural relief. (c) Acoustic impedance (AI). (d) Total porosity

Tables

Table 4.1. Available wells data. Gamma ray (GR), density (DEN), resistivity (RES), photoelectric factor (PE), P-wave sonic (DTCO), S-wave sonic (DTSM), X-ray fluorescence (XRF), Kelly busing (KB), and total depth (TD). Wells A through E are in the 3D survey area. AI units (g/cc* ft/s)

Well	*A*	*B*	*C*	*D*	*E*	*F*	*G*	*H*	*I*	*J*
GR	Y	Y	Y	Y	Y	Y	N	N	N	N
DEN	Y	Y	Y	Y	Y	Y	N	N	N	N
RES	Y	Y	Y	Y	Y	Y	N	N	N	N
PE	N	Y	Y	N	Y	Y	N	N	N	N
DTCO	Y	Y	N	N	N	Y	N	N	N	N
DTSM	N	Y	N	N	N	N	N	N	N	N
CORE	N	N	N	N	Y	N	Y	Y	Y	Y
XRF	N	N	N	N	N	N	N	N	Y	Y
Year Drilled	2002	2012	1996	2007	2006	2007	1955	1955	1956	1980
Formation	Miss Lime	Arbuckle	Miss Lime	Miss Lime	Miss Lime	Granite	Miss Lime	Miss Lime	Miss Lime	Miss Lime
KB	925	908	905	896	889	954	1062	1002	1317	1156
TD (ft)	3905	3809	3230	3024	3035	4550	3289	3166	2812	3310
Chat AI	29077	29587	--	--	--	22053	--	--	--	--
Tripolite AI	--	32603	--	--	---	--	--	--	--	--

Table 4.2. Well B rock physics properties and seismic resolution. *100 ft of shale above Chat. Mean values for mineralogy, density, P and S velocities.

Unit	*Shale**	*Chat*	*Upper Lime*	*Tripolite*	*Lower Lime*
No. of samples	200	34	246	62	326
Mineralogy (silica, carb, clay)	42, 1, 6	82, 0, 17	35, 56, 9	91, 5, 4	41, 50, 8
Porosity (%)	N/A	29	6	21	5
Origin	--	unconformity	--	hydrothermal	--
Density (g/cc)	2.618	2.287	2.645	2.325	2.641
P Velocity (m/s) / (ft/s)	3921 / 12864	3930 / 12894	5407 / 17740	4260 / 13976	5423 / 17792
S Velocity (m/s) / (ft/s)	2058 / 6752	2359 / 7740	3087 / 10127	2515 / 8251	3219 / 10561
Top/Base Amp	--	-/+	+/-	-/+	+/-
Thickness (m) / (ft)	30.5 / 100	5.1 / 17	37.5 / 123	9.4 / 31	49.6 / 162.72
57.5 Hz Vertical Resolution (m) / (ft)	17.05 / 56	17.1 / 56.10	23.5 / 77	18.52 / 60.76	23.57 / 77.32
P Wavelength (m) / (ft)	68 / 224	68 / 224	94 / 308	74 / 243	94 / 184
P Lateral Resolution (m) / (ft)	112	112	154	120	154
TWT Seismic Thickness (ms)	--	2.6	13.87	4.41	18.29

CHAPTER 5

Conclusion / Implications of This Study

We have reviewed worldwide expression of karst reservoirs around the world, interpreted and characterized Paleozoic paleokarst sinkhole and pipe features in Hughes and Coal County in the Arkoma Basin, Oklahoma, and distinguished paleokarst Mississippian Chat and tripolite zones in the Cherokee Platform, Osage County, Oklahoma.

Worldwide observation of paleokarst show occurrence from Precambrian to the Miocene with depths ranging from less than 200 m to up to 8000 m in the subsurface. Paleokarst features delineated on seismic data show sinkholes have diameters less than 100 m to greater than 2 km with depths greater than 100 m, pipe features up to 800 m in extent, paleocave complexes are up to 2.4 km long and tower karst up to 150 m in height. Karst features occur as sinkholes, tower karst, hills and fluviokarst features such as channels, canyons, and valleys. Anomalous amplitudes and bright spots characterize cave collapse indicative of low velocity zones. Pipe features show tapering upwards and cylindrical to conical geometry. Seismic attributes of bright amplitude, high variance, high curvature, and low acoustic impedance image and delineate sinkhole features. Isochron and isopach maps describe sinkhole evolution and distribution.

We have examined four seismic horizons which are the Ordovician Viola Limestone, Mississippian Caney Shale, Pennsylvanian Jefferson Sandstone and Wapanucka Limestone for paleokarst evidence in the Arkoma Basin. Vertical pipe features extend beyond the Ordovician terminating in the Mississippian formation and do not extend into the Pennsylvanian, with a vertical extent up to 490 m and diameters up to 520 m. The pipes exhibit high variance and are spatially coincident with Viola sinkholes and Caney sags. Viola sinkholes show significant relief, high variance, and low amplitudes. Viola sinkholes and pipe features are indicative of a mature

epigene paleokarst system. Wapanucka sinkholes show high amplitudes within and show no significant relief observed on seismic amplitude and are coincident with the Viola sinkholes. The Wapanucka sinkholes signify immature hypogene paleokarst formed by restricted subareal exposure, and later hydrothermal modification of the Wapanucka Limestone.

We have distinguished paleokarst Chat and tripolite zones associated with the Mississippian Lime in the Cherokee Platform. Wedge models indicate that Chat and tripolite show an increase in negative amplitudes with increase in thickness, however significantly Chat can be almost transparent to seismic reflection under acceptable circumstances. Note that high negative amplitudes observed for Chat are not solely due to thicknesses greater than the seismic resolution but also depend on acoustic impedance contrast of the surrounding material, noise, and phase of the wavelet. Seismic analysis show that well-developed Chat and tripolite regions are often characterized by strong negative amplitudes, but may also be effectively transparent to seismic reflection, proposing a new exploration method of mapping ‘Chat dim-outs’. Attribute analysis indicate that well-developed Chat regions are found in low structural relief. Well-developed tripolite regions show lower acoustic impedance, high porosity, and high negative amplitudes than Chat, and are in high structural relief, and covers a larger area than Chat.